



# Predicting plate velocities with mantle circulation models

Thorsten W. Becker and Richard J. O'Connell

Department of Earth and Planetary Sciences, Harvard University, 20 Oxford Street, Cambridge Massachusetts 02138, USA (becker@eps.harvard.edu; oconnell@geophysics.harvard.edu)

[1] **Abstract:** We predict plate motions from a comprehensive inversion of theoretical estimates of tectonic forces in order to evaluate the relative importance of these and the uncertainties of such models. Plate-driving forces from the mantle are calculated using global flow models that are driven by tomography and subduction-derived density fields. Observed and predicted plate velocities agree well for a variety of models, leading to varied conclusions about the relative importance of forces. The dominance of the subduction related density pattern in the mantle is confirmed; it appears that *P* wave models do not satisfactorily image all of the slab-associated anomalies in the upper mantle. Furthermore, lower mantle structure always improves the plate motion fit with respect to models that are based on upper mantle anomalies and lithospheric thickening only. We show that the average torques from the lower mantle scale with the radial flow through the 660-km phase transition; the amplitude of the lower mantle torques will be significant for a range of models if there is mass flux through 660 km. We also evaluate parameterized edge forces and find that the additional inclusion of such torques does not significantly improve the model fit. The main reason for the nonuniqueness of the inversions is plate boundary geometry since all plate motions are dominated by the trench-ridge system, and plates move from ridges to trenches.

**Keywords:** Plate motions; driving forces; edge forces; subduction history; mantle convection; mantle structure.

**Index terms:** Dynamics of lithosphere and mantle-general; plate motions-general; dynamics, convection currents and mantle plumes; tomography.

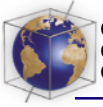
**Received** April 26, 2001; **Revised** August 22, 2001; **Accepted** August 24, 2001; **Published** December 28, 2001.

Becker, T. W., and R. J. O'Connell, 2001. Predicting plate velocities with mantle circulation models, *Geochem. Geophys. Geosyst.*, 2, 10.1029/2001GC000171, 2001.

## 1. Introduction

[2] It is now commonly accepted that plate motions are the surface expression of mantle convection. How the dynamical system plate tectonics should be broken down into parts to identify, isolate, and analyze the driving forces has, however, been debated for the last 30 years. As a recent AGU session shows

[Bokelmann and Humphreys, 2000], there is continuing controversy with regard to the most basic issues and a division between seemingly distinct approaches persists. These modeling approaches can be roughly classified into two types: the force balance type (where the goal is to achieve a force equilibrium for each plate given the observed plate motions) or the velocity model type (where



driving forces and resulting tractions are calculated first and model quality is subsequently judged from the plate motion predictions). Both approaches can be understood as alternative solutions to a boundary value problem, but it is not known a priori if they give the same answer. However, one expects that they would approach one another as the errors in each became small (which would be the case for a completely linear model). In our study, we attempt to combine both approaches to understand why different combinations of plate driving forces are successful in predicting plate velocities.

[3] Given its long-standing history, it is not feasible to give an exhaustive review of the problem here; the following account of previous work is necessarily incomplete. With regard to the quantifying of individual plate-driving forces, the role of sinking slabs and sublithospheric convection was mentioned by *Isacks et al.* [1968]. *McKenzie* [1967, 1968] estimated the cooling of the oceanic lithosphere and the temperature structure of subducted slabs which provided the basis for subsequent calculation of driving forces. The role of horizontal structural variations and a low viscosity asthenosphere in driving plate motions was discussed by *Hales* [1969] and *Lliboutry* [1969]; both considered plates sliding on topographic swells, and neither explicitly considered the cooling lithosphere. However, cooling lithosphere, sinking slabs and sublithospheric convection were all implicitly included in the boundary layer model of *Turcotte and Oxburgh* [1967]. *Elsasser* [1969] pointed out the importance of the lithosphere as a stress guide that integrates tractions acting over its surface. *Richter* [1973] then analyzed models of upper mantle convection beneath a plate and emphasized the importance of subducted slabs for driving plate motions. The effect of the cooling lithosphere in providing a plate-driving force was clarified by *Lister* [1975].

[4] The first to consider plate motions on a global scale were *Solomon and Sleep* [1974] who discussed the no net torque concept for the force equilibrium on the plates, *Harper* [1975] who calculated the forces from lithospheric cooling and sinking slabs for specific plates and used them to calculate plate velocities, and *Forsyth and Uyeda* [1975] who considered parameterized forces acting on all the plates and sought a force balance to constrain their estimates (Figure 1). The parameterized force model was broadened by *Chapple and Tullis* [1977] who included an explicit calculation of the sinking force from subducted slabs, thus constraining the magnitudes of the parameterized forces. *Solomon et al.* [1975] and *Richardson et al.* [1979] introduced the use of the intraplate stress field to test force models and found that ridge push was as important as other forces such as slab pull.

[5] The three-dimensional flow in the mantle associated with plate motions was calculated by *Hager and O'Connell* [1979] and included in a force balance model by *Hager and O'Connell* [1981]. This model explicitly included forces from lithospheric cooling, density in subducted slabs, and flow in the mantle excited by sinking slabs and by the motions of plates, including the return flow from subduction zones to ridges. Forces on plate boundaries were parameterized [after *Forsyth and Uyeda*, 1975] and chosen to minimize the net force on each plate. The complementary approach, a velocity model, was presented by *Ricard and Vigny* [1989] who calculated forces from density heterogeneities associated with subducted slabs, and seismic tomography in the upper and lower mantle. They did not consider any forces on plate boundaries. The use of seismic tomography to estimate mantle density heterogeneity was introduced by *Hager et al.* [1985] in a study of the origin of the geoid and *Forte and Peltier* [1987] used plate velocities to constrain the mantle viscosity. Among the more

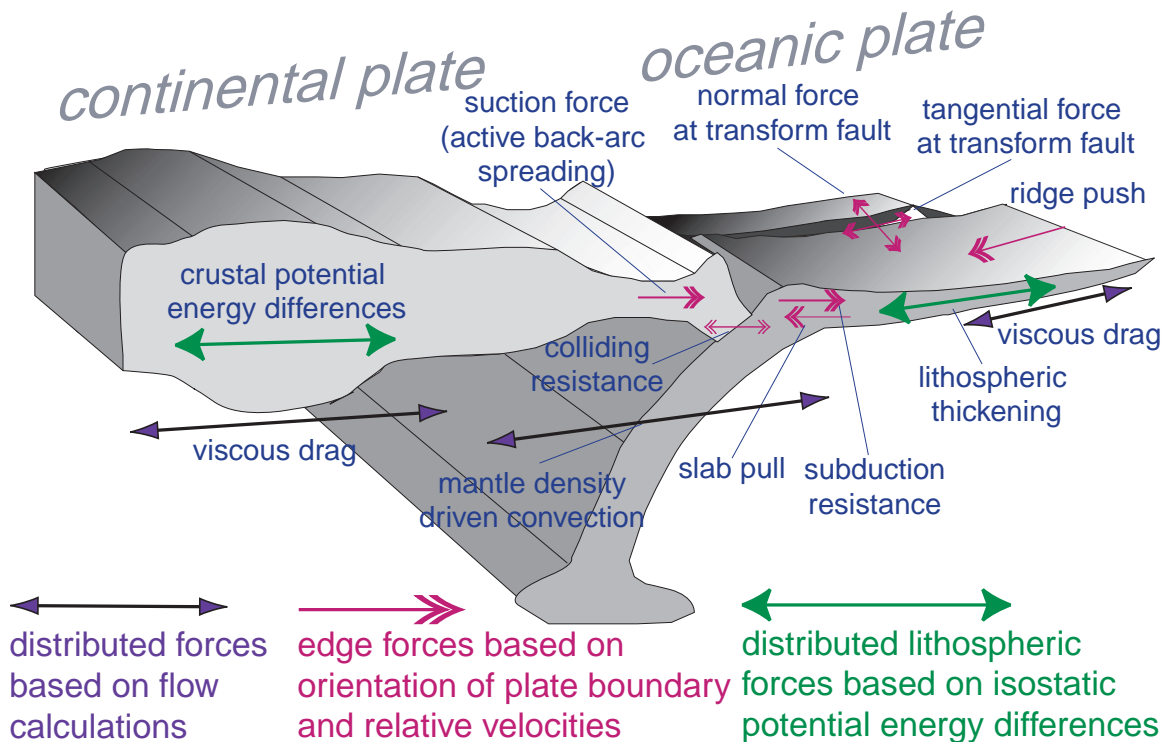
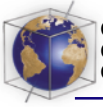


**Figure 1.** Forces acting on plates, modified after *Forsyth and Uyeda* [1975].

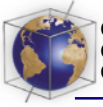
recent studies are those of *Deparis et al.* [1995] and *Lithgow-Bertelloni and Richards* [1995, 1998], who estimated density variations in the lower mantle from a model based on the locations of past subduction and also considered the balance of forces acting on different plate configurations during the Cenozoic.

### 1.1. Aim of This Paper

[6] Plausible models for forces causing plate motions can be found. The earlier models [*Harper, 1975; Forsyth and Uyeda, 1975; Hager and O'Connell, 1981*] all indicated that subducted slabs were important but that other forces were comparable to the net force transmitted to the plate by the sinking slab. Later, *Lithgow-Bertelloni and Richards* [1998] found that for their best-fit model, lower mantle

density variations resulting from past subduction were most important. Evaluating these studies is difficult because each uses different combinations of forces. We will therefore systematically investigate the role of all the forces that have been proposed in order to explore the range of uncertainty in the models. A velocity model will be used to test if candidates produce realistic plate motions in a simplified spherical flow-model, using rigid plates with the current geometry and radial viscosity profiles from the literature. As driving torques, we consider several models of lithospheric and mantle density structures, either based on seismic tomography or past subduction, and edge forces.

[7] We find that models that account for mantle-based forces always achieve a better



fit than models driven by lithospheric thickening and slab pull only. This result is insensitive to the details of the viscosity structure with depth, and the lower mantle will have a significant effect as long as there is mass flux through the 660-km discontinuity. We confirm earlier studies that indicate the importance of deep mantle density anomalies resulting from subduction [Deparis *et al.*, 1995; Lithgow-Bertelloni and Richards, 1998] and find that plate motions based on slab models are not significantly different from models that use seismic tomography to infer lower mantle densities. However, we demonstrate that estimates of the relative importance of different forces change with input model choice. This ambiguity is not resolved if parameterized plate boundary forces are introduced. While the model fit can be improved when such forces are considered, the gain is small. We show that this is due to plate geometry, leading to strong (anti-)correlations between several driving and resisting forces. These trade-offs were noted before for the slab pull/subduction resistance pair [Forsyth and Uyeda, 1975]; we demonstrate that all forces except the back arc suction and the transform fault normal forces can be classified as either driving or resisting in a roughly uniform fashion.

## 2. Method

[8] Our basic method of solving for plate velocities has been used for a thermal convection model with plates [Gable *et al.*, 1991], is similar to that of Ricard and Vigny [1989], and described in some detail by Lithgow-Bertelloni and Richards [1998]. The following discussion will therefore be brief.

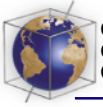
### 2.1. Observed Plate Motions

[9] We treat plate tectonics as a system of rigid plates and use the boundaries and Euler poles

from NUVEL-1 [DeMets *et al.*, 1990] to define the individual plates (Figures A1, A2, and A3). Since the no net torque condition for the force equilibrium of the plate motions can be fulfilled with any arbitrary rigid body rotation, we set this rotation to zero and use the no net rotation (NNR) reference frame for velocities. It has been shown that a net rotation of the lithosphere with respect to the mantle can only be excited in the presence of lateral viscosity variations [O'Connell *et al.*, 1991]. As such variations are missing from our model, the NNR frame is the natural choice. Out of the original 14 plates of NUVEL-1, we ignore the Juan de Fuca plate since it is too small to yield a reliable velocity prediction. We treat the Australian(AUS)-Indian(IND) system as two plates, divided along an inferred plate boundary in the Indian Ocean. We find that the inversion is not sensitive to this distinction since AUS and IND move in nearly the same direction.

### 2.2. Global Flow Models

[10] We model mantle convection as the instantaneous flow that solves the Navier-Stokes and continuity equations for the incompressible, infinite Prandtl number case given a known density anomaly distribution. If the viscosity varies only radially, the equations can be solved by the propagator matrix method [Hager and O'Connell, 1979, 1981]; we use an implementation by Steinberger [2000]. Such an approach involves expanding fields into spherical harmonics, leading to well-known problems: since velocities are discontinuous at the plate boundaries, theoretical stresses there are singular, and the exact value of the resolved stress depends on the maximum degree  $\ell_{\max}$  of the expansion [Hager and O'Connell, 1981]. Following Hager and O'Connell, we circumvent this problem by evaluating all stresses below the viscous lithosphere at depth  $z = 100$  km. It has been shown that the integrated torques



using this approach are insensitive to  $\ell_{\max}$  [Hager and O'Connell, 1981; Lithgow-Bertelloni and Richards, 1998]. Our theoretical resolution is then limited mainly by the seismic tomography models, since we know plate boundaries and upper mantle slab locations to higher precision, and we will use  $\ell_{\max} = 31$  for computational efficiency.

### 2.3. Torque Balance and Plate Velocity Solution

[11] We interpret fast and slow regions of seismic anomalies as being purely thermal in origin [e.g., Hager *et al.*, 1985] except for the continental tectosphere. Thermal density anomalies then drive flow in the mantle and exert torques on the overlying lithosphere. The solution for plate velocities depends on the linearity of the momentum equation [compare Gable *et al.*, 1991]. First, flow driven by density anomalies is calculated with a fixed surface (i.e., no plate motion), and the tractions on the base of each plate are evaluated. Second the motions of plates will also cause flow that exerts viscous drag on their base; the corresponding tractions are evaluated for the motion of each individual plate. Third the plate velocities that are driven by internal flow are found from the superposition of these solutions that results in zero net torque on each plate. We write this condition as

$$\mathbf{T}_{vd} = \mathbf{P} \cdot \boldsymbol{\omega} = \sum_i^M \mathbf{T}_i, \quad (1)$$

where we have expressed the torque due to viscous drag  $\mathbf{T}_{vd}$  as the product of the interaction matrix  $\mathbf{P}$  ( $3N \times 3N$  components) with the plate rotation vector  $\boldsymbol{\omega}$  ( $3N$  components), where  $N$  is the number of plates (13 in our case).  $\mathbf{P}$  is calculated by prescribing unity velocities for each plate and calculating the resulting drag torques on all other plates [Gable, 1989].  $\mathbf{T}_i$  are the driving torques from  $M$  various sources, such as lower and upper

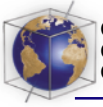
mantle flow, lithospheric contributions, and edge forces. Equation (1) is then solved for the plate rotations  $\boldsymbol{\omega}$ , assuming that the  $\mathbf{T}_i$  are known. We use singular value decomposition [e.g., Press *et al.*, 1993] and neglect small singular values to avoid the singularity of  $\mathbf{P}$  (a rigid body rotation can be added to  $\boldsymbol{\omega}$  without affecting  $\mathbf{P} \cdot \boldsymbol{\omega}$ ). We therefore enforce the no net rotation reference frame for plate motions  $\boldsymbol{\omega}$ .

[12] To determine torques that are based on tractions,  $\boldsymbol{\sigma}$ , beneath plates, we evaluate surface integrals of the type

$$\mathbf{T}_i = \int_{\text{plate}} dA \mathbf{r} \times \boldsymbol{\sigma} \quad (2)$$

numerically at  $0.5^\circ$  spacing. Here  $\mathbf{r}$  is the location vector, and  $dA$  indicates the plate area. Karpichev and Fleitout [1996] have argued that the detailed location of density anomalies is important when plate velocities are to be predicted because strong lateral variations of viscosity can be expected at plate margins. While we cannot treat such lateral variations with our model, we have explored a simplified scenario: the outcome if we do not consider tractions that are closer than  $\sim 200$  km to a plate boundary. The torques that we calculate with this constraint are similar to those that use all tractions, implying that at least our large-scale integrated torques are insensitive to the details of the density structure near plate boundaries.

[13] Recently, Steinberger *et al.* [2001] developed a thin shell formulation for the elastic and viscous deformation of the lithosphere owing to basal tractions, an extension of work by Bai *et al.* [1992]. We found that the torques calculated when such deformation is included are larger in amplitude than our rigid plate torques by  $\sim 15\%$  but very similar in direction. Since the role of the deforming lithosphere can ultimately only be resolved if we allow for faulted margins and a more realistic rheology, we will neglect the deformation of the lithosphere and



rheological complexity in our current calculations.

## 2.4. Inversion for Scaling Parameters

[14] The amplitude of torques that result from tomography-based flow calculations is proportional to the factor

$$R_Q^{p,s} = \frac{d \ln Q}{d \ln v_{p,s}} \quad (3)$$

that relates density anomalies,  $d \ln Q$ , to  $P$  and  $s$  wave anomalies,  $d \ln v_{p,s}$ , and all plate motion derived viscous drag torques scale with the absolute value of the viscosity,  $\eta_0$ . We allow these scaling factors to vary in order to minimize the difference between the calculated,  $\omega^{\text{mod}}$ , and observed,  $\omega^{\text{obs}}$ , plate rotation vectors. We use the downhill simplex method of *Nelder and Mead* [1965] for optimization [e.g., *Press et al.*, 1993], and minimize the misfit by varying the scalar weight of  $\mathbf{P}$  (factor  $w_1$ ) and the driving torques  $\mathbf{T}_i$  (factors  $w_2 \dots w_{M+1}$ ). The quality of fit is measured by the linear correlation coefficient,  $r$ , of the Cartesian components of the rotation vectors and the variance reduction, VR:

$$\text{VR} = 1 - \xi^2 / |\omega^{\text{obs}}|^2 \quad \text{with} \quad \xi^2 = \sum_i^{3N} (\omega_i^{\text{obs}} - \omega_i^{\text{mod}})^2. \quad (4)$$

We will present results in terms of the unweighted quantities  $r$  and VR and the plate-area weighted values  $r_w$  and  $\text{VR}_w$ . The  $r_w$  is equivalent to the point by point correlation for surface velocities and, as noted by *Lithgow-Bertelloni and Richards* [1995], dominated by the large, fast plates like PAC.

[15] The objective of the simplex method is to minimize  $\text{VR}_w$  (and therefore to maximize  $r_w$ ). The final weights are then normalized such that  $\sum_i w_i^2 = 1$ , and, using a penalty formulation, we usually enforce that all weights  $w_i \geq 0$ . (This prohibits driving forces from changing sign and becoming resisting forces.) We tested our sim-

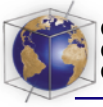
plex procedure by comparison with a grid search for  $M \leq 3$  and were able to find the global minimum to within  $|\Delta r_w| \lesssim 0.003$ . However, as we will show in section 3.5, many of the driving torques are highly correlated. This results in trade-offs that are responsible for the existence of numerous local minima in  $w_i$  space that correspond to solutions of the inverse problem with only slightly poorer fits to plate motions than the global minimum.

## 3. Input Models

[16] We now analyze the input models that are used to derive estimates of the various types of plate-driving forces. First we discuss the mantle density fields as inferred from tomography and geodynamic models, and second we study their degree of similarity. Third we explore different models of lithospheric thickening and ridge push. Last we describe how we derive edge forces based on NUVEL-1 plate boundaries.

### 3.1. Seismic Tomography

[17] We assume that the anomalies that are imaged by seismic tomography are thermal in origin throughout all but the shallowest mantle [e.g., *Hager et al.*, 1985; *Mitrovica and Forte*, 1997]. This is a simplification since velocity heterogeneities may well be due to compositional variations [e.g., *Ishii and Tromp*, 2001], although there is no consensus on this issue at present [e.g., *Masters et al.*, 2000; *Tackley*, 2000]. We also neglect depth-dependence of  $R_Q$  [e.g., *Karato*, 1993] for simplicity but use typical starting values of  $R_Q^p = 0.4$  and  $R_Q^s = 0.2$ .  $R_Q$  can then be adjusted via the optimized weights  $w_i$  (see section 2.4). We furthermore remove all structure shallower than 220 km depth from the tomographic models to account for the effect of the tectosphere where compositional differences are likely to cancel out the fast anomalies beneath cratons [e.g., *Jordan*, 1978;



*Forte et al.*, 1995]. For  $P$  wave tomography, craton related structures are probably imaged at depths larger than 220 km [e.g., *Becker and Boschi*, 2001]; our cutoff value might therefore be too low for these models. In any case, we will see that best-fit inversions tend to include only lower mantle for  $P$  wave models. Removing shallow structure also avoids counting lithospheric thickening twice since it is explicitly included as a separate torque.

[18] The following models were selected as representative of the current state of seismic tomography. For  $P$  wave models, we consider BDP00 (bdp00), which is an improved version of BDP98 [*Boschi and Dziewonski*, 1999; *Antolik et al.*, 2001], and a model by *Kárason and van der Hilst* [2001] (kh00p). For  $s$  wave models, we use S20RTS (s20rts) [*Ritsema and van Heijst*, 2000], SB4L18 (sb4l18) [*Masters et al.*, 1999], and S. Grand's model (ngrand) [*Grand*, 1994; *Grand et al.*, 1997], obtained in June 2001 (<ftp://amazon.geo.utexas.edu/outgoing/steveg>). All models were expanded into spherical harmonics up to  $\ell_{\max} = 31$ .

### 3.2. Subduction Models

[19] Geodynamic subduction models are an alternative to tomography models, and if the assumptions that go into these models are correct, they should directly predict the location of density anomalies caused by sinking slabs, though not those due to independent upwellings. We consider two whole, and one upper, mantle subduction model. Whole mantle model one (lrr98d) is by *Lithgow-Bertelloni and Richards* [1998] and based on a method by *Ricard et al.* [1993]. *Lithgow-Bertelloni and Richards* used existing reconstructions of Cenozoic plate motions [*Gordon and Jurdy*, 1986] and complemented those with their own reconstructions for the Mesozoic to determine the location of past trenches. From these locations, portions of lithospheric slabs were allowed to

descend into the mantle. Negative density anomalies were not advected by mantle flow laterally but only sank by a rate parameterized by the surrounding mantle viscosity. Whole mantle model two (stb00d) is by *Steinberger* [2000] and also based on *Lithgow-Bertelloni and Richards'* [1998] reconstruction. The difference from lrr98d is that sinking slabs themselves partly drive convection and are advected with the resulting flow. Both models are similar at long wavelengths, which can be explained by the finding that lateral flow is weak at middle to lower mantle depths. We note, however, that lrr98d and stb00d are quite different for  $\ell \gtrsim 5$ , possibly owing to different slab sinking rates and the interpolation method that was used by *Steinberger* [2000] to smooth the transition between plate tectonic stages [*Becker and Boschi*, 2001].

[20] For the upper mantle part of the slab pull forces, we consider a third model that attributes a density anomaly of  $\Delta\rho = 75 \text{ kg/m}^3$  to each location where we observe seismicity in subducted lithosphere (rum). Wadati-Benioff zones were converted to a spherical harmonics model by integrating along the RUM slab contours [*Gudmundsson and Sambridge*, 1998], which are in turn based on *Engdahl et al.'s* [1998] catalog. We will furthermore contrast this seismically active upper mantle slab model with the upper mantle part of lrr98d to study the possible effect of older, aseismic slab material.

[21] The slab pull that follows from flow calculations based on models like rum is a force that acts on both the subducting and the overriding plate because of the viscous drag of sinking slabs that is transferred to the base of the lithosphere. This is different from the common notion of a stress guide coupling the negative buoyancy of the subducting lithosphere to the oceanic plate only (compare *King et al.* [1992] for a comparison of different ways

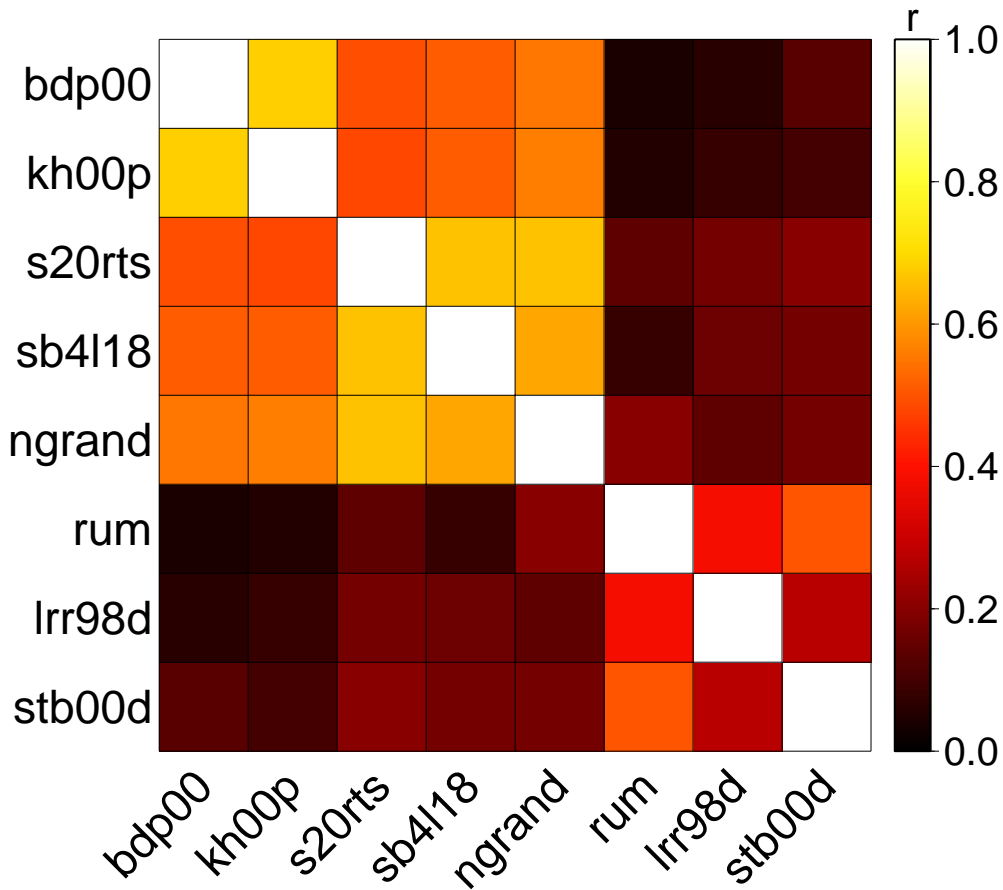
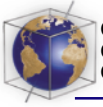


**Figure 2.** Total correlation,  $\langle r_{20} \rangle$ , matrix for mantle structure models. For  $\ell_{\max} = 20$ ,  $r$  has  $(1 + \ell_{\max})^2 - 3 = 438$  degrees of freedom. Assuming Student's  $t$  distribution applies, it follows that  $|r| \geq 0.12$  is statistically significant at the 99% level [e.g., *Press et al.*, 1993].

of treating slab forces). We find that our model predictions are actually better if we apply a two-sided drag force instead of a one-sided slab pull (see section 4.2.4). This might be because slabs are comparable in strength to the surrounding mantle [e.g., *Moresi and Gurnis*, 1996], and it is the mantle flow that couples slab forces to the overlying plates.

### 3.3. Mantle Model Similarity

[22] To explore the degree of similarity between our input models, Figure 2 shows

the total average correlation,  $\langle r_{20} \rangle$ , between all models discussed in section 3.2. The  $\langle r_{20} \rangle$  was calculated based on spherical harmonics up to  $\ell_{\max} = 20$  with volume weighted averaging with depth. Correlation analysis involves subtleties [e.g., *Ray and Anderson*, 1994], notably when sharp features such as slabs are compared in the spectral domain. However, we see that, on average, geodynamic models do not correlate well with tomography. (From Figure 2, we find that the mean  $\langle r_{20} \rangle$  between tomography and subduction models is 0.15 and 0.12 for stb00d and lrr98d,



respectively.) This is especially true for  $\ell \gtrsim 5$ , and even when only fast anomalies and wavelengths up to  $\ell_{\max} = 8$  are compared with the slab models, global correlations are not substantially improved. Different  $S$  and  $P$  wave models, however, correlate fairly well with models of the same type, as should be expected given that especially  $P$  models are based on very similar data sets. There is moderately good correlation between  $S$  and  $P$  wave models that image different rock properties and have different sensitivity kernels. Further discussion of the input model properties such as the relative heterogeneity signal strength is given by *Becker and Boschi* [2001].

### 3.4. Lithospheric Contributions

[23] Lateral variations in the density structure of the lithosphere can lead to deviatoric stresses and drive plate motions [e.g., *Artyushkov*, 1973; *Lister*, 1975; *Hager*, 1978; *Hager and O'Connell*, 1981; *Fleitout and Froidevaux*, 1982]. These stresses can be derived from the gradient of the vertically averaged normal stress,  $\bar{\sigma}_{rr}$ , or equivalently from the potential energy per unit area,  $U$ . Variations in  $U$  for the oceanic plates are mainly due to sea-floor spreading and the age progression of the lithosphere which results in a distributed lithospheric thickening force [e.g., *Hager*, 1978]. In continents, lateral gradients in  $U$ ,  $\nabla U$ , can be expected to be most pronounced around regions of high topography where forces arise from the tendency of orogens to collapse and spread. The effectiveness of intracontinental  $\nabla U$  for plate-driving forces will depend on the rheology of the lower lithosphere; it will be most pronounced for regions where lateral variations are important down to the asthenosphere in young tectonic settings. Moreover, intraplate continental stresses that are not active across plate boundaries will tend to have little net effect on driving a plate. Hence, we will make a dis-

inction between lithospheric models that are only based on oceanic contributions and global models that incorporate continental contributions as well.

[24] Our approach is similar to that of *Coblentz et al.* [1994]: We use an isostatic, long-wavelength and thin sheet approximation for the lithosphere. Solving for vertically averaged stresses, we can then relate the gradient in  $U$  to equivalent basal tractions,  $\sigma_{\{r\theta, r\phi\}}$ , [*Fleitout and Froidevaux*, 1983]:

$$U(\theta, \phi) = \int_0^{L+\varepsilon} dr g \varrho(r)r \quad (5)$$

$$\sigma_{\{r\theta, r\phi\}} \approx -L_0 \nabla_{\{\theta, \phi\}} \bar{\sigma}_{rr} \quad (6)$$

$$= -\frac{L_0}{L} \nabla_{\{\theta, \phi\}} U, \quad (7)$$

where  $L$  is the isostatic compensation depth ( $L = 130$  km),  $L_0$  is the lithospheric shell thickness ( $L_0 = 100$  km),  $\varepsilon$  is elevation,  $g$  is gravitational acceleration ( $g = 9.81$  m/s<sup>2</sup>),  $\varrho$  density, and  $\nabla_{\{\theta, \phi\}}$  are the  $\theta$  and  $\phi$  components of the horizontal gradient operator, respectively.

[25] We have used the 3SMAC model [*Nataf and Ricard*, 1996] to obtain ice thickness and extrapolated  $2^\circ \times 2^\circ$  sea-floor ages from which we calculate an oceanic lithosphere model, using a modified half-space cooling progression for the water depth  $d_w$  [*Parsons and Sclater*, 1977; *Carlson and Johnson*, 1994]:

$$d_w = 2600 \text{ m} + 345 \text{ m} \sqrt{t[\text{Ma}]} \quad \text{for } t \leq 81 \text{ Ma} \quad \text{and} \quad (8)$$

$$d_w = 6586 \text{ m} - 3200 \text{ m} \exp\left(\frac{-t[\text{Ma}]}{62.8}\right) \quad \text{for } t > 81 \text{ Ma}. \quad (9)$$

The thickness of the oceanic lithosphere,  $d_{li}^{oc}$ , is found from isostasy for constant  $\varrho_{li}^{oc}$  and crustal thickness  $d_{cr}^{oc} = 8$  km. This leads to a simplified model for the lithospheric thickening force with  $d_{li}^{oc} \leq 100$  km. For continental

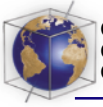


**Table 1.** Average Density of the Lithospheric Model for Layers<sup>a</sup>

Type	Value, kg/m <sup>3</sup>
Q <sub>ic</sub>	920
Q <sub>wa</sub>	1020
Q <sub>cr</sub> <sup>co</sup>	2861
Q <sub>ma</sub> <sup>co</sup>	3380
Q <sub>ma</sub> <sup>oc</sup>	3350
Q <sub>li</sub> <sup>oc</sup>	3412
Q <sub>cr</sub> <sup>oc</sup>	2868

<sup>a</sup> Here ic, ice; wa, water; <sup>co</sup><sub>cr</sub>, continental crust; <sup>co</sup><sub>ma</sub>, subcontinental mantle; <sup>oc</sup><sub>ma</sub>, suboceanic mantle; <sup>oc</sup><sub>li</sub>, oceanic lithosphere; and <sup>oc</sup><sub>cr</sub>, oceanic crust.

areas, we correct a 2° smoothed ETOPO5 topography [National Oceanic and Atmospheric Administration (NOAA), 1988] for the iceload and again determine an isostatic crustal thickness using average densities as given in Table 1. The resulting potential energy differences from a global mean of  $\bar{U} = 2.616 \cdot 10^{14} \text{ J/m}^2$  are shown in Figure 3. As expected, the main variations are due to seafloor age and large orogens.

[26] Our model is a simplification of the actual lithospheric density variations, and we have strived to emphasize well constrained features like the sea floor age. In addition, we have experimented with more detailed models of the continental crust such as CRUST 5.1 [Mooney *et al.*, 1998]. We note, however, that CRUST 5.1 is not an isostatic model, but the topography has to be dynamically [Pari and Peltier, 2000] or compositionally supported in the mantle. Since we attempt to include dynamic effects in our flow models and want to exclude cratonic tectosphere, we will limit ourselves to isostatic models at this point.

[27] After taking the gradient of  $U$ , we derive tractions from (2); integration yields the driving torques that are shown together with Coblenz *et al.*'s [1994] results in Figure 4. We have chosen to evaluate the torques as equivalent forces at the plate centroids instead of showing a force field to allow for easier comparison between different driving torques.

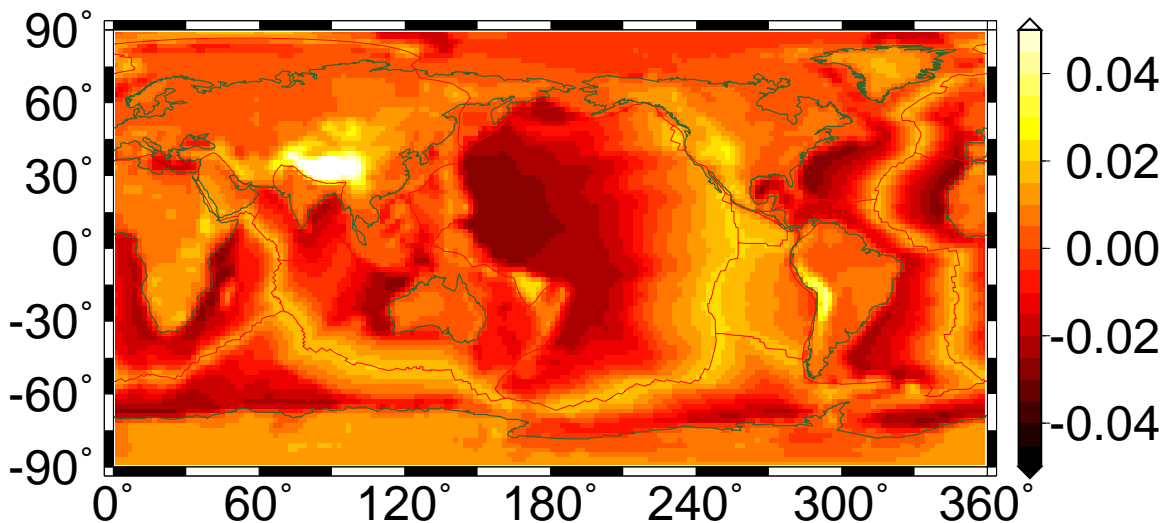


**Figure 3.** Differential potential energy  $\Delta U = U - \bar{U}$  ( $\bar{U} = 2.616 \times 10^{14} \text{ Jm}^{-2}$ ) of our  $2^\circ \times 2^\circ$  model in units of  $10^{14} \text{ Jm}^{-2}$ . Min/mean/max values of  $\Delta U$  for oceanic and continental lithosphere are  $-0.03/-0.004/0.023$  and  $-0.013/0.007/0.078$ , respectively.

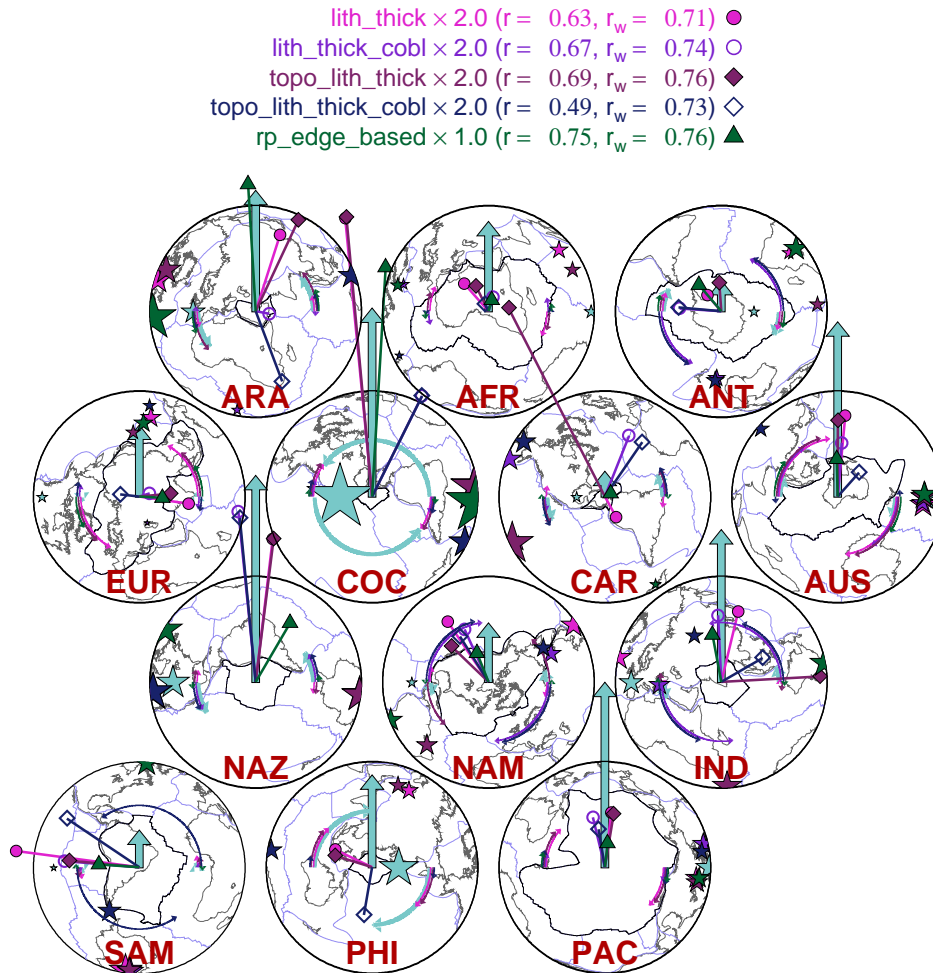


**Figure 4.** Lithospheric torques per plate area based on our lithospheric model (oceans only, lith\_thick, or whole Earth including continental topography, topo\_lith\_thick), *Coblentz et al.* [1994] (lith\_thick\_cobl and topo\_lith\_thick\_cobl), and our ridge push estimate from edge forces (section 3.5). We show NNR-NUVEL-1 plate motions (green, maps are rotated accordingly to aid comparison) and boundaries (blue); vectors indicate velocity/horizontal force if the Euler poles/torque vectors are evaluated at the plate centroid. The rotational component of the Euler pole/torque vector is indicated by two arc segments; while arc lengths have the same scaling in all plots, they are not drawn to scale compared to the force vectors. Also shown are the Euler/torque pole axes (stars); sizes scale with the magnitude. The legend lists torque scaling factors,  $w_i$ , and the overall (plate area weighted) correlation  $r$  ( $r_w$ ) of the normalized resolved forces and plate velocities at the centroid.

The predictions from our model are similar to those of *Coblentz et al.* [1994], especially for the torques that are based solely on oceanic lithosphere. There are some differences, however, and correlations of torque directions with NNR plate velocities are better (worse)

for *Coblentz et al.*'s [1994] model for oceanic-only (continental topography included) torques. Discrepancies might in part be due the plate boundaries used by *Coblentz et al.* which are somewhat different from ours (e.g., AUS/IND was treated as one plate). We have



attempted a first-order correction by scaling with modified plate areas when given, but some of the remaining differences might simply have a geometric origin.

[28] We furthermore find that the ridge push torques in Figure 4, which are based on parameterized edge forces, are similar to sea floor age derived lithospheric thickening. Ridge push actually leads to a better correlation with plate motions than the field derived torques. This implies that plate motion changes in the last 180 Ma have little effect with regard to integrated, age-based torques. For most plates with a substantial oceanic part, the resolved forces agree well with plate motions [cf. *Richardson et al.*, 1979; *Richardson*, 1992] although SAM and PHI are exceptions. For the latter plate, this might be due to the poorly constrained age structure.

[29] The correlation of resolved forces with NNR-NUVEL-1 velocities is one measure of the degree of alignment between torques and observed velocities, and it is appropriate to compare NNR reference frame derived torques with NNR plate velocities. However, if the model would be able to produce a net rotation of the lithosphere, other reference frames could be realized. We can indeed find a rigid body rotation such that the resulting correlations are improved up to  $r_w = 0.92$  for our and *Coblentz et al.*'s [1994] lithospheric thickening model. This optimal reference frame minimizes the motion of continental areas and causes the oceanic plate cooling derived torques to align better with absolute plate velocities.

[30] We note that the basic observation that the ridge-trench geometry is directly related to tectonic plate motions [*Gordon et al.*, 1978] explains the good correlation between all ridge push torques and plate velocities. This relationship makes it hard to distinguish between the

various contributions of driving forces, as we will discuss in section 3.5.

### 3.5. Plate Boundary Forces

[31] In addition to traction based torques, we also consider globally parameterized edge forces that act along plate boundaries. Such torques have been neglected in previous plate velocity inversions although they were included in force balance models [*Forsyth and Uyeda*, 1975; *Chapple and Tullis*, 1977; *Hager and O'Connell*, 1981]. On the basis of the classification by *Forsyth and Uyeda* [1975], we calculate the following contributions for all plates, listed in Table 2 (see Figures 1, A1, A2, and A3 for forces and plate boundary types):

$$\begin{Bmatrix} T_{\text{tft}} \\ T_{\text{tftw}} \end{Bmatrix} = C_1 \int_{\text{TF}} dl \left\{ \frac{\text{sgn}(v_t)}{v_r} \right\} (\mathbf{r} \times \hat{\mathbf{t}}) \quad (10)$$

$$T_{\text{tth}} = C_1 \int_{\text{TF}} dl \mathbf{r} \times \hat{\mathbf{n}} \quad (11)$$

$$\begin{Bmatrix} T_{\text{sp}} \\ T_{\text{spw}} \\ T_{\text{sdr}} \\ T_{\text{sdrw}} \end{Bmatrix} = \int_{\text{SP}} dl \begin{Bmatrix} -C_2 \\ -C_2 \sqrt{\frac{t[\text{Ma}]}{180}} \\ C_1 \\ C_1 \frac{v_n}{v_r} \end{Bmatrix} (\mathbf{r} \times \hat{\mathbf{n}}) \quad (12)$$

$$\begin{Bmatrix} T_{\text{crw}} \\ T_{\text{cr}} \\ T_{\text{crw}} \end{Bmatrix} = C_1 \int_{\text{TR}} dl \mathbf{r} \times \begin{Bmatrix} \hat{\mathbf{n}} \\ \hat{\mathbf{v}} \\ \frac{\mathbf{v}}{|\mathbf{v}|} \end{Bmatrix} \quad (13)$$

$$T_{\text{bas}} = -C_1 \int_{\text{OP}} dl \mathbf{r} \times \hat{\mathbf{n}} \quad (14)$$

$$T_{\text{rp}} = C_1 \int_{\text{SR}} dl \mathbf{r} \times \hat{\mathbf{n}} \quad (15)$$

Here  $\int dl$  means integration along the appropriate plate boundary segments,  $\hat{\mathbf{n}}$  and  $\hat{\mathbf{t}}$  are unit vectors normal and tangent to the boundary,  $\hat{\mathbf{v}}$  is the unity relative motion vector, and  $v_n$  and  $v_t$  are the relative motion components in the  $\hat{\mathbf{n}}$  and  $\hat{\mathbf{t}}$  directions, respectively (Figure 5). The boundary types are TF, transform fault; SP, trench, acting only

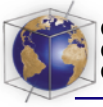


**Table 2.** Torque Type Abbreviations; Compare Equations (10)–(15)

Abbreviation	Definition
tft	transform fault tangential
tftw	weighted tft
tfn	transform normal
sp	slab pull
spw	weighted sp
sdr	subduction resistance
sdrw	weighted sdr
cr	colliding resistance
crnv	cr no velocity dependence
crw	weighted cr
bas	back-arc suction
rp	ridge push

at the subducting plate; TR, trench, at both plates; OP, trench, only at overriding plate; SR, spreading ridge.

[32] The force magnitudes are poorly constrained a priori; we have therefore chosen

the factors  $C_1 = 2 \times 10^{12}$  N/m and  $C_2 = 2 \times 10^{13}$  N/m, of the order of typical estimates for lithospheric thickening and slab pull, respectively [e.g., *Turcotte and Schubert, 1982*].  $C_1$  and  $C_2$  are also equivalent to the integrated strength of a plate margin with a yield stress of 200 MPa and depth extents of 10 and 100 km, respectively. We have chosen the signs of the edge forces such that sp, spw, bas, and rp are driving, and tft, tftw, tfn, sdr, sdrw, cr, crnv, and crw are resisting plate motion.

[33] We numerically compute the integrals in (10)–(15) along the NUVEL-1 boundaries using segment lengths of  $0.2^\circ$ . Since plate boundaries and Euler poles are better determined now than 25 years ago, our torques should be an improvement over the work of *Forsyth and Uyeda [1975]*. There is, however, some arbitrariness in the definition of the

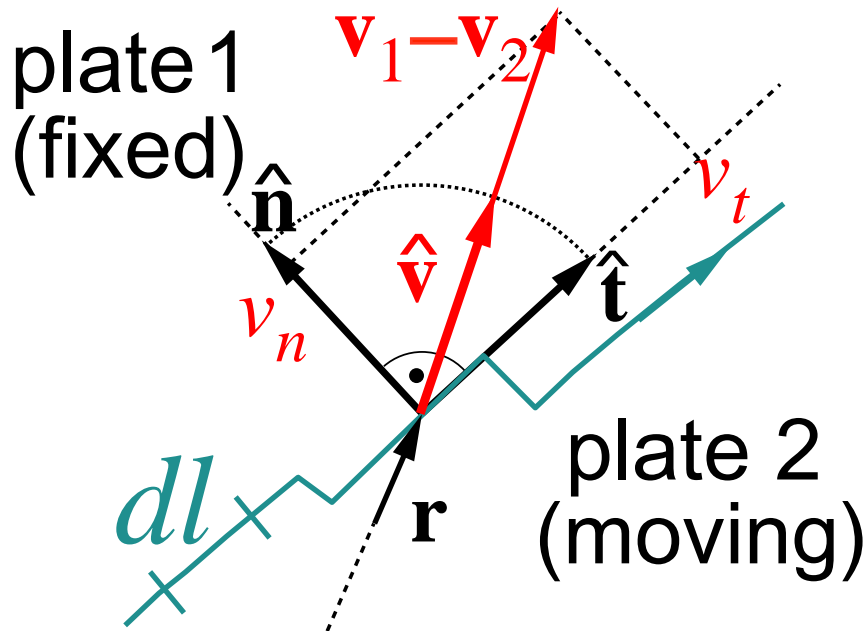
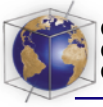


**Figure 5.** Geometric quantities for the integration of edge forces acting on Plate 1.



margin types: Our rule for discerning between transform and convergent/divergent margins is that boundaries are of the transform type when relative motion is at an angle smaller than  $25^\circ$  to the tangential. We use the RUM Wadati-Benioff zone model to decide if the plate boundary is converging with or without a seismic slab and which plate is subducting. For spw, we need the seafloor age at the trench which is poorly constrained at some subduction zones [cf. *Müller et al.*, 1997]. We therefore extrapolate ages based on the 3SMAC model. All relative velocities  $\mathbf{v}_1 - \mathbf{v}_2$  are calculated from NUVEL-1 and are then used to calculate edge torques for plate motion inversions. If those torques depend on the observed velocities, this procedure is not self-consistent. However, as we show in section 4.2.4, parameterized edge forces do not improve the plate motion fit significantly. Thus we will not attempt to find a more consistent solution by including the velocity dependent torques on the left hand side of (1).

[34] Figure 6 shows a comparison between some of the edge torques. A quantitative analysis of the interdependence of the different forces can be done by calculating the correlation matrix of the torque vectors. *Forsyth and Uyeda* [1975] pointed out that the strongest (anti-)correlation is that between the slab pull (sp) and the weighted subduction resistance at the trench (sdrw). If we consider (12), it is clear why this is the case: sp and sdrw are derived from integrating the same plate boundaries; their only difference is the prefactor,  $C_1 v_n / v_n^{\max}$  for sdrw. If the small deviations that are introduced by the velocities are neglected, sp and sdrw are exactly anti-correlated. The dominance of such strong correlations between different components of the plate-driving force inversion has been noted before [*Forsyth and Uyeda*, 1975; *Backus et al.*, 1981], but it is worthwhile to point out that they are simply geometric in

origin. Any force balance model that is based on similar integration rules will be dominated by plate geometry effects that render the analysis of the physical processes at plate boundaries extremely difficult.

[35] Figure 7 shows the correlations for some of the edge and area-based torques: “plate\_motion\_D” is the viscous drag resistance to plate motion that we find for a 3-D flow calculation using viscosity profile  $\eta_D$  (see section 4) and prescribing the NUVEL-1 NNR plate motions,  $\mathbf{v}_{\text{NNR}}$ , at the surface (see section 4.2.1). In comparison, we can resort to a simplified estimate of the viscous drag by assuming that tractions are given directly by  $-\mathbf{v}_{\text{NNR}}$ , either underneath all plates (“visc\_drag\_nnr”) or only under cratons (“visc\_drag\_nnr\_craton”). It has been pointed out that these viscous drags are not identical [*Hager and O’Connell*, 1981] and Figure A4 shows that deviations vary between plates, being strongest for SAM, NAM, EUR, and ARA. In Figure 7, we also show correlations for driving torques for rum (“rum\_D”) and tomographic model s20rts (“s20rts\_whole\_mantle\_D”) that can be compared to the edge based slab pull (sp), the lithospheric thickening (“lith\_thick”), and the ridge push edge force (rp). This analysis shows that only the suction force (bas) and the force that is normal to transform faults (tfn) do not consistently correlate with any of the other forces. It also implies that a number of different models of driving forces can be expected to yield good plate motion fits.

## 4. Results and Discussion

[36] We now discuss flow-model based torques which represent the driving effect of the mantle. Subsequently, we will use these torques in plate motion inversions. At this point, we do not invert for other geophysical observables such as the geoid or intraplate stresses but use typical scalings and viscosity profiles that have

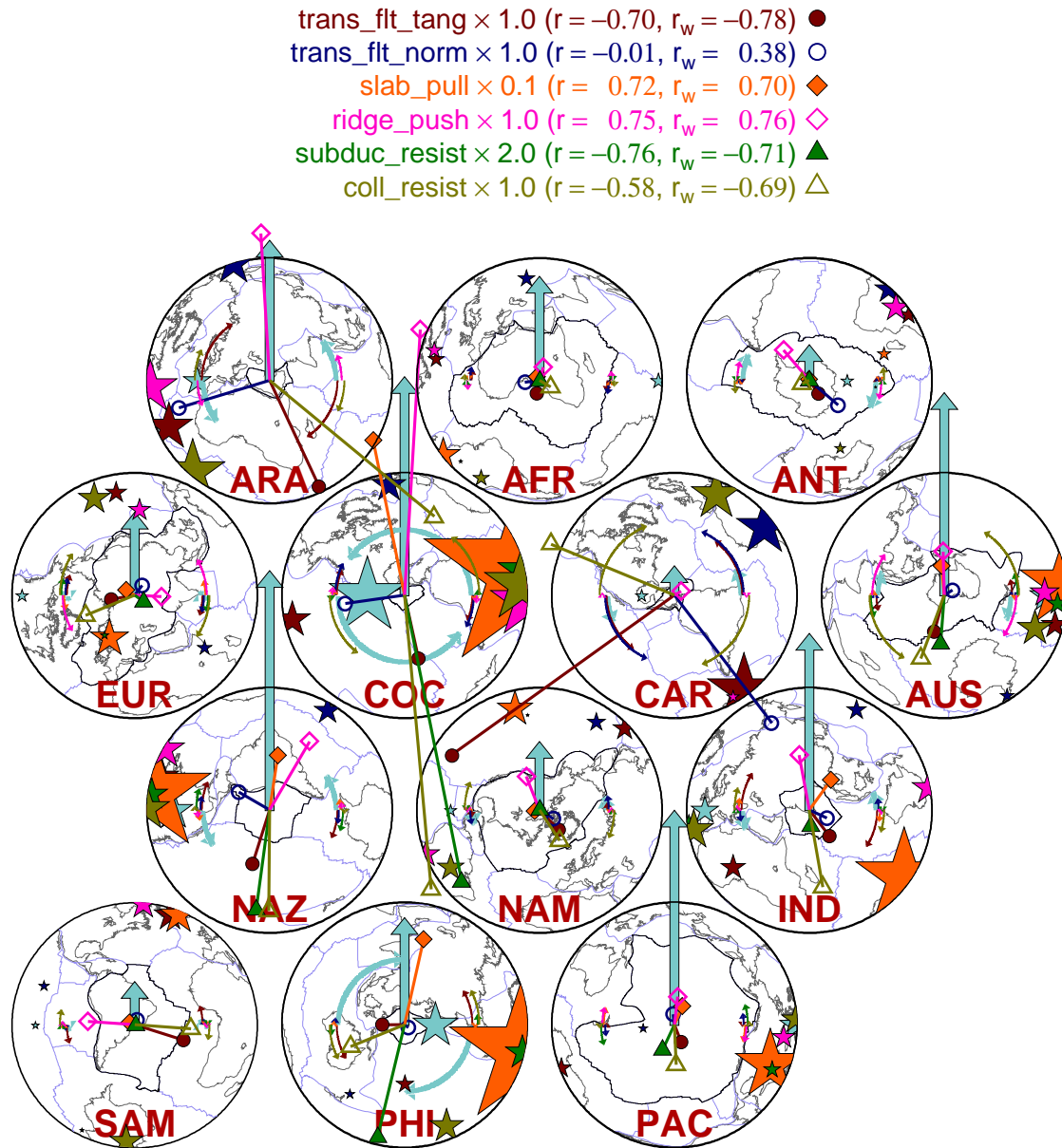
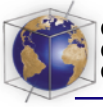
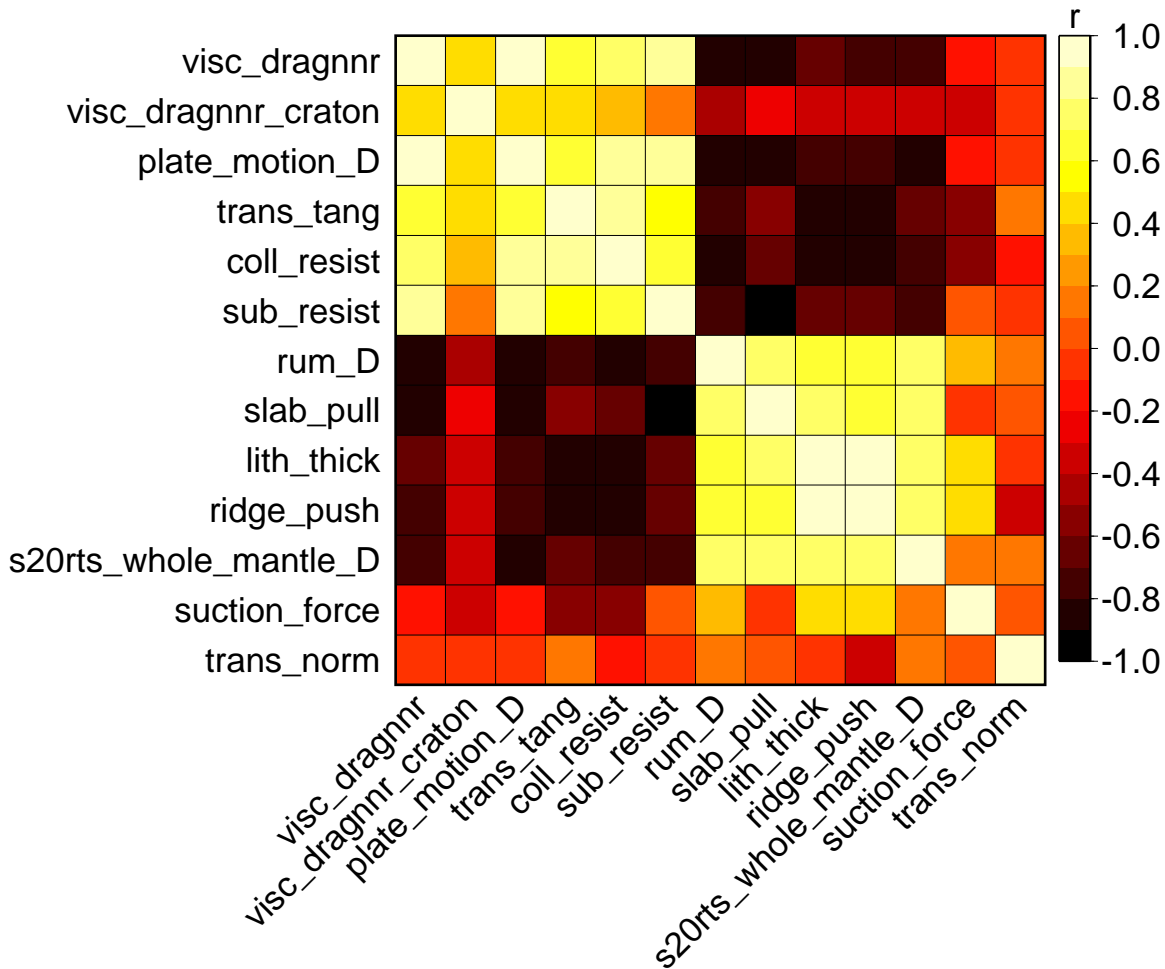
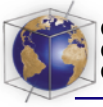


Figure 6. Comparison of edge force derived driving torques; for explanation see Figure 4.

been determined by other studies. Figure 8 shows the viscosity structures we consider:  $\eta_C$  is a generic model with an increase in viscosity in the lower mantle,  $\eta_D$  has an asthenospheric channel,  $\eta_E$  a weaker lithosphere than  $\eta_C$ ,  $\eta_F$  has been used by Steinberger [2000] for

stb00d, and  $\eta_G$  and  $\eta_H$  are from an inversion by Mitrovica and Forte [1997]. Profile  $\eta_E$  is similar to the best-fit viscosity structure from Lithgow-Bertelloni and Richards [1998] and has the factor 50 increase in the lower mantle as used to construct lrr98d. We will discuss



**Figure 7.** Correlation matrix for driving and resisting torques calculated by comparing the 3*N* components of the torque vectors.

model resolution with respect to viscosity structure in section 4.2.1.

#### 4.1. Mantle Driving Torques

[37] Figure 9 shows an example of driving torques that result from flow-models; we have used viscosity model  $\eta_D$  and the density models as described in section 3. We note that using slab model derived torques that are based on viscosity structures other than that used in the slab advection calculations itself (upper/lower

mantle jump as in  $\eta_E$  for lrr98d,  $\eta_F$  for stb00d) is slightly inconsistent. Deviations should be small, however, as we will see in section 4.2.1. The whole-mantle torques of Figure 9 can be compared with Figure 10, which shows the torques that result from lower mantle structure only.

[38] Table 3 gives the average fraction of the torque contribution of the lower mantle when we use different viscosity profiles. We use two measures for the strength of the driving

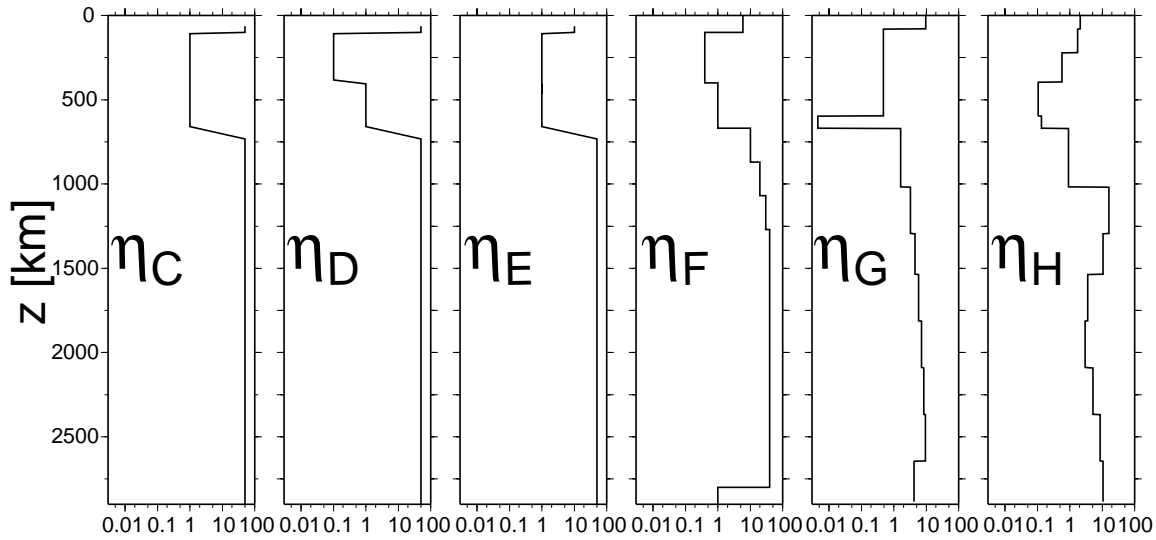
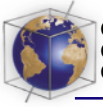


Figure 8. Viscosity profiles as used in the flow-models, units are  $10^{21}$  Pas.

forces: mean absolute torque,  $\hat{T}_{\text{abs}}$ , which is obtained by averaging all local torque magnitudes,  $|\mathbf{T}|$ , on the surface of the Earth ( $\hat{T}_{\text{abs}}$  is Earth's radius times the mean horizontal traction magnitude), and average torque,  $T_{\text{avg}}$ , which is determined by plate-area weighted averaging of the integrated plate torques.  $T_{\text{avg}}$  contains information about the current plate geometry. We find that a substantial fraction ( $\sim 70\%$ ) of the absolute mantle based torques on the plates results from lower mantle structure (comparable to the volumetric fraction of the lower mantle, 66%), with small variations with the viscosity structure and moderate dependence on the model type. Model lr98d's lower mantle fraction is the largest overall; this is likely due to the strong increase in the density heterogeneity signal from upper to lower mantle [Lithgow-Bertelloni and Richards, 1998; Becker and Boschi, 2001].

[39] Figure 9 indicates that, for some plates, different mantle models result in substantial variations in driving torque directions. For the

smaller plates, such as ARA, COC, and CAR, Figure 9 emphasizes these differences since we normalize by the plate area, and small plates are also at the limit of our model resolution. In general, however, correlations between resolved forces and plate velocities are again found to be good (AFR, CAR, NAM, and SAM being the exceptions). They are best for geodynamic models ( $r_w \approx 0.83$ ), slightly poorer for  $s$  wave models ( $r_w \approx 0.67$ ), and poorest for  $P$  wave models ( $r_w \approx 0.29$ ).

[40] We can compare the global correlation of individual torques (Figure 11) with the correlations between the input models (Figure 2) to observe that the driving torques show a higher correlation with each other than do the input models. This can be expected since torques are integrated tractions and are therefore smoother than the density variations. We also find that  $s$  wave and subduction model derived torques are more similar than  $P$  wave model torques, an observation that is mirrored in the model performance in terms of plate motion inversions (see section 4.2.3). The reason for

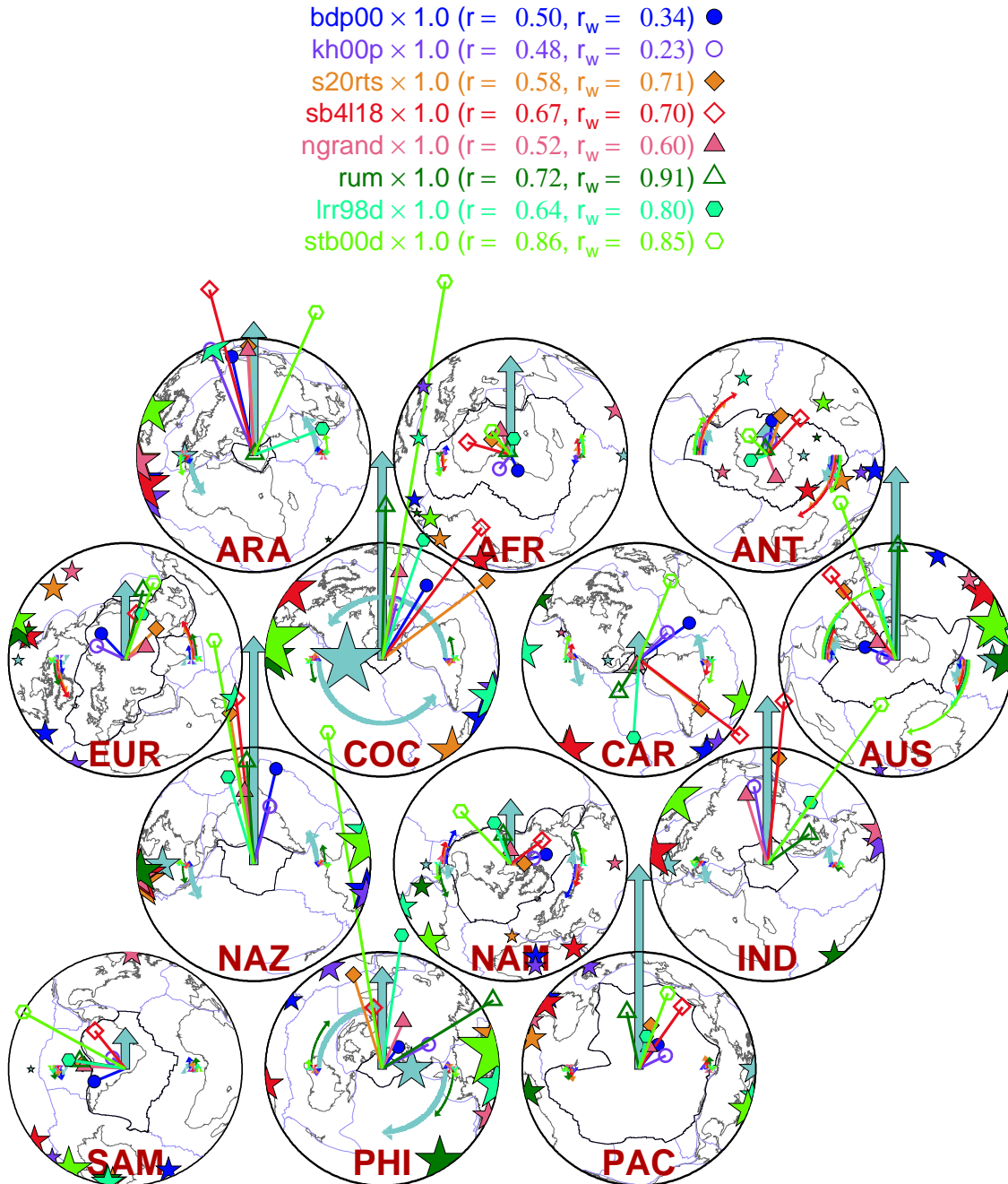
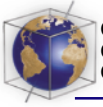


**Figure 9.** Comparison of mantle based driving torques for viscosity profile  $\eta_D$ . For explanation see Figure 4.

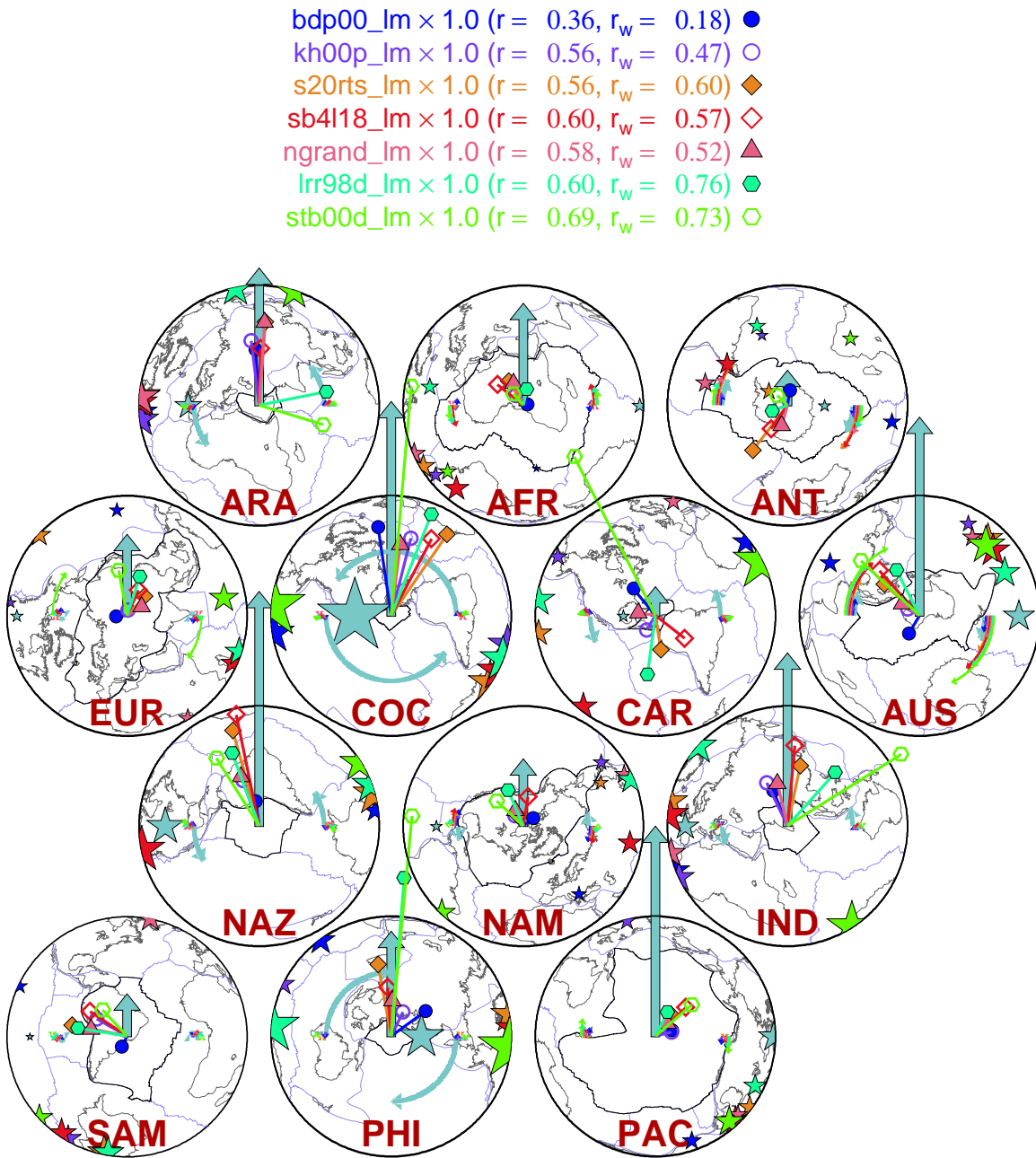
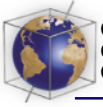


**Figure 10.** Comparison of lower mantle based driving torques for viscosity profile  $\eta_D$ ; compare with Figure 9, and see Figure 4 for explanation.

this appears to be structure in the upper mantle that is important for slab pull forces. While  $P$  wave tomography images slabs in some subduction zones [e.g. *van der Hilst et*

*al.*, 1997], other seismically fast structure in the  $P$  models, mostly correlated with cratons, probably offsets the upper mantle slab signature when tomography is scaled to density

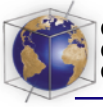


**Table 3.** Average  $\pm$  Standard Deviation of the Fractions of  $\hat{T}_{\text{abs}}$  and  $T_{\text{avg}}$  That are Caused by the Lower Mantle for Different Viscosity Profiles  $\eta_i$  as in Figure 8

model	$\bar{T}_{\text{abs}}, \%$	$T_{\text{avg}}, \%$
bdp00	59 $\pm$ 7	52 $\pm$ 6
kh00p	59 $\pm$ 2	68 $\pm$ 6
s20rts	68 $\pm$ 2	71 $\pm$ 2
sb4l18	68 $\pm$ 5	69 $\pm$ 5
ngrand	74 $\pm$ 3	85 $\pm$ 2
lrr98d	91 $\pm$ 1	84 $\pm$ 1
stb00d	63 $\pm$ 4	56 $\pm$ 4

anomalies. The  $S$  wave models have a more even data coverage in the upper mantle since they can rely on surface wave observations which are not limited by the ray path incidence which is nearly vertical at shallow depths [e.g., *Becker and Boschi, 2001*].

## 4.2. Plate Motion Inversions

[41] We have conducted numerous plate velocity inversions using different combinations of input models and viscosity structures and will now describe some of the successful models. By introducing different types of driving forces step by step, we attempt to develop a deeper understanding of their role in driving the plates and try to assess which degree of model complexity is warranted.

### 4.2.1. Effect of Viscosity Structure

[42] An increase of mantle viscosity with depth is likely [e.g., *Hager, 1984; Hager and Clayton, 1989; Mitrovica and Forte, 1997*] and plate velocities have indeed been used to deduce such an increase [*Forte and Peltier, 1987*]. The differences between our radial viscosity profiles (Figure 8) are therefore of second order compared to this general trend; consistent with *Lithgow-Bertelloni and Richards [1998]*, we find that the inversions are insensitive to such details.

[43] If we use our starting values for the scaling factors (Figure 12), we observe that viscosity profiles  $\eta_D$ ,  $\eta_G$ , and  $\eta_H$  lead to the best mean model performance in terms of  $r_w$ . Individual best models lead to velocity predictions that are correlated as  $r_w \approx 0.9$  with NUVEL1-NNR. If the scalar prefactors of the driving and resisting torques are optimized to reduce the misfit in plate motion predictions (see section 2.4), the performance of the models is as shown in Figure 13. We see that all combinations of models and viscosity profiles can be adjusted to yield good fits, that there is not much variation with respect to mean model correlation,  $\hat{r}_w$ , and that the best models of each  $\eta$  type all give  $r_w \approx 0.9$  with best overall results for  $\eta_D$ ,  $\eta_G$ , and  $\eta_H$ . This implies that our original choices for scaling factors led to reasonable plate motion predictions, especially for viscosity profiles of the  $\eta_D$  type. The mean  $\hat{r}_w$  of optimized models is, however, in general  $\approx 0.07$  higher than the nonoptimized models (compare Figures 12 and 13).

[44] If we compare optimized and nonoptimized variance reduction histograms (Figure A5 and Figure A6), we can see that improvements in mean VR vary by a larger extent between  $\eta$  structures than for  $r_w$ , and adjustment of scaling factors leads to a larger improvement for VR overall. For  $\eta_G$  and  $\eta_H$ , mean VR is improved substantially over fixed weight models. Since variance reduction is affected by the plate velocity magnitude and not only the directions, as is the case for  $r_w$ , this implies that we have some resolution in terms of the absolute value of the viscosity,  $\eta_0$ , which controls the viscous drag amplitudes [*Forte et al., 1991; Lithgow-Bertelloni and Richards, 1998*]. In particular, viscosity profile  $\eta_G$  leads to models whose velocities are too high such that the optimized viscosity  $\eta_0$  is increased by a factor of  $\sim 3$  (see Table A2).

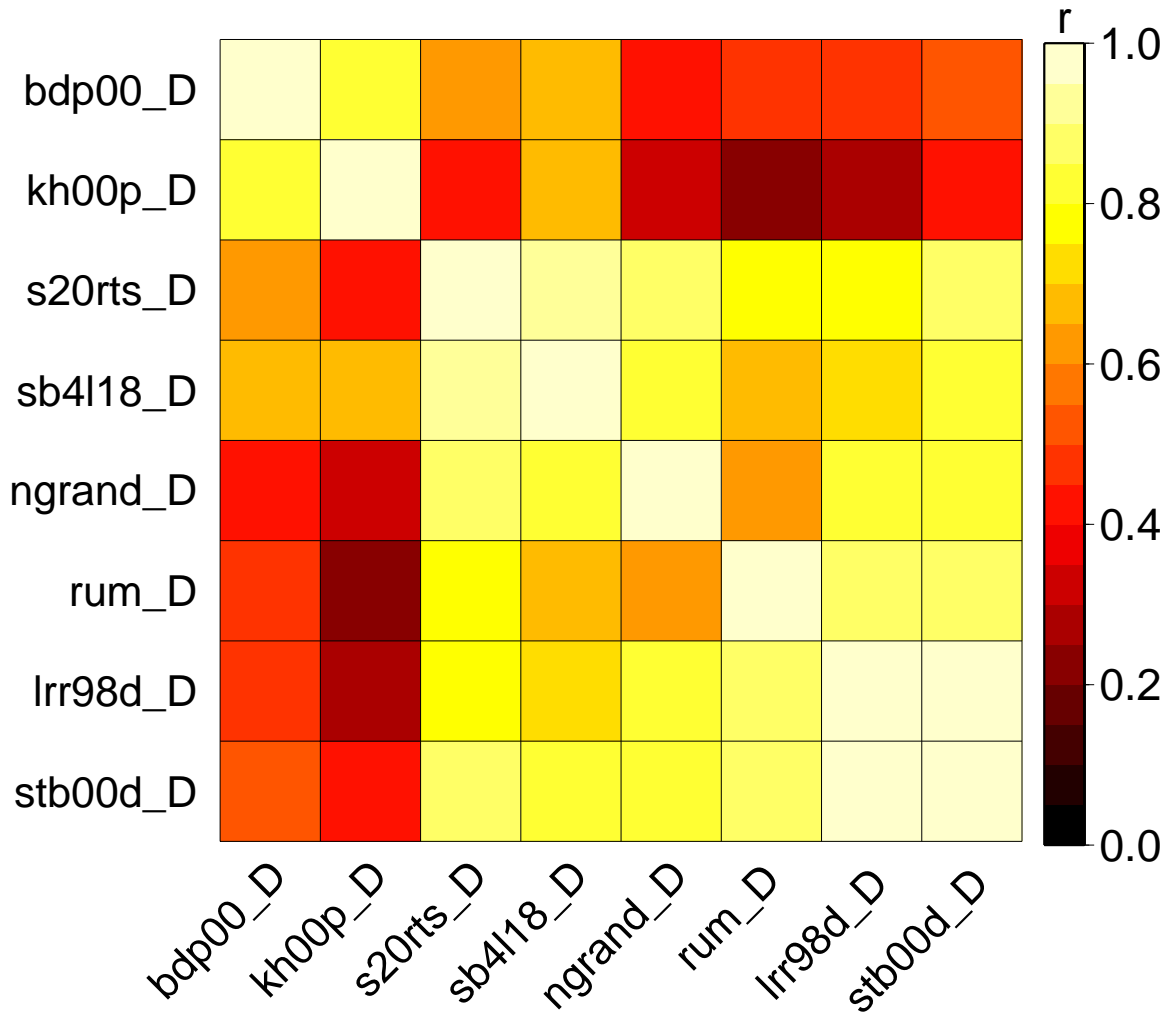
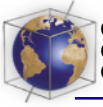


**Figure 11.** Correlation matrix for driving torques based on whole mantle density models and flow calculations with  $\eta_D$ .

[45] The finding that predicted plate motions are insensitive to the depth dependence of  $\eta$  is consistent with work by *Lithgow-Bertelloni and Richards* [1995] who explored the role of a low viscosity asthenospheric channel similar to that in our profile  $\eta_D$ . Such a decoupling zone could be expected to diminish the plate-driving force of the mantle. However, *Lithgow-Bertelloni and Richards* showed that a viscosity drop of several orders of magnitude will still lead to large mantle contributions,

and some of our best fitting models actually have such low viscosity channels ( $\eta_D$  and  $\eta_G$ ). The explanation for this apparent paradox is conservation of mass: while a low viscosity channel will reduce the shear stresses that are transmitted across such a zone, radial flow will maintain communication between the layers. Figure 14 explores this: we studied the effect of models with only lower mantle density variations (based on bdp00, ngrand, s20rts, and lrr98d) on the

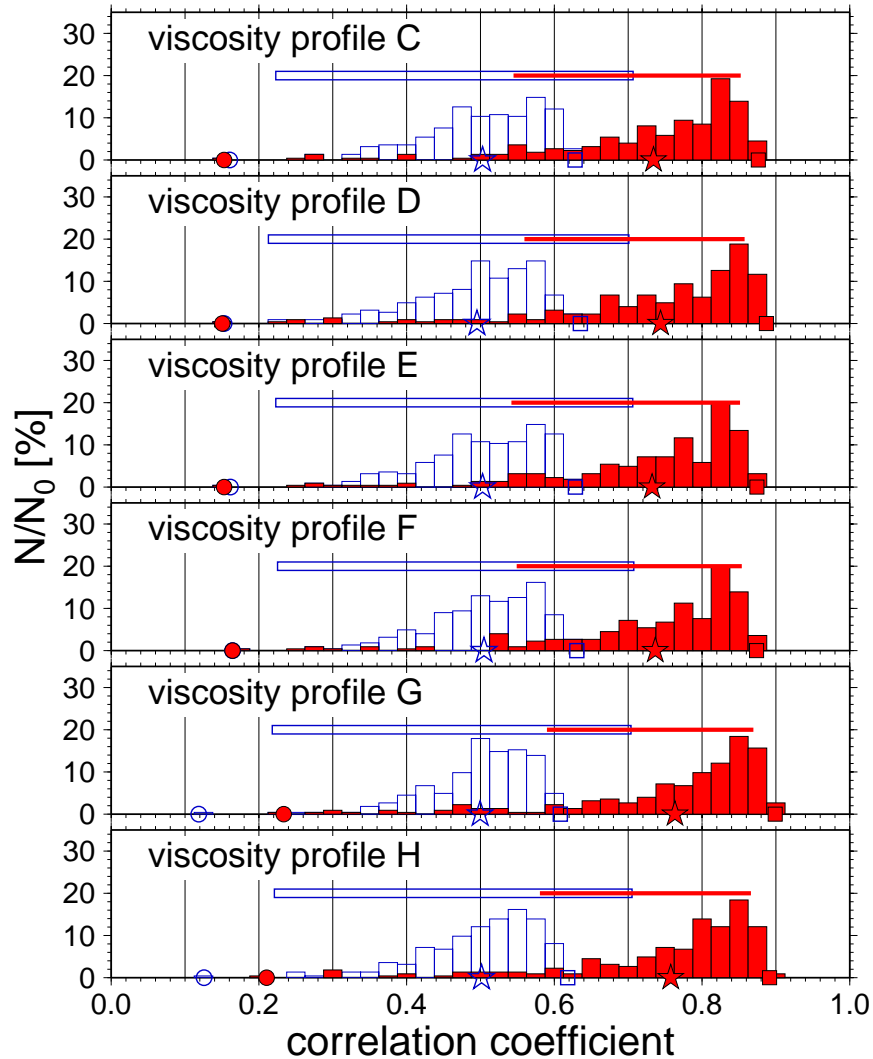
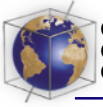


**Figure 12.** Histogram of nonoptimized model performance as a function of  $r$  (open bars) and  $r_w$  (solid bars).  $N/N_0$  denotes the fraction of all models that fall into a certain quality bin when models are sorted by viscosity structure. Circles, stars, and boxes indicate minimum, mean, and maximum performance of the models, respectively. Horizontal bars centered on the mean indicate the 95% confidence interval were the mean  $r$  the true correlation of the inversion, determined from Fisher's  $z$  transformation [e.g., Press *et al.*, 1993]. Variations are small between results with different viscosity profiles. (Compare Figures 13, A6, and A5).

magnitude (RMS) of the radial flow through the transition zone at 660 km,  $u_r^{660}|_{\text{RMS}}$ , and the torques on the plates when the viscosity of the lower mantle,  $\eta_{\text{lm}}$ , is varied for an  $\eta_E$ -type viscosity profile. As expected, radial flow decreases when convection becomes

more sluggish in the lower mantle; we can fit all models with a power law  $u_r^{660}|_{\text{RMS}} \propto \eta_{\text{lm}}^{-0.62}$  (Figure 14, top). Correspondingly, the torque amplitudes are smaller, and for the average plate-integrated torques,  $T_{\text{avg}}$ , we fit  $T_{\text{avg}} \propto \eta_{\text{lm}}^{-0.29}$  (Figure 14, bottom).

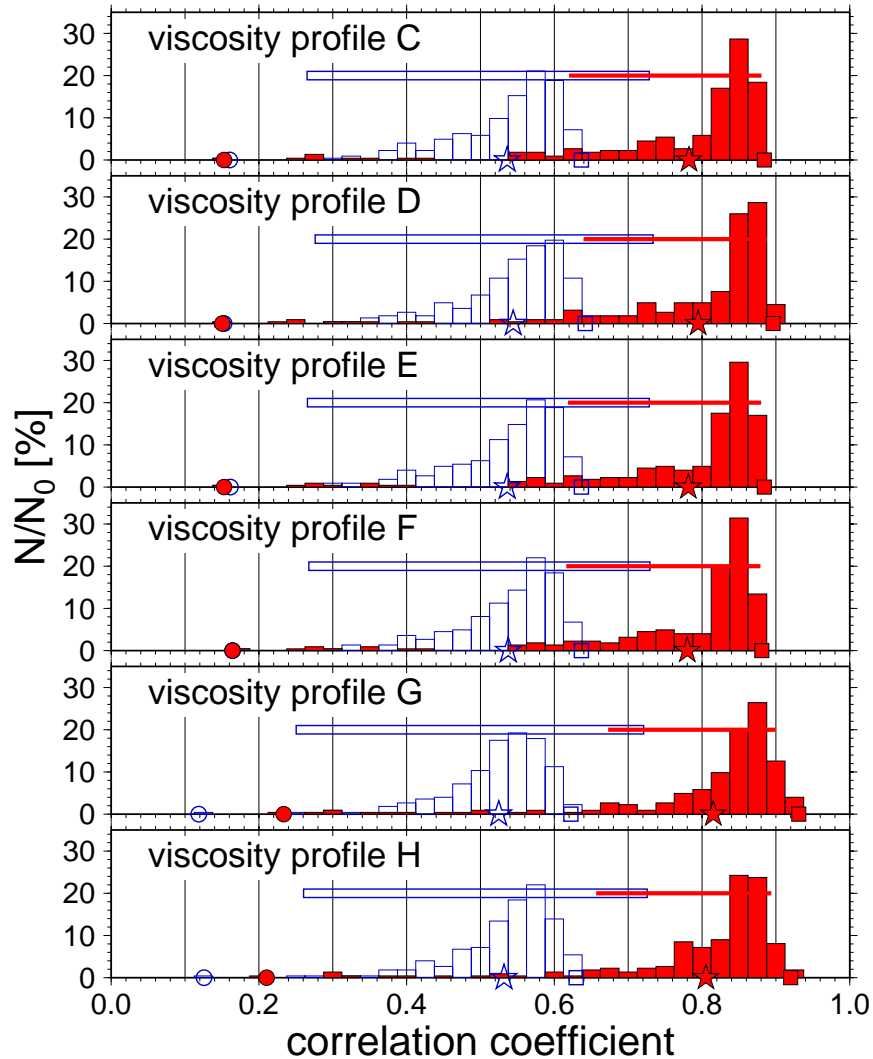
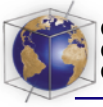


**Figure 13.** Histogram of optimized model performance in terms of correlation. In contrast to Figure 12, all scaling factors,  $w_i$ , were allowed to vary. All viscosity profiles give similar results.

[46] The considerations above hold for constant density anomalies in the lower mantle. As noted before,  $\eta_{lm}$  strictly cannot be varied independently for geodynamic models like lrr98d since the density field of those models depends on the viscosity structure itself. For lrr98d, we can estimate that the total slab density that can be sustained will scale with the inverse of the sinking velocity of subducted material in the

lower mantle since the influx is constrained by the plate tectonic reconstruction. Depending on the functional relationship between the sinking velocity and  $\eta_{lm}$ , we can therefore expect that the decrease of  $T_{avg}$  with increasing  $\eta_{lm}$  will be diminished from that shown in Figure 14. However, torques due to lower mantle density are always large when compared, for example, to those due to lithospheric thickening. Independ-

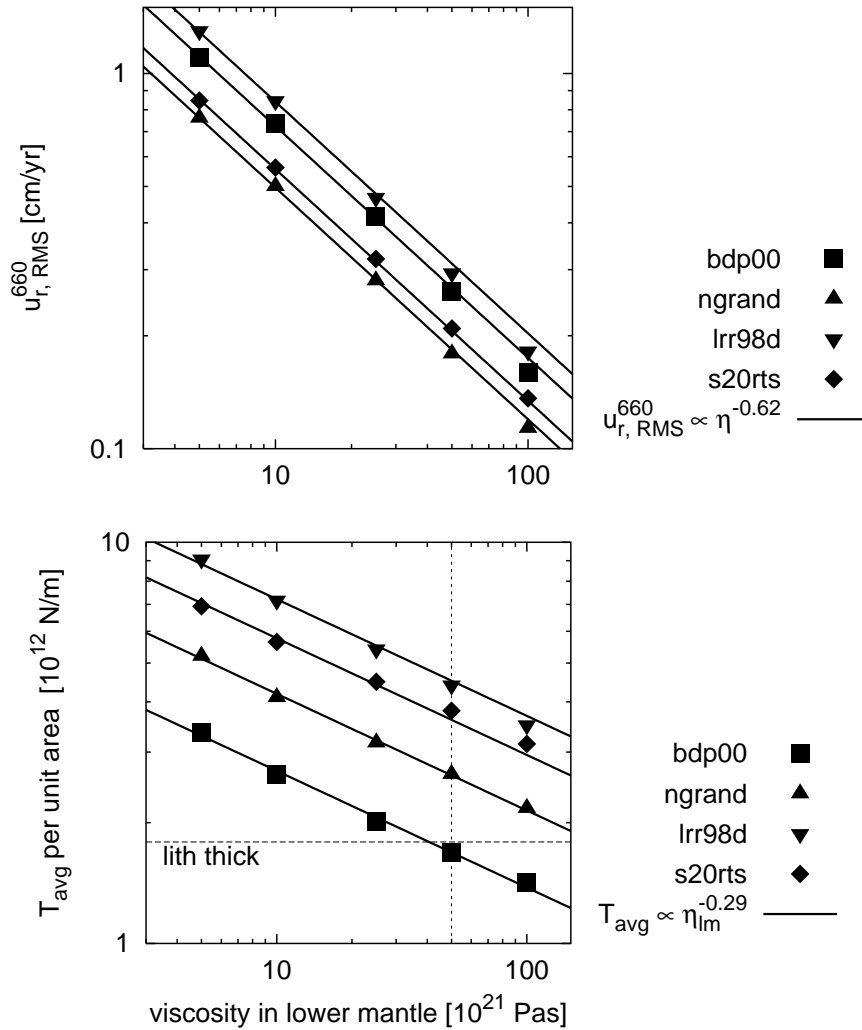
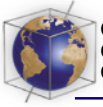


**Figure 14.** (top) RMS of the radial velocity,  $u_r^{660}|_{RMS}$ , driven by lower mantle only density models in a no-slip surface boundary condition flow-model and (bottom) plate averaged torques per area,  $T_{avg}$  as a function of lower mantle viscosity  $\eta_{lm}$  for  $\eta_E$  type profiles. Horizontal dashed line indicates the lithospheric torque contribution from our model, and vertical dotted line indicate  $\eta_{lm} = 50$ , as used in the construction of lrr98d.

ent of the absolute magnitude of  $T_{avg}$ , we find that the torques relate to the flow through the transition zone roughly as  $T_{avg} \propto \sqrt{u_r^{660}|_{RMS}}$  for the current plate geometry; this appears to be valid for many density models. Our results therefore illustrate how lower mantle density variations can play a role in driving the plates in any style of convection that allows for substantial mass flux through 660 km, as is likely the

case for the present-day Earth [e.g., *van der Hilst et al., 1997; Grand et al., 1997; Puster and Jordan, 1997*].

#### 4.2.2. Lithosphere and Upper Mantle Driving Forces Only

[47] For the discussion of the best fitting models of plate motions in terms of model quality

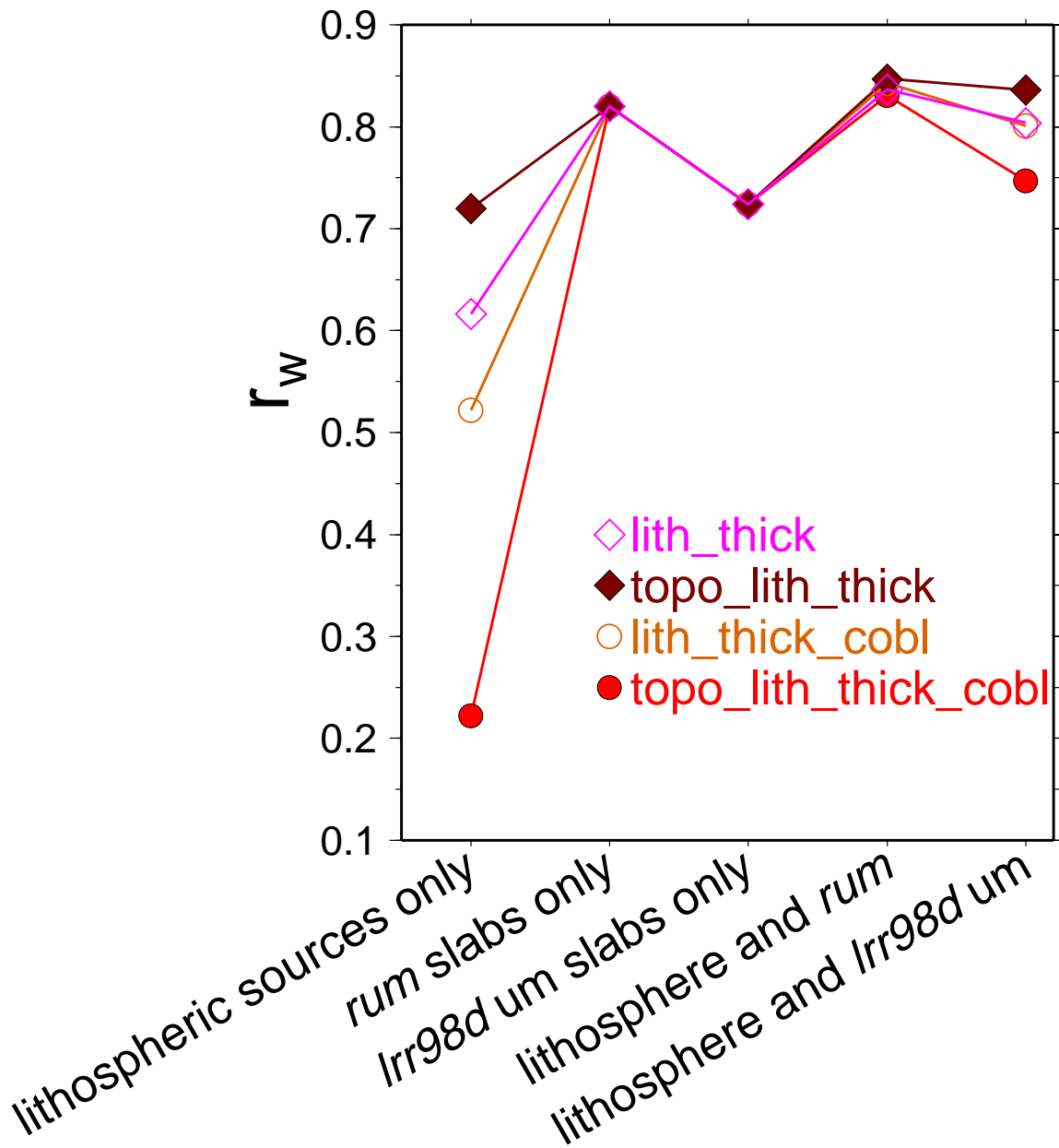
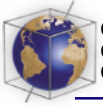


**Figure 15.** The  $r_w$  for best-fit models using viscosity profile  $\eta_D$  and lithospheric driving forces only, upper mantle seismic slabs from rum only, upper mantle “total” slabs from lrr98d only, lithosphere plus rum, and lithosphere plus lrr98d upper mantle slabs.

we fix the viscosity structure to be  $\eta_D$ . While  $\eta_G$  yields results that are slightly better most of the time, we constrain ourselves to the simpler viscosity profile since we have seen that differ-

ences are small. We also proceed to show models with adjusted, nonnegative scalar torque weights  $w_i$  but, as discussed in section 4.2.1, optimization gains are small, too.

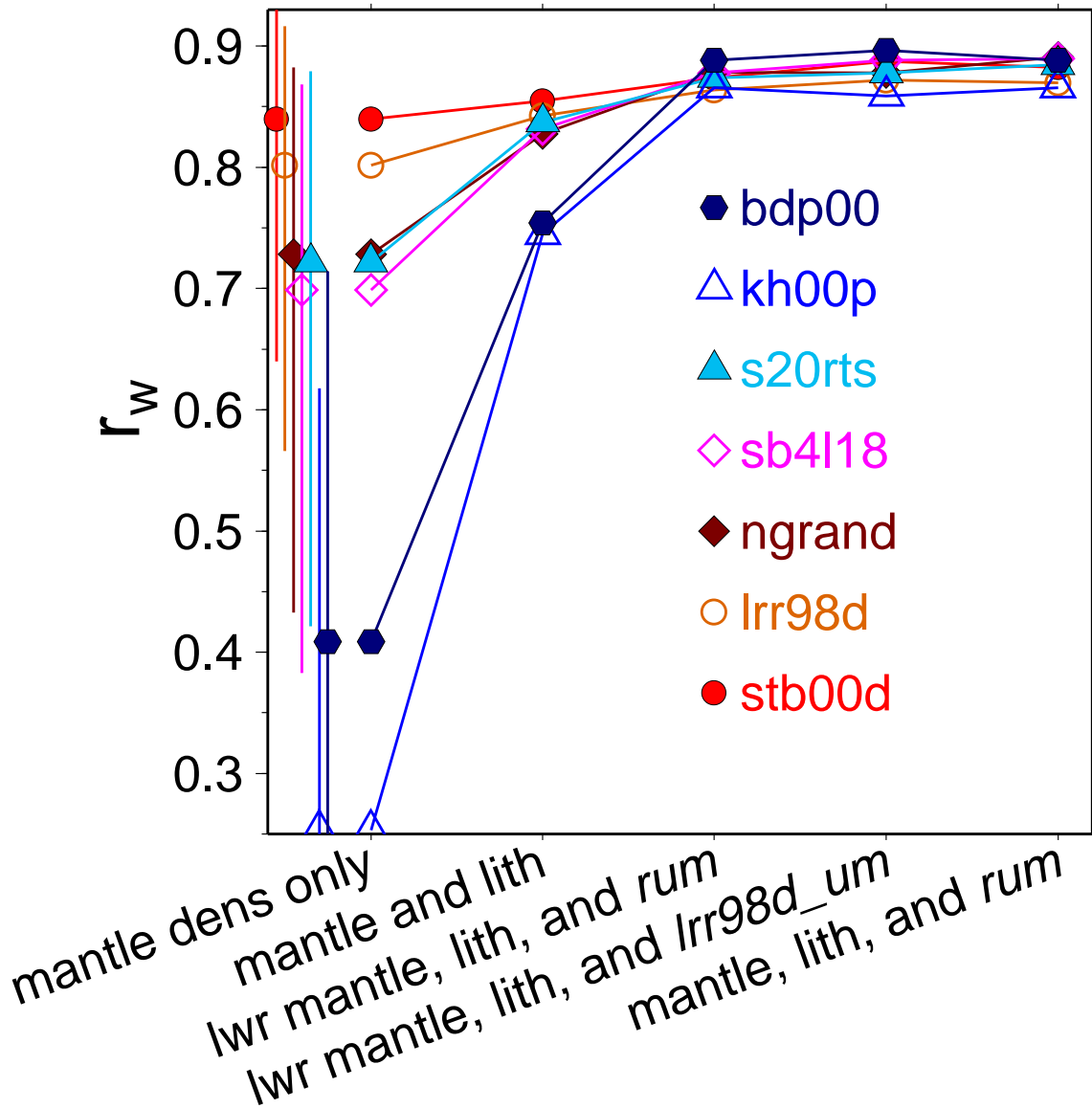
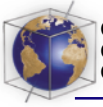
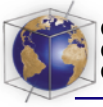


**Figure 16.** The  $r_w$  for best-fit models with mantle density driven flow and  $\eta_D$ . Error bars on the left indicate the range outside which models can be considered significantly better or worse than mantle only models at the 95% confidence level according to Fisher's  $z$  transformation.

[48] First we present models that are based on lithospheric structure only, testing the hypothesis that lithospheric thickening forces alone counterbalance the viscous drag due to plate motion. Figure 15 shows the quality of plate velocity fit for a combination of driving tor-

ques. We find that our lithospheric model ("lith\_thick") performs better if tested against *Coblentz et al.*'s [1994] model ("lith\_thick\_cobl") for lithospheric thickening only ( $r_w = 0.62$  vs.  $r_w = 0.52$ ). Models that further include continental topography ("topo\_lith\_thick")



$$r = 0.60 \quad r_w = 0.89 \quad VR = 31.6\% \quad VR_w = 79.1\%$$

viscosity profile D  
viscous drag  $w_1 = 0.69$   
sb4118\_whole\_mantle\_D  $w_2 = 0.27$  (38%)  
lith\_thick\_cobl  $w_3 = 0.39$  (20%)  
rum\_slabs\_D  $w_4 = 0.55$  (42%)

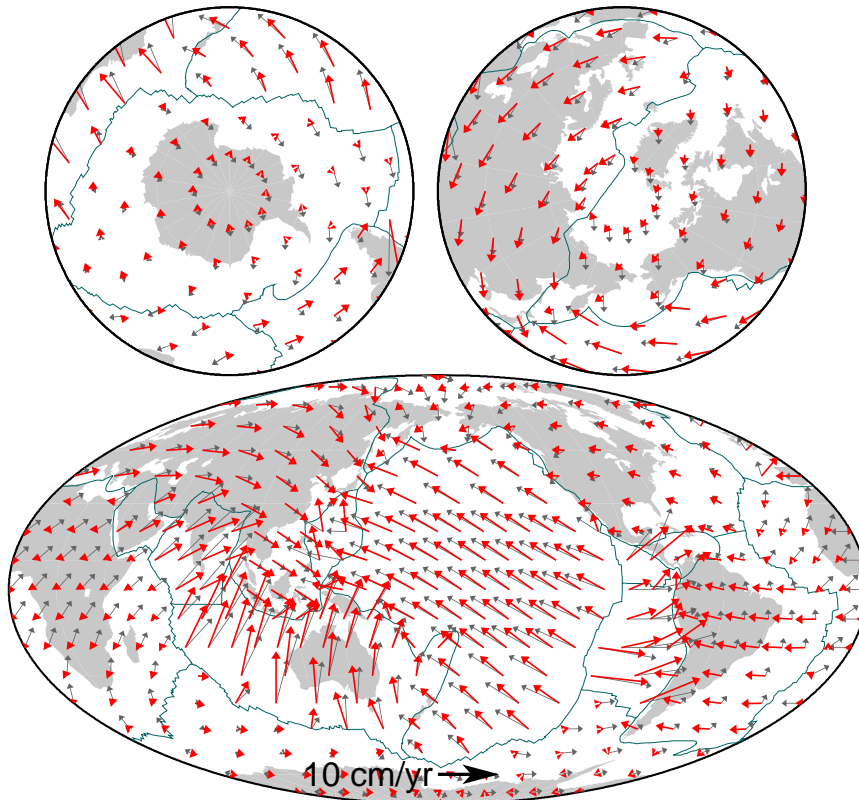
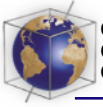


**Figure 17.** Predicted plate velocities (red, thick vectors) based on the best fitting  $S$  wave model for  $\eta_D$ , sb4118, and observed NNR-NUVEL-1 velocities (gray, thin vectors). The  $w_i$  values indicate the scalar factors that were adjusted to minimize the misfit. If we assume that the lithospheric model is best constrained ( $w_3 \equiv 1$ ), the absolute viscosity of  $\eta_D$  should be scaled by 1.78, and mantle and slab density fields should be scaled by 0.7 and 1.41, respectively. (See also Table A2.) Numbers in parentheses are the relative contributions of the driving torques to  $T_{\text{avg}}$ .

are not necessarily in better agreement with plate motions than oceanic plate only models; while topography-included torques yield better results for our model ( $r_w = 0.72$ ), the opposite is true for *Coblentz et al.*'s [1994] torques ( $r_w = 0.22$ ).

[49] We next consider only slab pull driving plate motions, in the form of rum, our

seismic slab model, or the upper mantle part of lrr98d, as an approximate "total" upper mantle slab model. With viscosity  $\eta_D$ , we achieve  $r_w = 0.82$  for rum which is not much lower than the fit for more complex models. Upper mantle slabs based on lrr98d lead to a poorer performance than rum. If we combine rum or upper mantle lrr98d slab pull with the lithospheric models, the fit to plate motions is



**$r = 0.56$   $r_w = 0.86$   $VR = 26.5\%$   $VR_w = 74.1\%$**

viscosity profile D

viscous drag  $w_1 = 0.69$

lrr98d\_whole\_mantle\_D  $w_2 = 0.46$  (44%)

lith\_thick\_cobl  $w_3 = 0.25$  (15%)

rum\_slabs\_D  $w_4 = 0.50$  (41%)

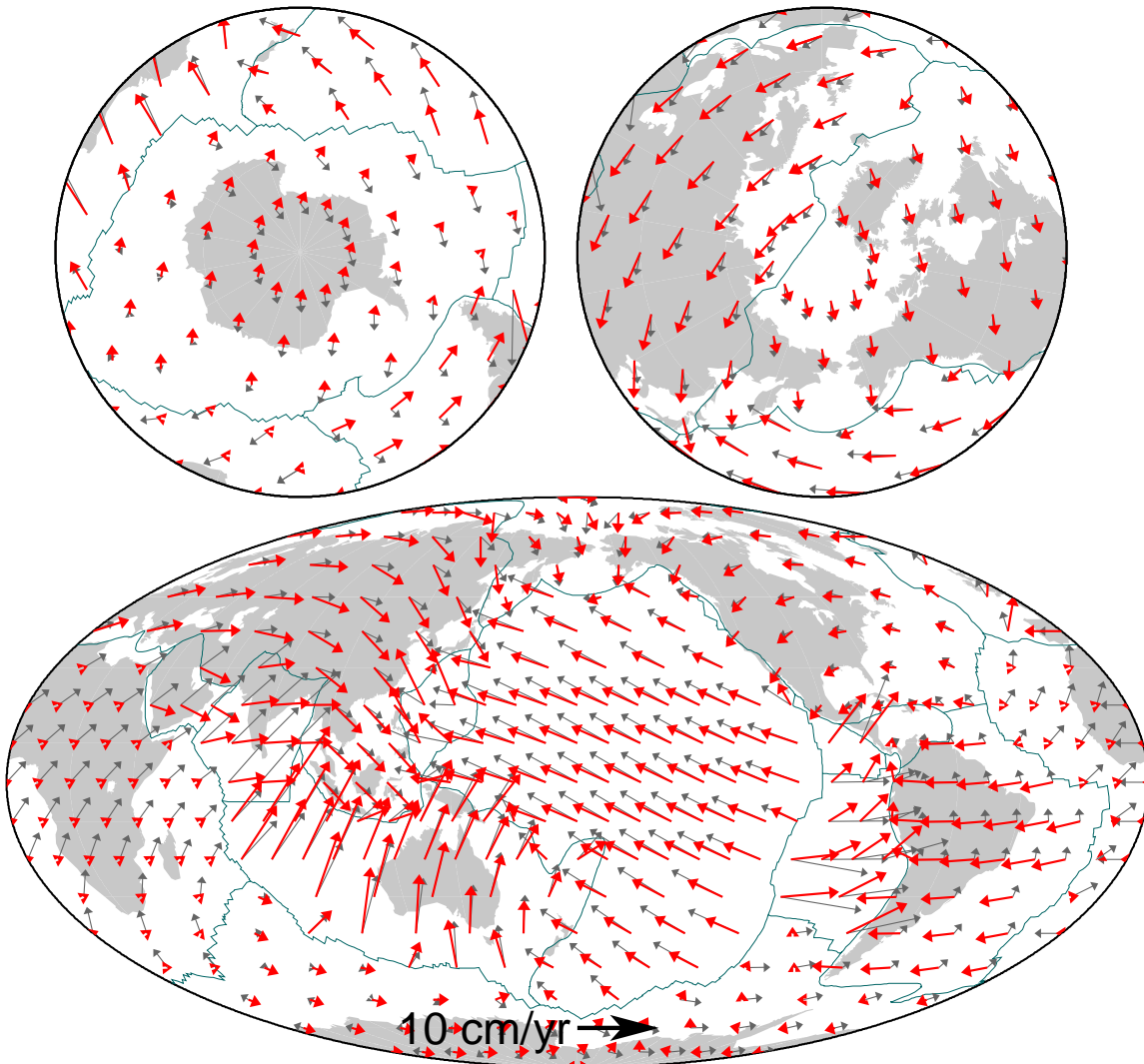


**Figure 18.** Predicted and observed plate velocities based on geodynamic model lrr98d for  $\eta_D$ , compare Figure 17.

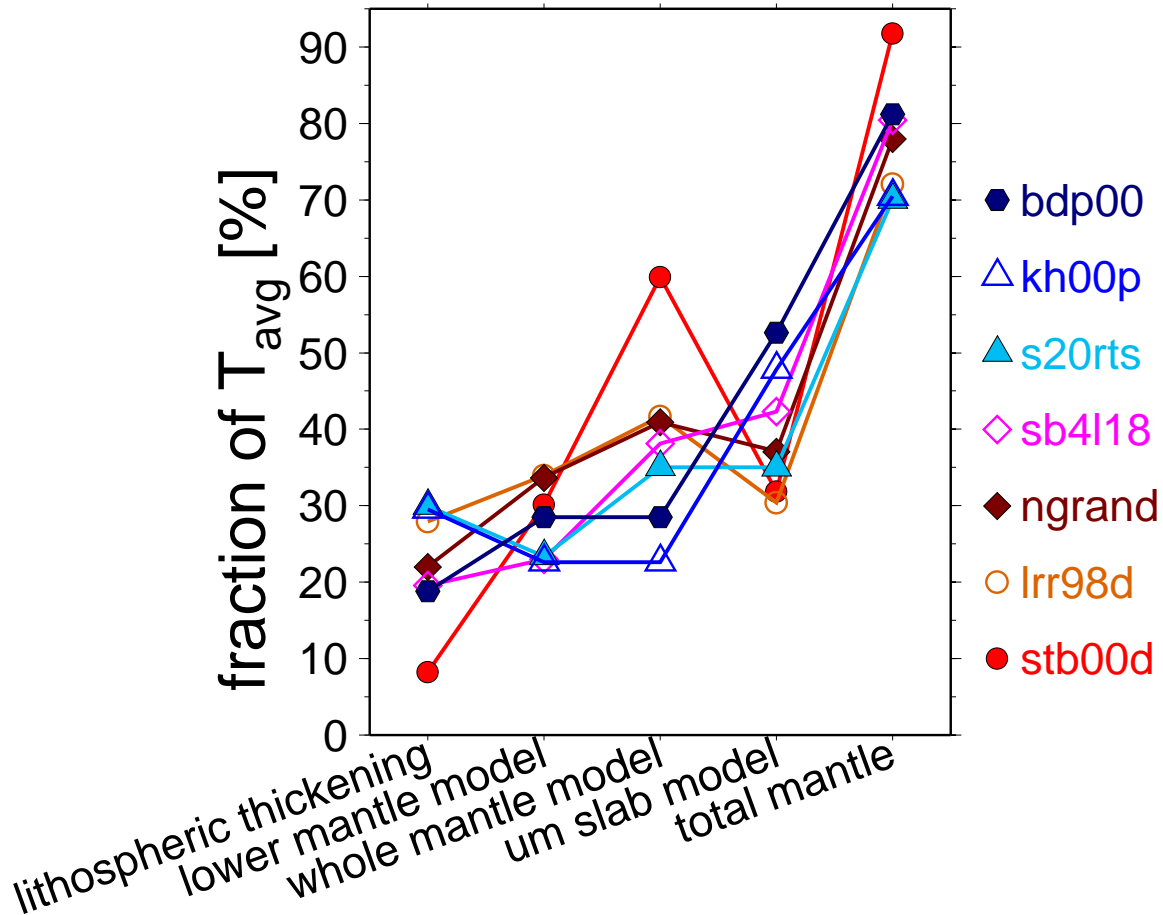
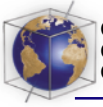


**Figure 19.** Fractional contribution of density models to the total driving torque,  $T_{\text{avg}}$ , for the optimized best-fit models with  $\eta_D$  as in Figure 16. The “um slab model” indicates the contribution of additional rum upper mantle slabs, not included in “whole mantle model”.

slightly improved to  $r_w \approx 0.83$ . These numbers are, however, lower than for models that include lower mantle based forces, considered in the next section.

#### 4.2.3. Mantle Structure

[50] We now turn to plate motion models that are based on lower and/or whole mantle density anomalies and include other driving forces successively. Results in Figure 16 are based on  $P$  and  $S$  wave tomography and subduction models stb00d and lrr98d. As above, we test

seismic (rum) and “total” (lrr98d) upper mantle slab configurations. For flow driven by mantle density structure only, we observe that  $P$  wave models do a poorer job than  $S$  wave models. Both are inferior to subduction models, such as stb00d, which yields  $r_w = 0.84$ . When we allow for lithospheric contributions, plate motion fits are improved, and the best model is again stb00d, although it is not substantially better than lrr98d or s20rts. Table A1 lists the performance parameters for the best mantle plus lithospheric thickening models with the corresponding optimized values for  $\eta_0$  and  $R_Q$ .

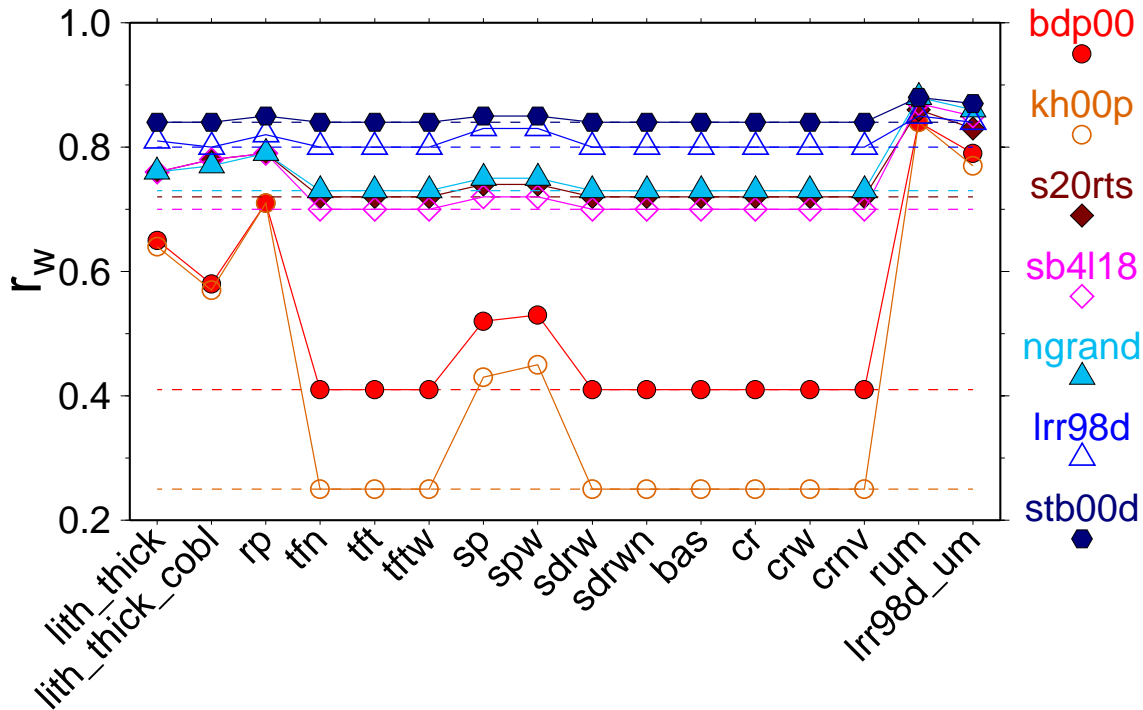
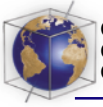


**Figure 20.** Effect of torque addition to mantle density only  $\eta_D$  models as in Figure 16. The  $r_w$  is shown for mantle only (dashed base lines) and additional torques (symbols and solid lines). For edge force legend, see Table 2.

[51] Focusing on the lithospheric structure models, we find that for  $\eta_D$ , the mean model performances of all model combinations,  $\bar{r}_w$ , are 0.80/0.83 for oceanic-only/global lithospheric contributions from our model and 0.79/0.75 for the *Coblentz et al.* [1994] torques. Consistent with our findings in section 4.2.2, we find that our lithospheric torques lead to slightly better predictions than *Coblentz et al.*'s [1994], and the inclusion of continental crustal structure has led to a small improvement of plate motion fits. However, as mentioned before, it is not clear if potential energy differences in old continental regions will contribute much to driving plates such that the relevance of this improvement is doubtful.

[52] We next test the effect of replacing all upper mantle structure with the seismic slab

model rum (Figure 16). This approach improves *P* wave models substantially and improves *S* wave models, stb00d, and lrr98d slightly. When we use slabs as derived from the upper mantle part of lrr98d instead, results are comparable. For other viscosities (markedly  $\eta_G$ ) we find that “total” slabs based on lrr98d lead to models that are slightly better than those for rum ( $\Delta r_w \sim 0.03$ ). (Scaling factors for the upper mantle part of lrr98d are then larger than those for the lower mantle, most likely since lrr98d has small density amplitude in the upper mantle.) We might therefore slightly underestimate the upper mantle slab driving force by restricting ourselves to the seismic rum. Since differences are not great, we nonetheless use only rum for upper mantle slabs in the following for simplicity.

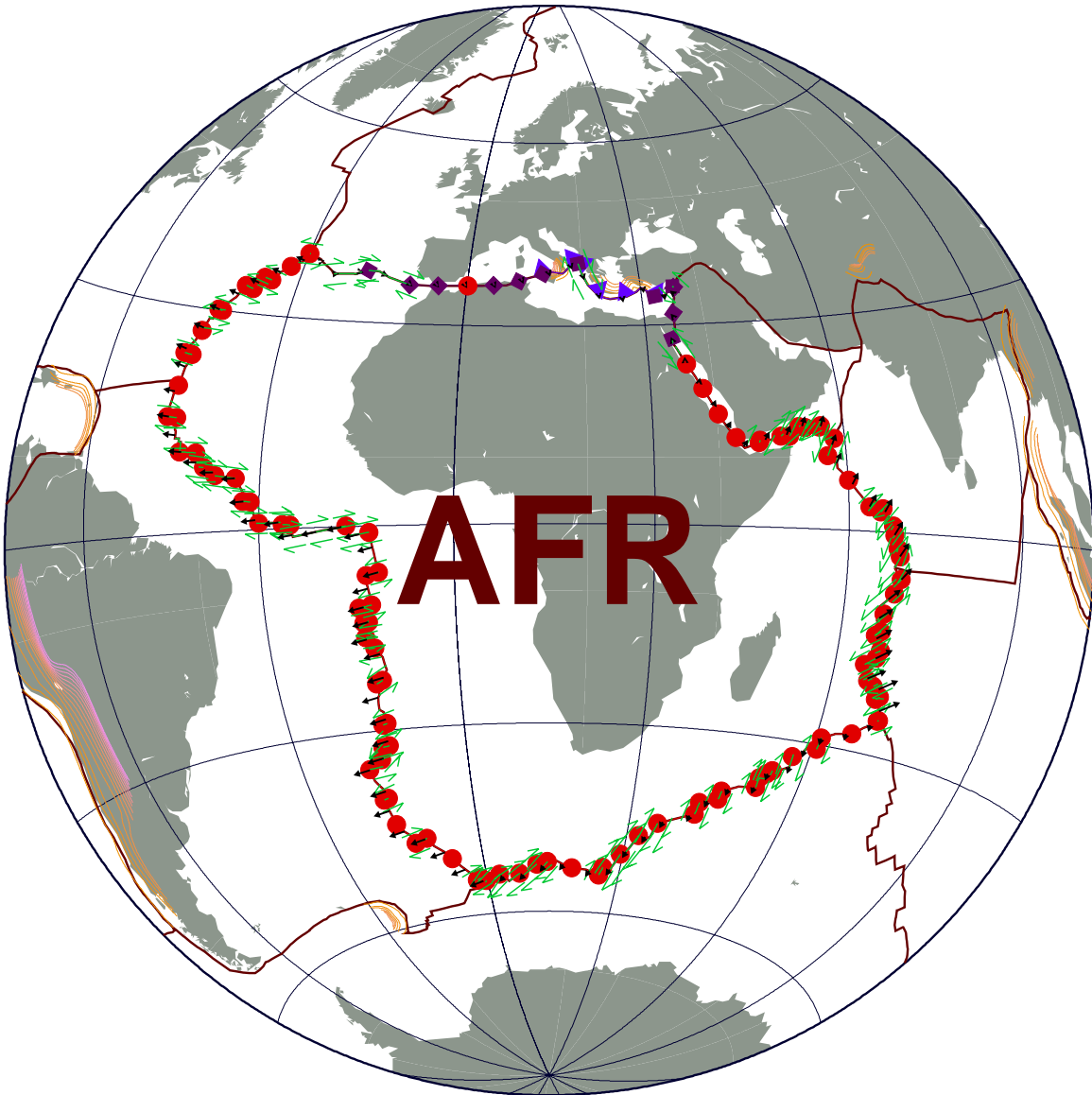
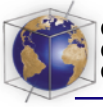


**Figure A1.** Plates and boundaries from NUVEL-1 as used in the velocity inversion and integration of edge forces, part 1. (a) AFR, Africa; (b) ANT, Antarctica; (c) ARA, Arabia; (d) AUS, Australia; CAR, Caribbean; COC, Cocos; EUR, Eurasia; IND, India; NAM, North America; NAZ, Nazca; PAC, Pacific; PHI, Philippines; and SAM, South America. Margin types are as follows: red circles, ridge; green slip-arrows, transform boundary; bright violet one-sided triangle, convergent margin with seismic slab; dark violet centered triangle, convergent margin without deep seismicity. Black vectors indicate relative motion of neighboring plates; contour lines indicate Wadati-Benioff zone geometry from RUM [Gudmundsson and Sambridge, 1998] (yellow, shallow; magenta, deep).

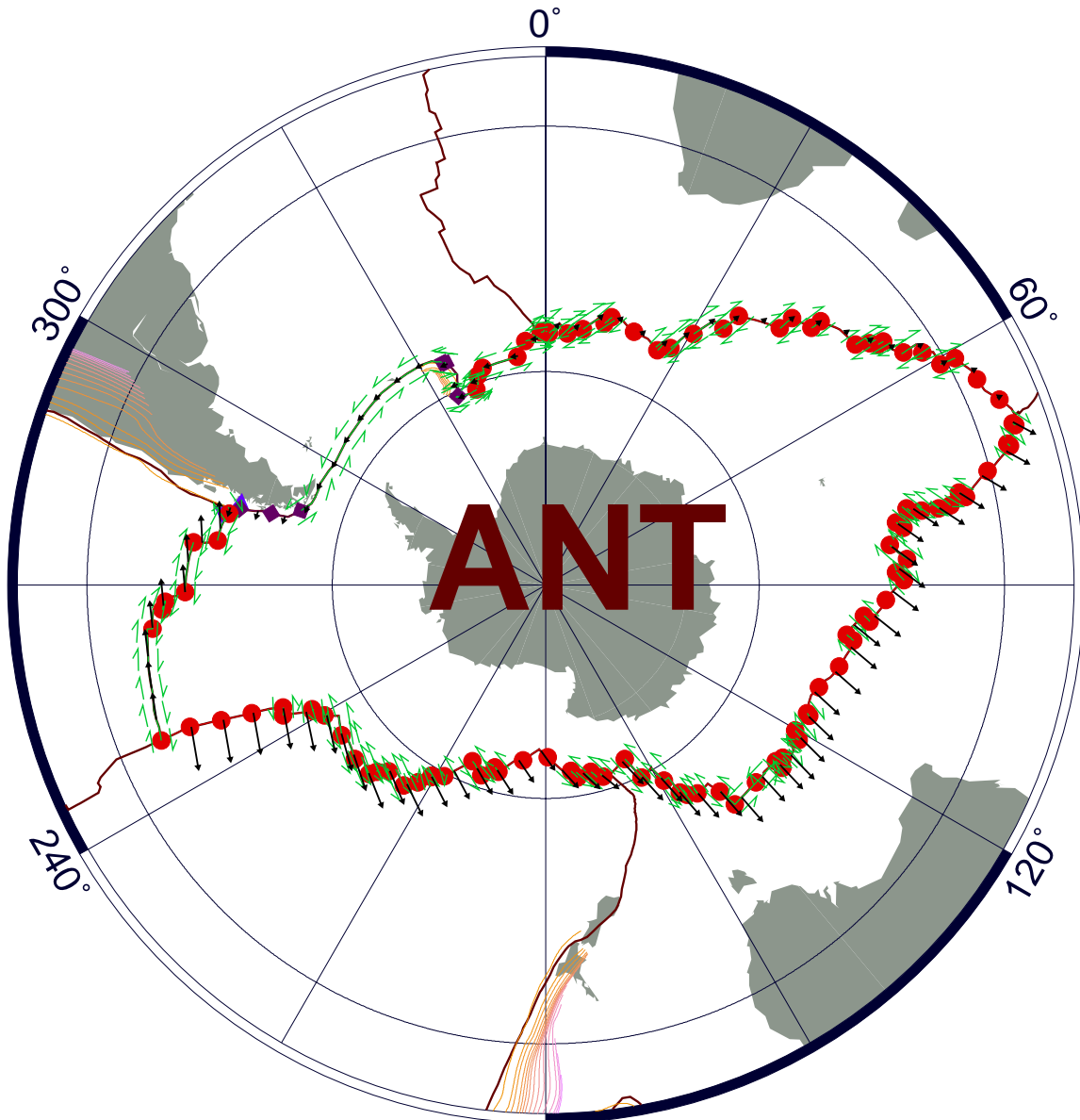
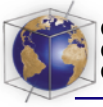


Figure A1. (continued)

[53] Finally, we search for the best models using whole or lower mantle only structure, lithospheric thickening due to seafloor spreading, and additional rum slabs (assuming that tomographic models fail to image some slab signal). With this combination, all types of models achieve  $r_w \approx 0.89$  ( $VR_w \approx 80\%$ ) and

none is significantly better than the other. (A list of best-fit models with the scaling parameters is given in Table A2.) For  $P$  wave models, the best-fit is achieved with lower mantle structure from tomography, replacing the upper mantle completely with rum. This is consistent with our previous finding that

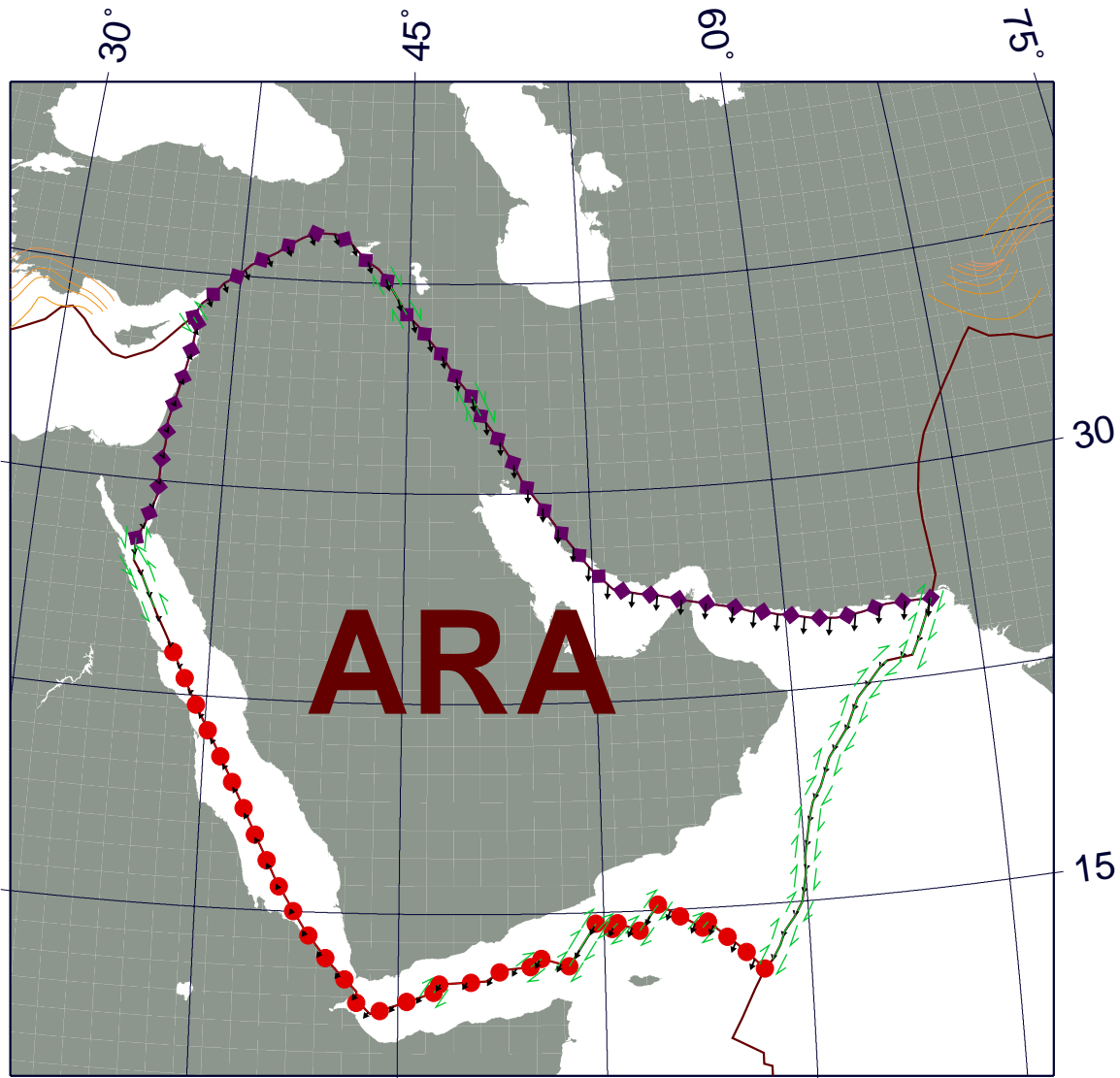
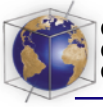


Figure A1. (continued)

the upper mantle structure imaged by *P* wave models is different from the slab signature that appears to be included in *S* wave models (see section 4.1). Accordingly, the best *S* wave model inversion uses the whole mantle structure and adds some rum signal to the upper mantle part. If we consider only the exact viscosity structures that have led to the geodynamic models lrr98d and stb00d for

consistency, the best models are slightly worse and  $r_w \approx 0.86$ .

[54] For illustration, we include the predicted plate velocities for the best fitting *s* wave model (Figure 17) and lrr98d (Figure 18). (For the best-fit velocities for stb00d and *P* model see Figures A7 and A8, respectively. Model scaling factors are given in Table

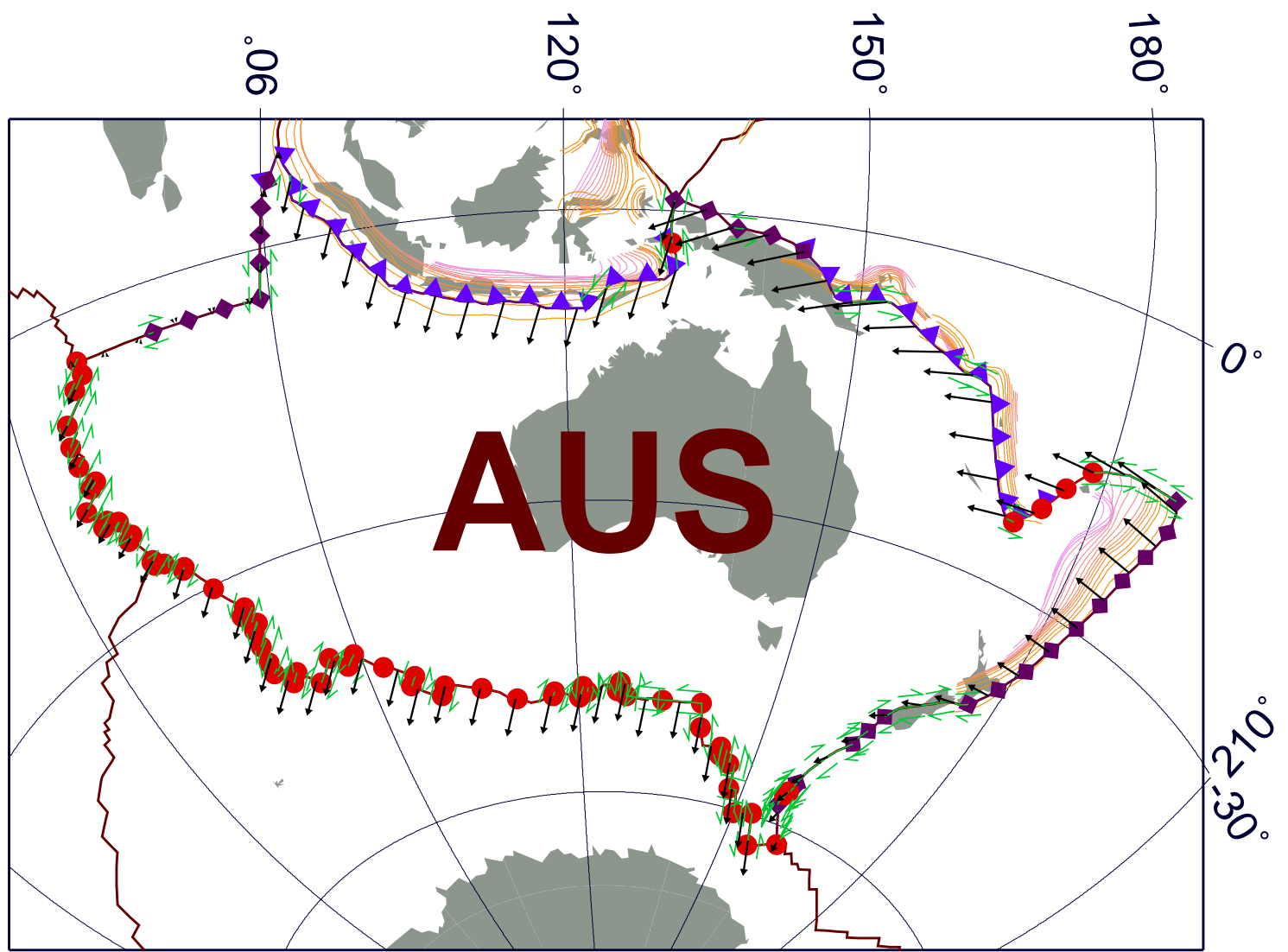
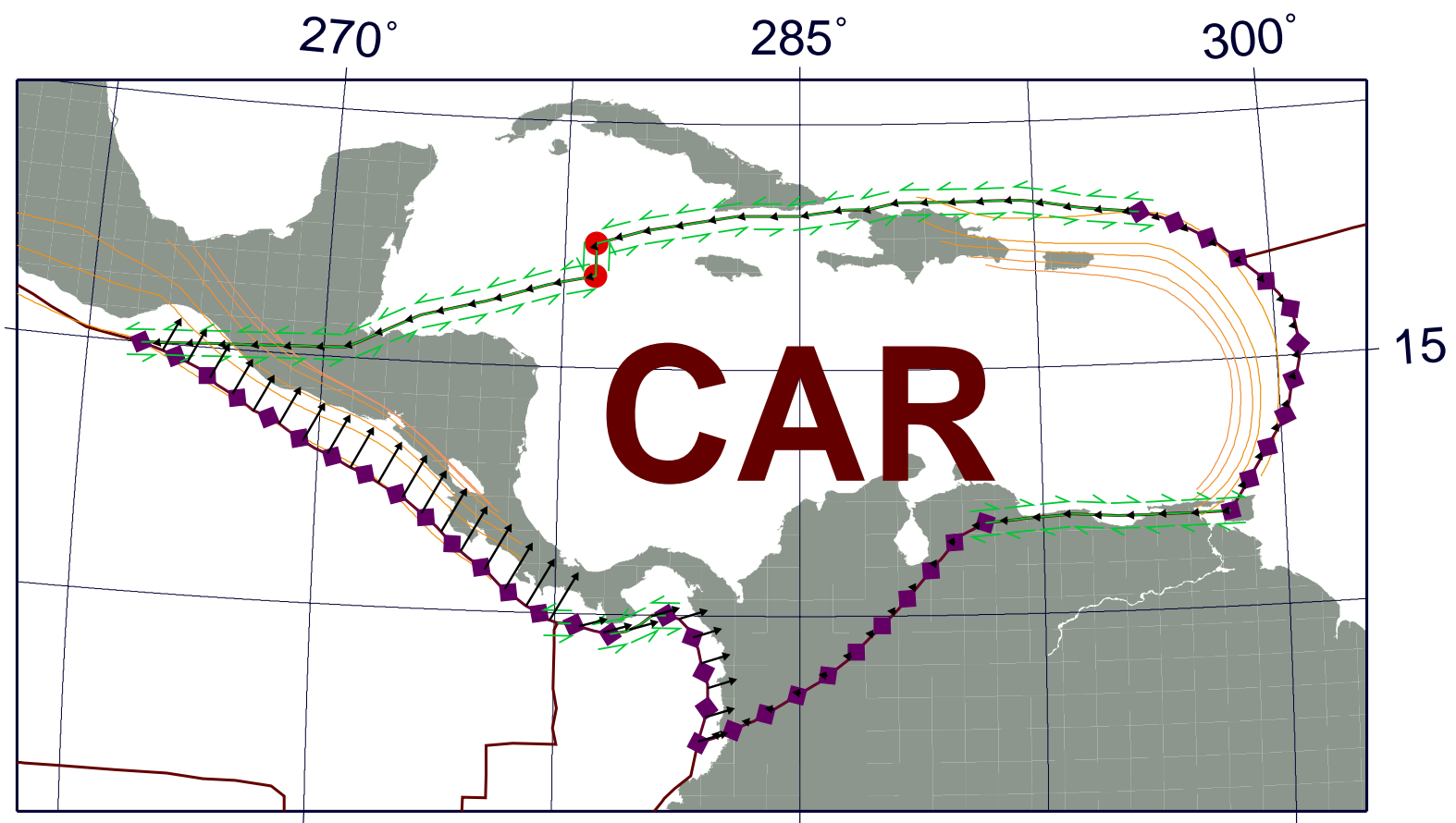


Figure A1. (continued)



**Figure A2.** Plate boundaries as used in the velocity inversion and the integration of plate boundary forces, part 2: (a) CAR, (b) COC, (c) EUR, (d) IND, (e) NAM, and (f) NAZ. For explanation see Figure A1.

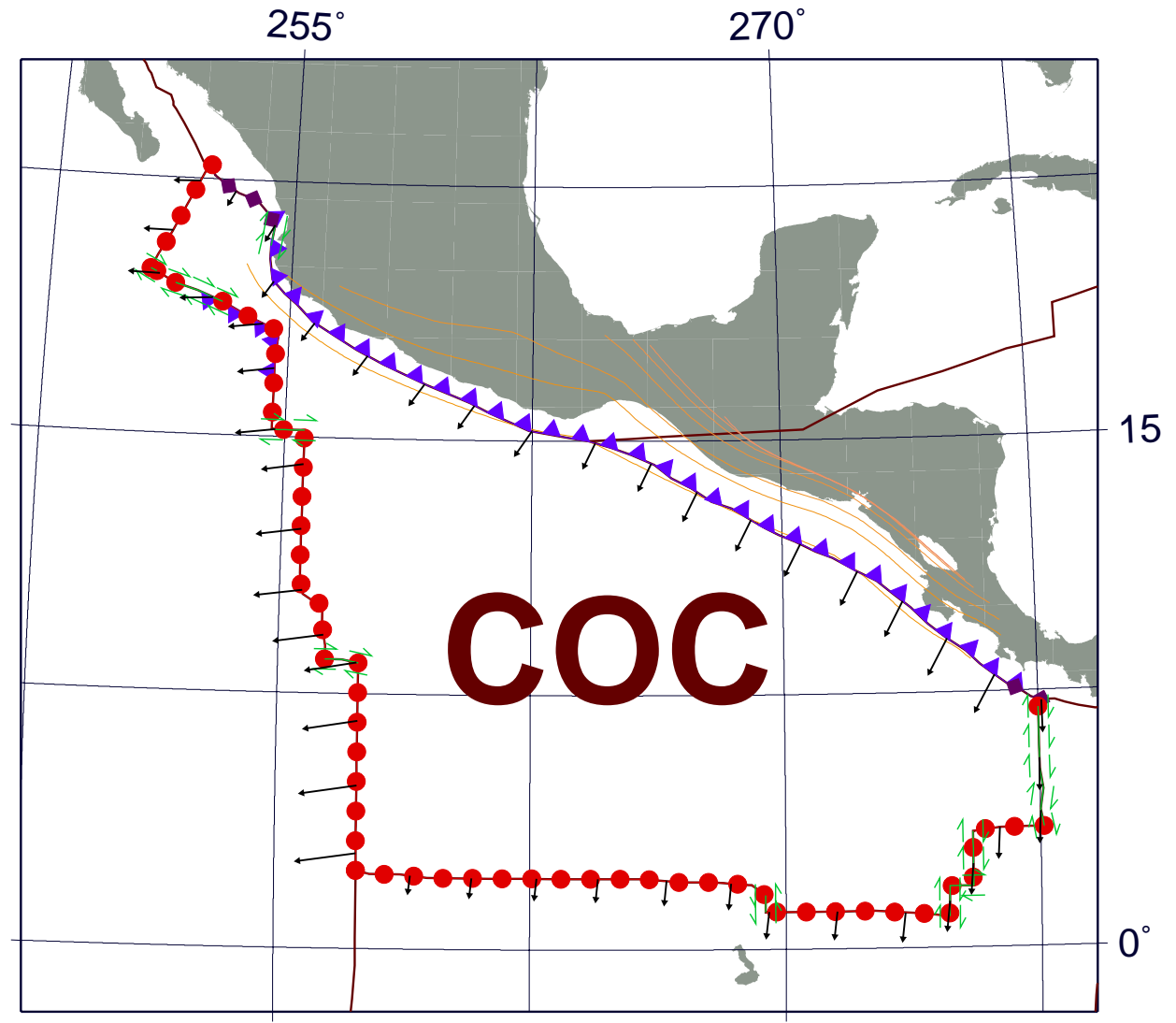


Figure A2. (continued)

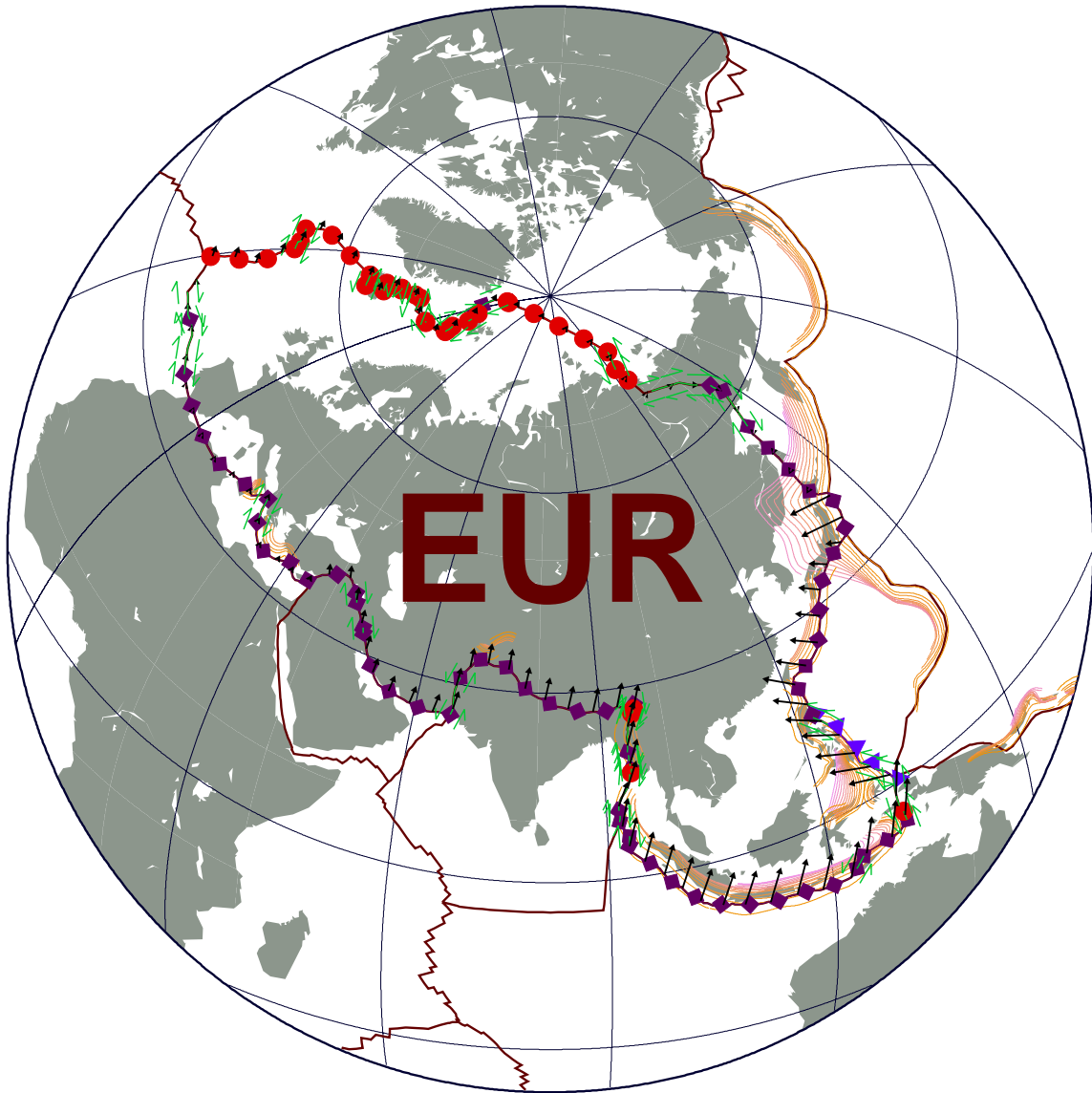
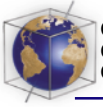


Figure A2. (continued)

A2.) Inspection of the plate velocities shows fairly good agreement between models and observations, as in earlier work. Discrepancies differ between models, with some consistent failures like the underprediction of the northward motion of SAM. The velocities we find for lrr98d are similar, but not identical, to those of *Lithgow-Bertelloni and Richards* [1995], and we attribute this to

small differences in the viscosity structure and the lithospheric model. Quality measures such as  $r_w$  ( $\sim 0.9$ ) are comparable, however.

[55] We conclude that a range of models, based on tomography or subduction history, can reproduce plate motions, indicating that the sinking slabs are the most important contribu-

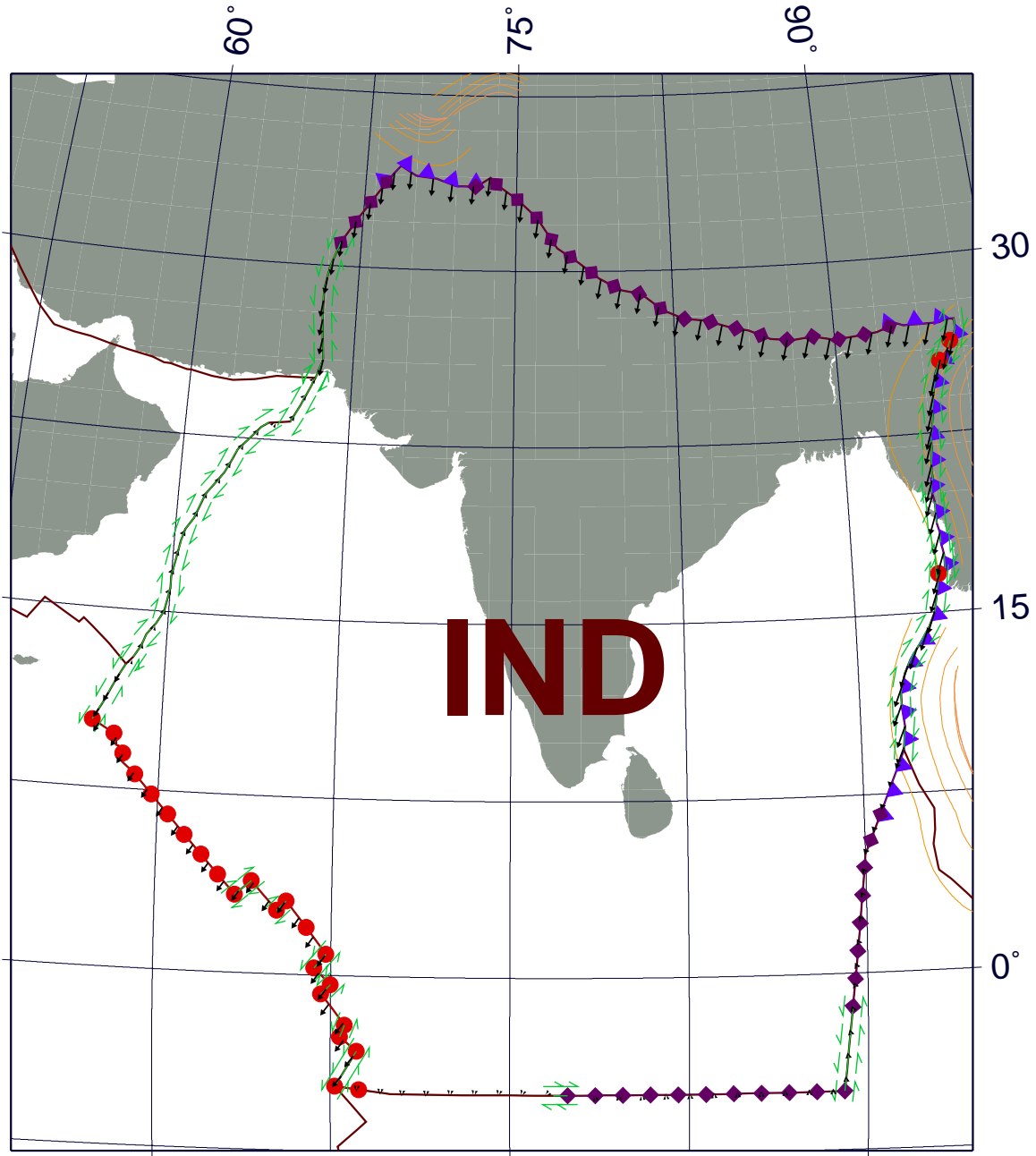
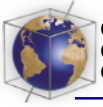


Figure A2. (continued)

tion to the mantle driving forces as far as tomography and our models can resolve them. All models that include lower mantle structure perform better than the upper mantle only

models of section 4.2.2. For some models and viscosity profiles, the difference is up to  $\Delta r_w \approx 0.1$ , which is statistically significant at the 95% level using Fisher's  $z$  transformation. This

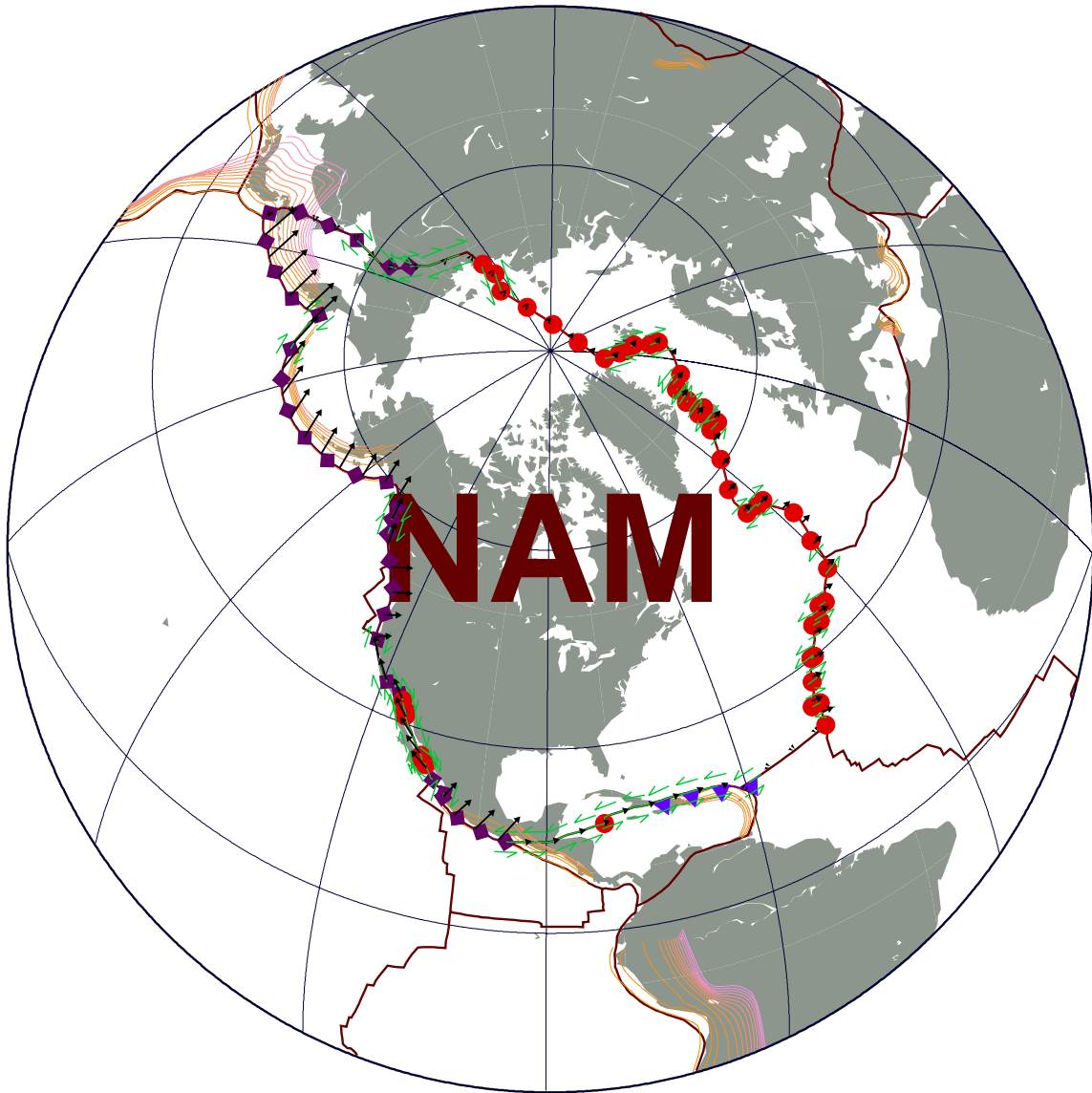
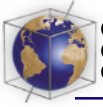


Figure A2. (continued)

improvement in fit when lower mantle sources are included is in agreement with the notion that slab related structures in the lower mantle are the most important features of mantle convection [e.g., Chase, 1979], that they correlate relatively well with fast regions of tomography [e.g., Ray and Anderson, 1994], and are responsible for major driving forces [e.g., Davies and Richards, 1992; Ricard *et al.*,

1993; Deparis *et al.*, 1995; Lithgow-Bertelloni and Richards, 1995].

[56] What differs between the best-fitting mantle models, however, are the relative contributions of the different components to the total torque,  $T_{\text{avg}}$ . Figure 19 shows that the contribution of the lithosphere for the best-fit models with  $\eta_D$  with optimized weight factors

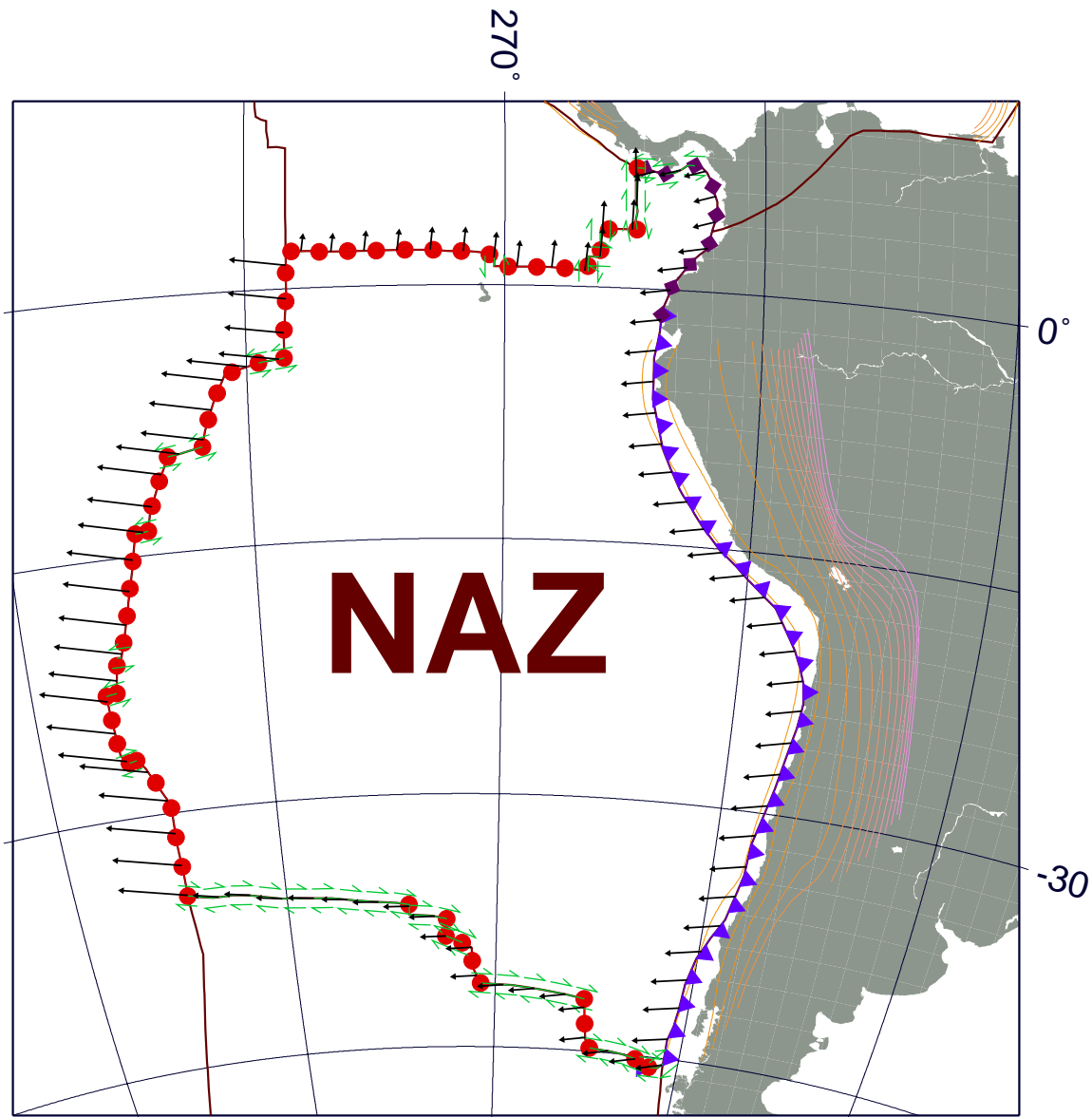
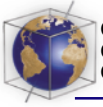
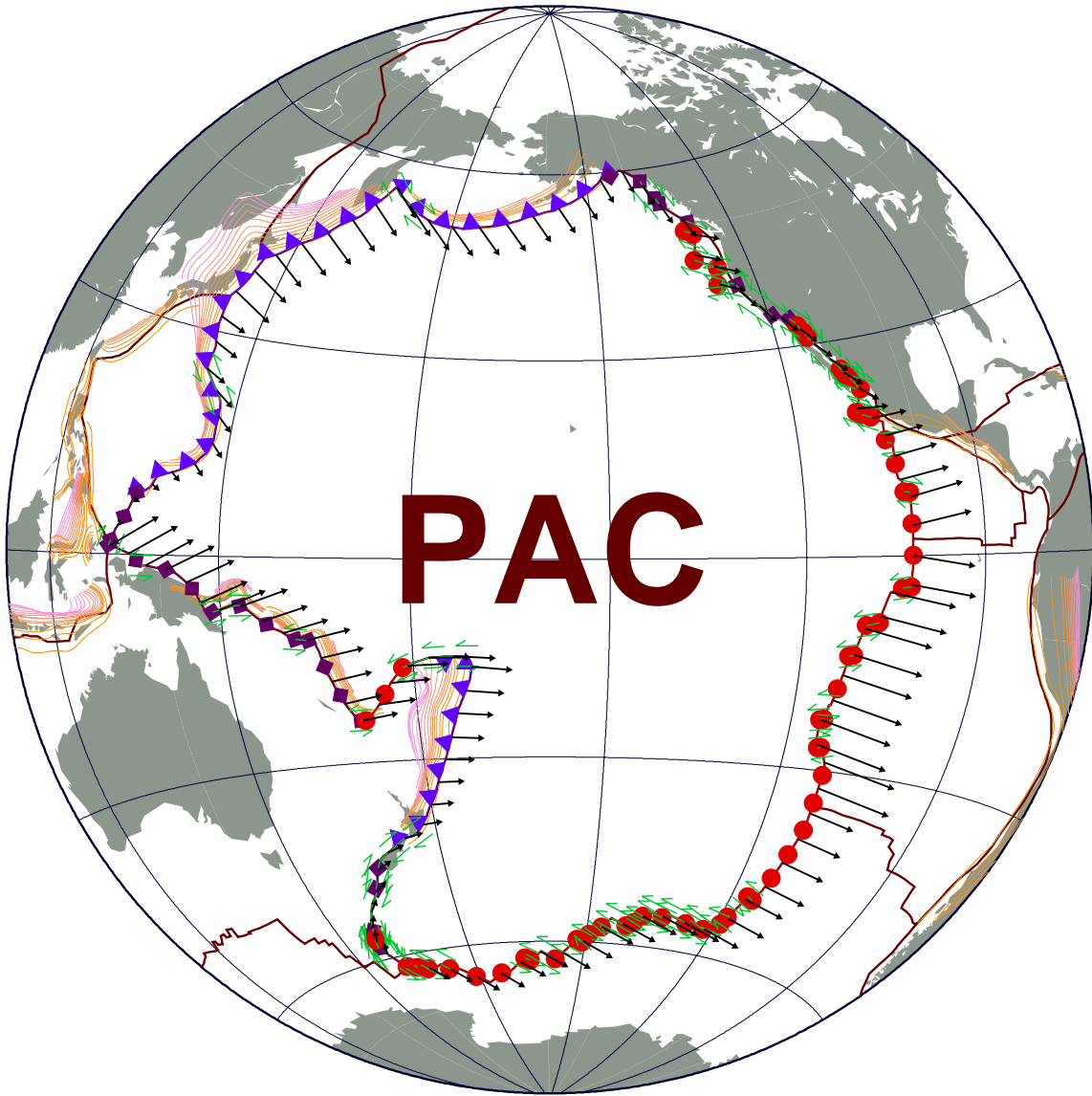
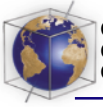


Figure A2. (continued)

varies between  $\sim 30\%$  for most models and  $\sim 10\%$  for *stb00d*. While all inversions include substantial additional rump slab pull, *lrr98d* does so to the smallest extent for  $\eta_D$  and rejects it completely for other viscosity structures such as  $\eta_G$ . We also observe that the fraction of the mantle driving force that comes from the lower mantle is between

$\sim 20\%$  and  $\sim 35\%$  for  $\eta_D$ . There is some variation of the individual contributions between viscosity profiles, and the lower mantle contribution can be as high as  $\sim 50\%$  for *lrr98d* and  $\eta_G$ .

[57] There is, of course, a priori information about the presence and, to some extent, the



**Figure A3.** Plates boundaries as used in the velocity inversion and the integration of plate boundary forces, part 3: (a) PAC, (b) PHI, and (c) SAM. For explanation see Figure A1.

amplitudes of the individual driving torques. Not all combinations of our optimized weights models correspond therefore to realistic absolute viscosity values and scaling factors. We have also seen that optimization gains are small since good velocity predictions can be found for a range of models and viscosity structures; the nonuniqueness of driving force inversions

is, in fact, one of our main conclusions. However, if we examine models where we fix the, probably best constrained, lithospheric thickening contribution and let only the absolute viscosity values vary, or if we fix all weights to their starting values, we find that results are similar to those shown above. Consistent with some models of *Lithgow-Bertelloni and*

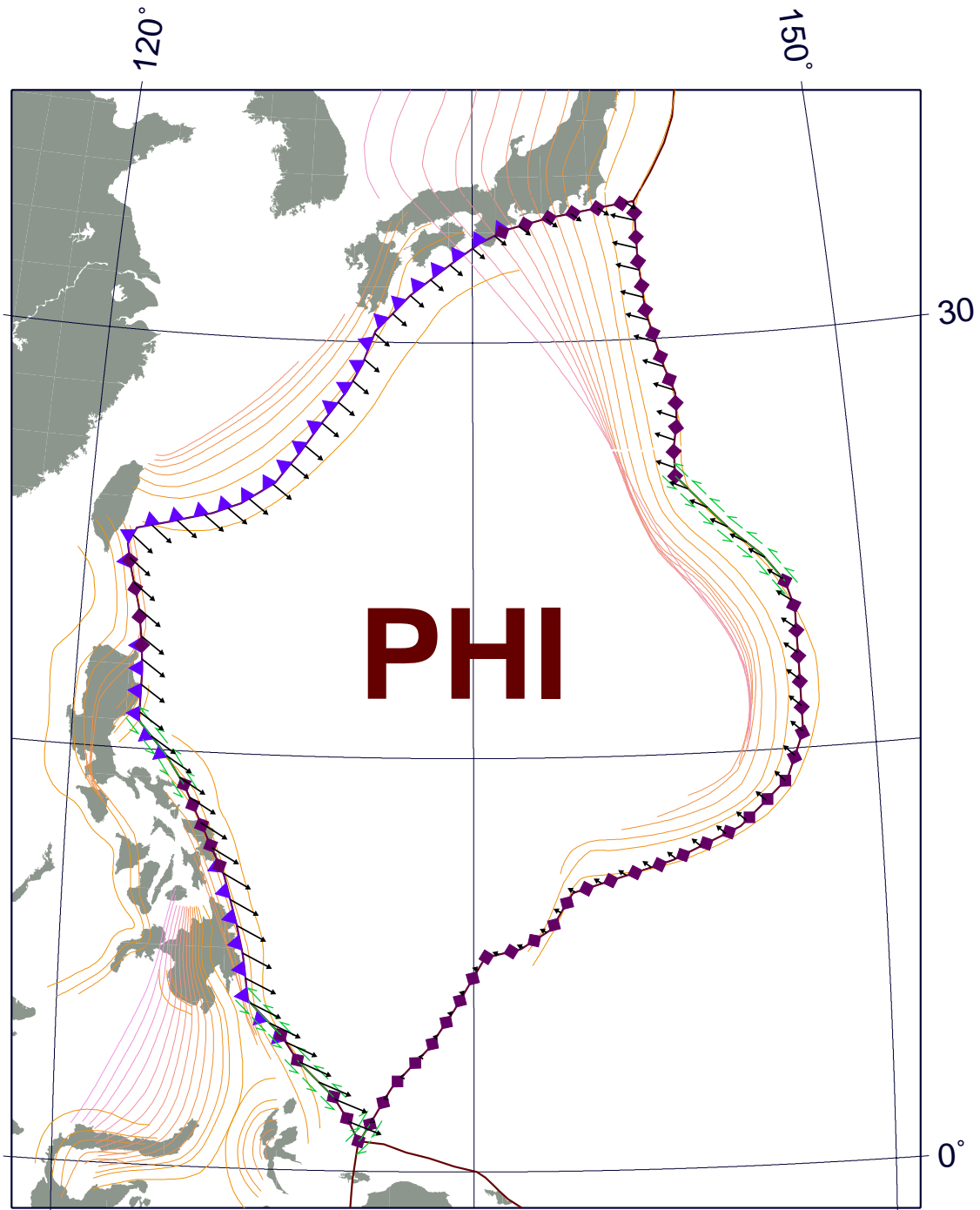
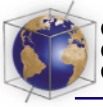


Figure A3. (continued)

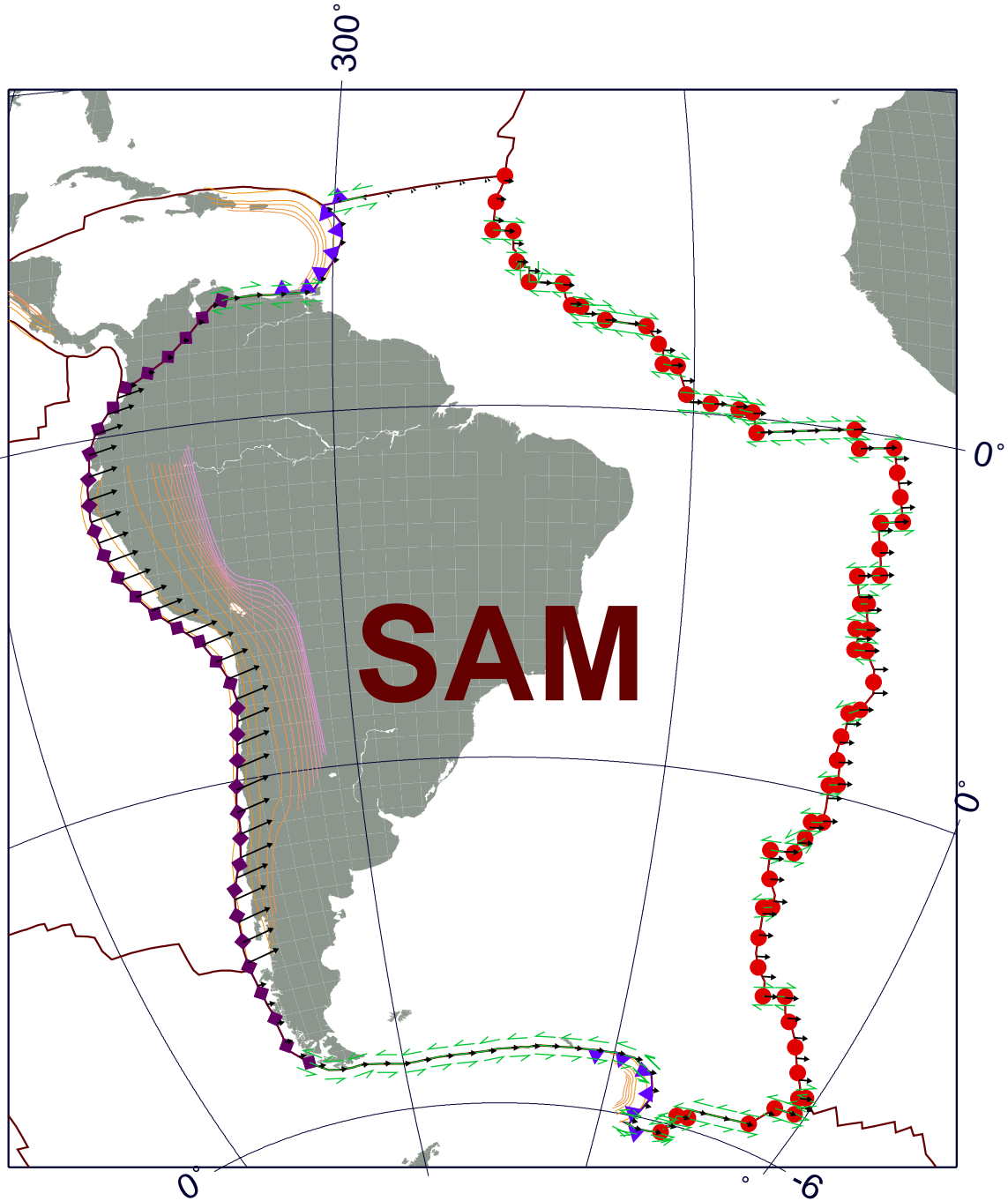
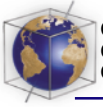
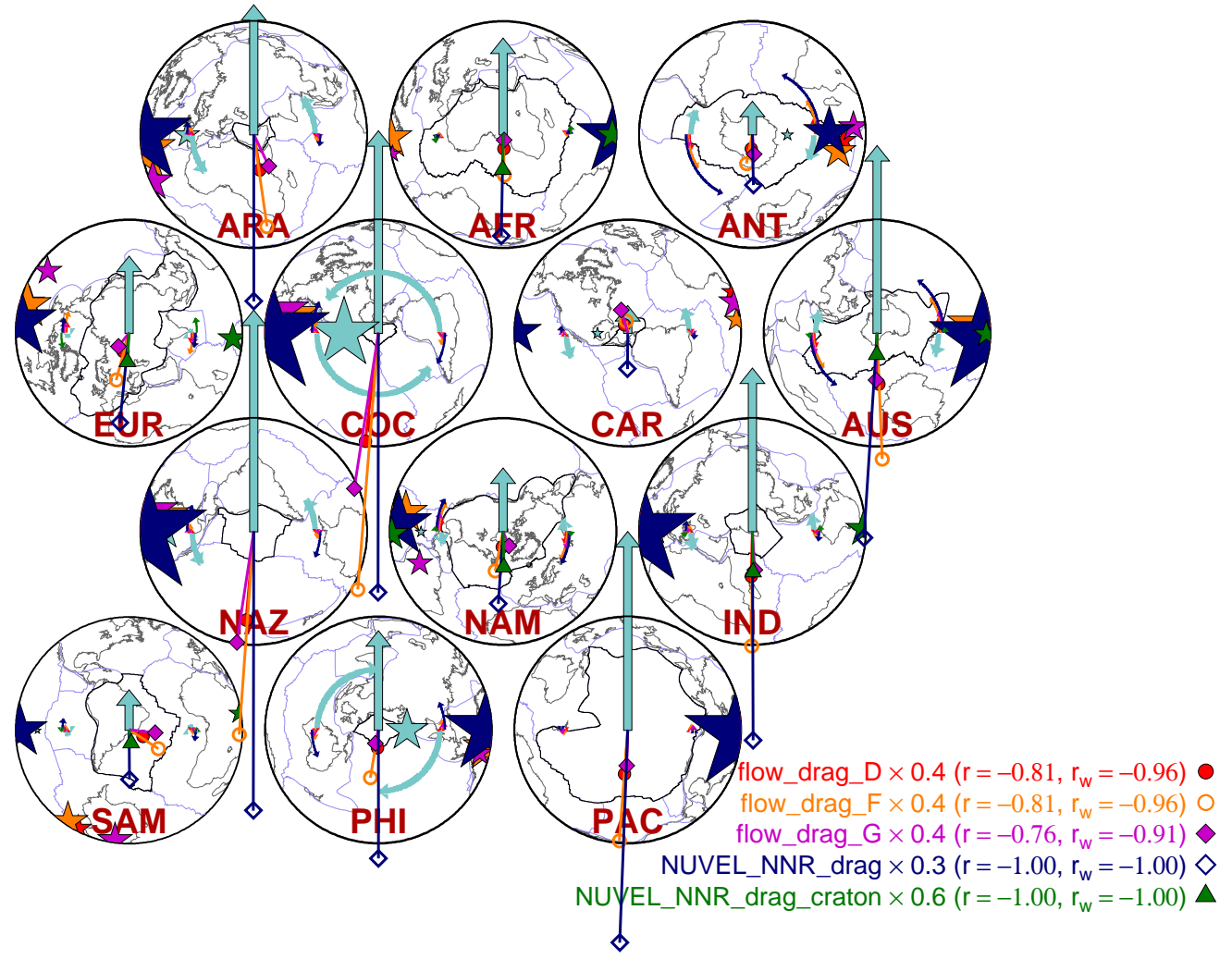


Figure A3. (continued)



**Figure A4.** Comparison of viscous drag torques. We show torques based on flow calculations with NUVEL-1 NNR surface motions prescribed and viscosity profiles  $\eta_D$ ,  $\eta_F$ , and  $\eta_G$ , as well as viscous drag torques that are based on tractions that are always opposite to the NNR plate motion. Also shown are torques based on such tractions but only underneath cratons (from the 3SMAC model by *Nataf and Ricard* [1996]). For explanation see Figure 4.

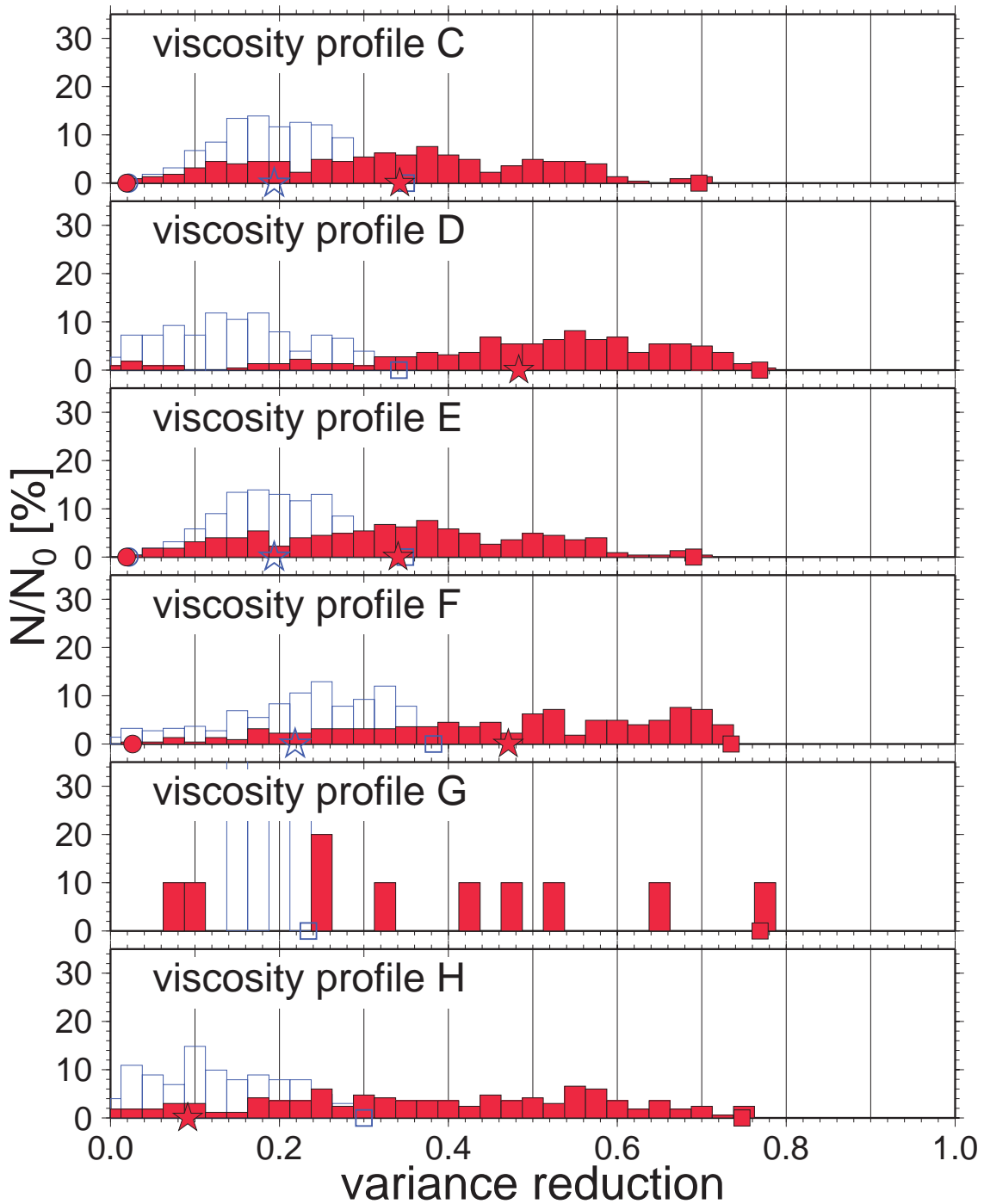
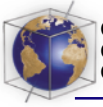
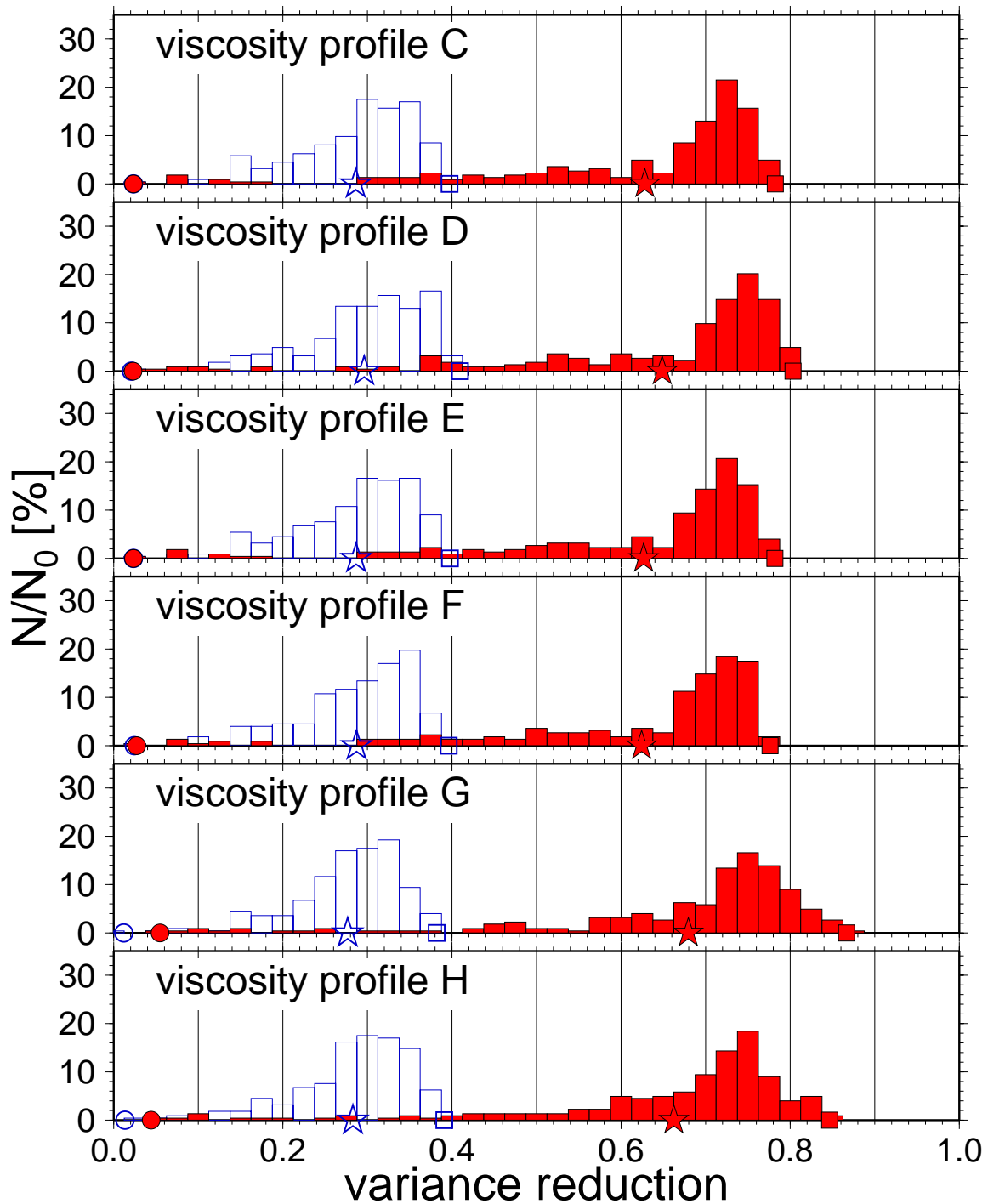
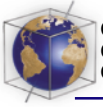
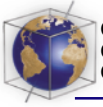


Figure A5. Histogram of nonoptimized model performance in terms of variance reduction.



**Figure A6.** Histogram of optimized model performance in terms of variance reduction. In contrast to Figure A5, all scaling factors were allowed to vary.



**$r = 0.58$   $r_w = 0.88$   $VR = 25.9\%$   $VR_w = 77.5\%$**

viscosity profile D

viscous drag  $w_1 = 0.78$

stb00d\_whole\_mantle\_D  $w_2 = 0.35$  (55%)

lith\_thick\_cobl  $w_3 = 0.24$  (12%)

rum\_slabs\_D  $w_4 = 0.46$  (32%)

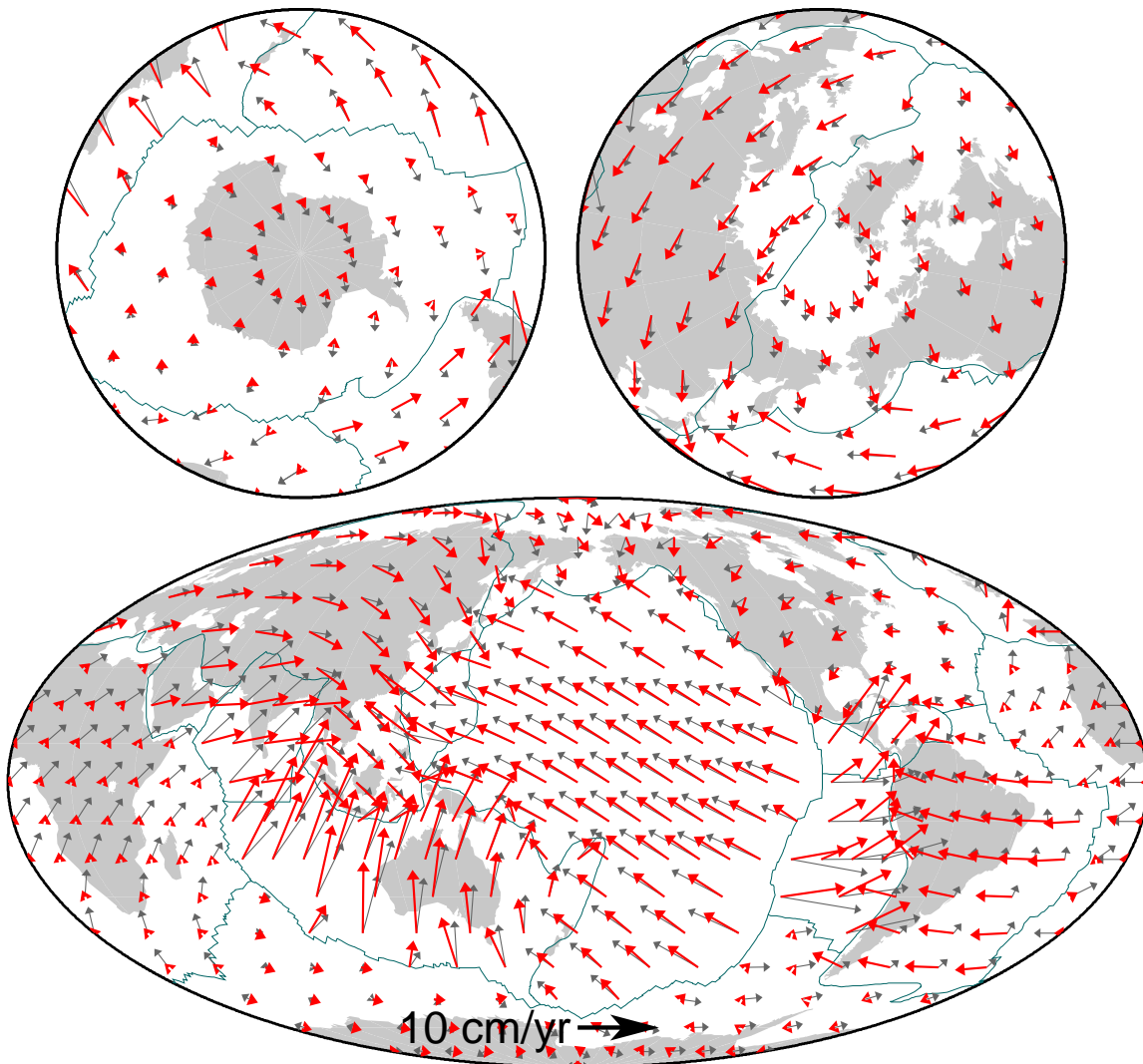
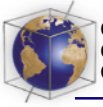


**Figure A7.** Predicted and observed plate motion based on the best fitting model using stb00d slabs and  $\eta_D$ , compare Figure 17.



**$r = 0.56$   $r_w = 0.88$   $VR = 18.1\%$   $VR_w = 78.3\%$**

viscosity profile D

viscous drag  $w_1 = 0.45$

bdp00\_lower\_mantle\_D  $w_2 = 0.69$  (31%)

lith\_thick\_cobl  $w_3 = 0.11$  (9%)

rum\_slabs\_D  $w_4 = 0.55$  (60%)

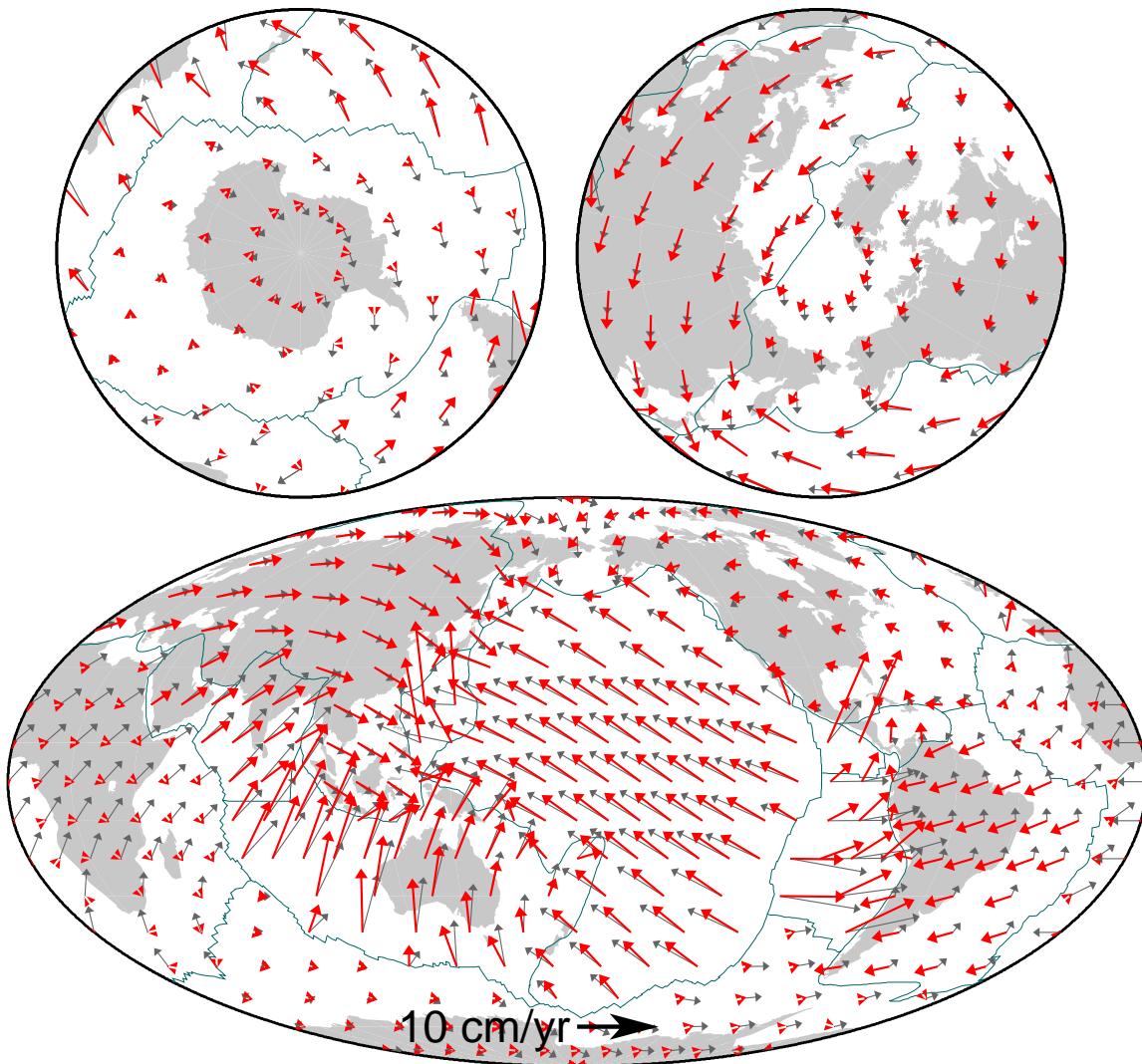


**Figure A8.** Predicted and observed plate motion based on the best fitting  $P$  wave model for  $\eta_D$ , bdp00, compare Figure 17.

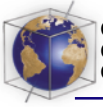


**Table A1.** Best Two Models for Mantle Density Plus Lithospheric Thickening Driving Torques<sup>a</sup>

Viscosity	Density Model	Type	$r_w$	VR <sub>w</sub>	$\eta_0, \sim 10^{21}$ Pas	$R_Q^{\text{tomo}}$
<i>Scaling Factors Fixed</i>						
C	stb00d	whole	0.83	54.7%	1	1
	sb4118	whole	0.75	42.1%	1	0.2
D	lrr98d	whole	0.84	70.2%	1	1
	s20rts	whole	0.83	68.5%	1	0.2
E	stb00d	whole	0.83	54.4%	1	1
	sb4118	whole	0.75	42.3%	1	0.2
F	stb00d	whole	0.83	68.5%	1	1
	sb4118	whole	0.77	56.8%	1	0.2
G	ngrand	whole	0.84	-79.0%	1	0.2
	bdp00	whole	0.60	-94.1%	1	0.4
H	ngrand	whole	0.81	65.4%	1	0.2
	lrr98d	whole	0.86	62.1%	1	1
<i>Scaling Factors Optimized</i>						
C	stb00d	whole	0.83	69.7%	0.32	0.53
	lrr98d	whole	0.83	68.1%	0.21	0.55
D	stb00d	whole	0.85	73.0%	1.55	1.05
	lrr98d	whole	0.84	71.0%	1.05	1.28
E	stb00d	whole	0.83	69.2%	0.32	0.52
	lrr98d	whole	0.82	67.8%	0.22	0.57
F	stb00d	whole	0.83	69.2%	0.68	0.71
	lrr98d	whole	0.82	67.2%	0.44	0.73
G	lrr98d	whole	0.89	79.5%	1.41	0.34
	s20rts	whole	0.88	76.8%	0.94	0.03
H	lrr98d	whole	0.88	76.8%	0.58	0.32
	stb00d	whole	0.87	75.8%	0.77	0.27

<sup>a</sup> Scaling factors are normalized such that the lithospheric contribution is assumed to be known ( $w_{\text{lith}} \equiv 1$ ), and for lrr98d and stb00d  $R_Q^{\text{tomo}} \neq 1$  indicates scaling of the density field.

**Table A2.** Best Two Models for Mantle Density, Lithospheric Thickening Torques From Ocean Age Progression, and rum Upper Mantle Slabs<sup>a</sup>

Viscosity	Density Model	Type	$r_w$	VR <sub>w</sub>	$\eta_0, 10^{21}$ Pas	$R_Q^{\text{tomo}}$	$R_Q^{\text{rum}}$
<i>Scaling Factors Fixed</i>							
C	stb00d	whole	0.87	68.9%	1	1	1
	sb4118	whole	0.84	60.4%	1	0.2	1
D	bdp00	lower	0.86	73.5%	1	0.4	1
	ngrand	whole	0.88	71.6%	1	0.2	1
E	stb00d	whole	0.87	68.2%	1	1	1
	sb4118	whole	0.84	59.9%	1	0.2	1
F	sb4118	whole	0.85	72.0%	1	0.2	1
	stb00d	whole	0.86	72.0%	1	1	1
G	bdp00	whole	0.83	-508.7%	1	0.4	1
	kh00p	whole	0.78	-528.2%	1	0.4	1
H	bdp00	lower	0.88	74.4%	1	0.4	1
	kh00p	lower	0.83	57.4%	1	0.4	1
<i>Scaling Factors Optimized</i>							
C	bdp00	lower	0.87	76.4%	0.99	1.42	3.90
	stb00d	whole	0.87	76.2%	0.62	0.69	1.24

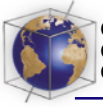


**Table A2.** (continued)

Viscosity	Density Model	Type	$r_w$	VR <sub>w</sub>	$\eta_0, 10^{21}$ Pas	$R_q^{\text{tomo}}$	$R_q^{\text{rum}}$
D	sb4118	whole	0.89	79.1%	1.78	0.14	1.41
	ngrand	whole	0.89	79.1%	2.40	0.51	1.93
E	bdp00	lower	0.87	75.9%	0.98	1.40	4.00
	ngrand	whole	0.87	75.9%	0.42	0.19	1.11
F	bdp00	lower	0.87	75.9%	2.19	1.98	5.03
	sb4118	whole	0.87	75.6%	0.74	0.09	1.09
G	stb00d	whole	0.90	81.7%	2.95	0.32	0.53
	bdp00	lower	0.90	81.1%	3.22	0.41	1.24
H	stb00d	whole	0.90	80.2%	1.41	0.39	0.54
	ngrand	whole	0.88	77.7%	0.95	0.10	0.50

<sup>a</sup> Scaling factors are normalized such that lithospheric sources are assumed to be known ( $w_{\text{lith}} \equiv 1$ ).  $R_q^{\text{tomo}} \neq 1$  or  $R_q^{\text{rum}} \neq 1$  implies scaling of the density field for lrr98d, stb00d, or rum. (Not all optimized weights correspond to realistic solutions.)

Richards [1995], we find that the total mantle density and lithospheric contribution to the driving torques is always  $\sim 70\%$  and  $\sim 30\%$ , respectively.

#### 4.2.4. Effect of Parameterized Edge Forces

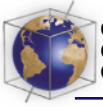
[58] We now evaluate the effects of edge forces on plate velocity inversions. First we show how plate motion models that are based on mantle density only and  $\eta_D$  can be improved by inclusion of additional torques (Figure 20). We find that the ridge push (rp) leads to larger improvements in fit than the realistic lithospheric models (“lith\_thick”) that consider the sea-floor age. The good performance of rp is related to the ridge-trench geometry, as discussed in section 3.5.

[59] Slab pull (sp/spw) leads to improvements for all models; they are nonetheless smaller than those resulting from the inclusion of rum or the upper mantle part of lrr98d. The viscous drag due to sinking slabs which acts on both plates at a convergent margin therefore appears to be more suited to driving the observed plate motions than a one-sided edge force which requires a stress guide and a strong slab. Except for the *P* models, weighting the slab pull by age (spw) does not consistently lead to larger improvement in  $r_w$  than sp for different mantle

models. All other edge forces lead to no significant increase in  $r_w$  if weights are restricted to  $w_i \geq 0$ .

[60] Finally, we explore how globally parameterized edge forces change models that already contain lower mantle, lithospheric, and rum density anomalies. We attempt to improve the model fit for  $\eta_D$  models while still enforcing  $w_i \geq 0$  and maximizing  $r_w$ . The inclusion of one additional edge force (equations (10)–(15)) improved the models by at most  $\Delta r_w = 0.02$  (cr for s20rts). However, introducing a colliding resistance typically led to an insignificant improvement of  $r_w$  or no improvement at all for other viscosities. Other edge forces, such as tft and tfn on transform faults, were rejected by the inversion and weighted as zero.

[61] If we allow for positive and negative weights, we find that models cannot be significantly improved either, only the relative strengths of different torques are readjusted to achieve optimal fits. The largest improvement for  $\eta_D$  is  $\Delta r_w = 0.03$  for an additional tftw that is weighted negatively and therefore corresponds to unphysical tangential transform fault driving forces. Results for the sign of other edge forces such as the collision resistance vary for different viscosity profiles,



and between models, implying that we cannot resolve them reliably.

[62] As expected from the correlation analysis of Figure 7, we find that a variety of forces can be combined to drive the plates. Since mantle, lithospheric, and upper mantle slab torques lead to models with good correlations of  $r_w \sim 0.9$  already, we cannot justify any added complexity due to globally parameterized edge forces. This implies either that our global parameterization has to be improved or that edge forces have to be specified according to more detailed regionalization for an enhanced prediction of plate motions. The treatment of forces, especially at convergent margins, might have to be improved to include the effect of lithospheric bending of the oceanic plate which could be important in determining the effectively transmitted forces between subducting and overriding plate [e.g., *Conrad and Hager, 1999; Becker et al., 1999*].

## 5. Conclusions

[63] We have demonstrated that a number of combinations of driving forces can be invoked to explain observed plate motions. Lithospheric thickening (or ridge push) and slab pull forces are successful candidates since they are naturally aligned with the correct direction of motion, from ridges to trenches. In section 4.2.2 we have shown that fairly good predictions of plate velocities are indeed possible without invoking any driving agents other than cooling lithosphere and upper mantle slabs.

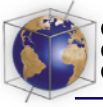
[64] However, if we include lower mantle density variations as derived from tomography or subduction models, the fit to observed plate motions always improves. This finding is insensitive to the viscosity structure with depth as long as there is radial flow through 660 km (section 4.2.1). Individual density models lead to slightly different predictions; yet all achieve

the same quality of fit with correlations of  $\sim 0.9$  (section 4.2.3). Models based on  $S$  wave tomography lead to equally good results as do models with only sinking slabs or  $P$  wave tomography. However, for the latter, we had to replace the upper mantle density variations with a slab model, probably because the ray path coverage of  $P$  models does not adequately image slabs.

[65] Our conclusion that the slab signal, as imaged by tomography and predicted by geodynamic models, is the most important contribution of mantle-driven torques substantiates earlier studies. Estimates of the relative importance of mantle or lithosphere based density variations are somewhat different for our best-fit models, but lithospheric thickening usually contributes  $\sim 30\%$ , and total mantle density anomalies contribute  $\sim 70\%$  to the average plate-driving torque. Of the latter component, roughly 40% is due to lower mantle heterogeneities. The lower mantle should therefore be explicitly taken into account when surface expressions of mantle convection are studied; it might be an oversimplification to neglect tractions caused by mantle flow in studies of intracontinental deformation.

[66] We were only marginally successful in our attempt to improve plate motion models by including parameterized plate boundary forces. We showed that one reason for this is that most edge forces can be classified as globally driving or resisting plate motions in a well correlated manner for simple geometrical reasons (section 3.5). Consequently, without independent knowledge of their magnitude, not much new information is introduced when edge force derived torques are used, and the improvement in fit does not warrant the additional complexity.

[67] Subduction zones in particular might require a more realistic treatment than was possible with our model. Our inversions did



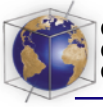
not, however, indicate that a colliding resistance was required, either on the subducting, or on both the subducting or overriding plate. A two-sided slab pull was found to be best suited to explain plate motions. These results imply that only a more detailed, regional specification of trench forces can be expected to improve plate motion models.

## Acknowledgments

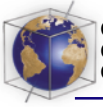
[68] We thank all authors of the tomographic and geodynamic models for sharing their results. Comments by our reviewers Carolina Lithgow-Bertelloni and Brad Hager, as well as suggestions by James Kellogg, Bernhard Steinberger, and Steven Zatzman, improved this typescript substantially. We also thank Bernhard for providing his flow code. Most figures were prepared with GMT [Wessel and Smith, 1995]. TWB was supported by the *Deutscher Akademischer Austauschdienst* (DAAD) under a “Doktorandenstipendium HSP–III,” and we would also like to acknowledge support from NSF grants EAR-9814666 and EAR-0001046.

## References

- Antolik, M., Ekström, G., Dziewonski, A. M., Gu, Y. J., Pan, J.-f., and Boschi, L., A new global joint  $P$  and  $s$  velocity model of the mantle parameterized in cubic B-splines, in *22nd Annual DoD/DOE Seismic Research Symposium: Planning for Verification of and Compliance with the Comprehensive Nuclear-Test-Ban Treaty (CTBT): Proceedings*, vol. II, Dep. of Defense, Washington, D.C., 2001.
- Artyushkov, E. V., Stresses in the lithosphere caused by crustal thickness inhomogeneities, *J. Geophys. Res.*, **78**, 7675–7708, 1973.
- Backus, G., J. Park, and D. Garbasz, On the relative importance of the driving forces of plate motion, *Geophys. J. R. Astron. Soc.*, **67**, 415–435, 1981.
- Bai, W., C. Vigny, Y. Ricard, and C. Froidevaux, On the origin of deviatoric stresses in the lithosphere, *J. Geophys. Res.*, **97**, 11,729–11,737, 1992.
- Becker, T. W., and L. Boschi, A comparison of tomographic and geodynamic mantle models, *Geochemistry, Geophysics, Geosystems*, in press, 2001.
- Becker, T. W., C. Facenna, R. J. O'Connell, and D. Giardini, The development of slabs in the upper mantle: Insight from numerical and laboratory experiments, *J. Geophys. Res.*, **104**, 15,207–15,225, 1999.
- Bokelmann, G., and E. Humphreys, Plate-mantle interaction and forces that move plates, *Eos Trans. AGU*, **81**(46), Fall Meet. Suppl., F12, 2000.
- Boschi, L., and A. M. Dziewonski, “High” and “low” resolution images of the Earth's mantle: Implications of different approaches to tomographic modeling, *J. Geophys. Res.*, **104**, 25,567–25,594, 1999.
- Carlson, R. L., and H. P. Johnson, On modeling the thermal evolution of the oceanic upper-mantle: An assessment of the cooling plate model, *J. Geophys. Res.*, **99**, 3201–3214, 1994.
- Chapple, W. M., and T. E. Tullis, Evaluation of the forces that drive the plates, *J. Geophys. Res.*, **82**, 1967–1984, 1977.
- Chase, C. G., Subduction, the geoid, and lower mantle convection, *Nature*, **282**, 464–468, 1979.
- Coblentz, D. D., R. M. Richardson, and M. Sandiford, On the gravitational potential of the Earth's lithosphere, *Tectonics*, **13**, 929–945, 1994.
- Conrad, C. P., and B. H. Hager, The effects of plate bending and fault strength at subduction zones on plate dynamics, *J. Geophys. Res.*, **104**, 17,551–17,571, 1999.
- Davies, G. F., and M. A. Richards, Mantle convection, *J. Geol.*, **100**, 151–206, 1992.
- DeMets, C., R. G. Gordon, D. F. Argus, and S. Stein, Current plate motions, *Geophys. J. Int.*, **101**, 425–478, 1990.
- Deparis, V., H. Legros, and Y. Ricard, Mass anomalies due to subducted slabs and simulations of plate motion since 200 My, *Earth Planet. Sci. Lett.*, **89**, 271–280, 1995.
- Elsasser, W. M., Convection and stress propagation in the upper mantle, in *The Application of Modern Physics to the Earth and Planetary Interiors*, edited by S. K. Runcom, pp. 223–249, John Wiley, New York, 1969.
- Engdahl, E. R., R. D. van der Hilst, and R. Buland, Global teleseismic earthquake relocation with improved travel times and procedures for depth determination, *Bull. Seismol. Soc. Am.*, **88**, 722–743, 1998.
- Fleitout, L., and C. Froidevaux, Tectonics and topography for a lithosphere containing density heterogeneities, *Tectonics*, **1**, 21–56, 1982.
- Fleitout, L., and C. Froidevaux, Tectonic stresses in the lithosphere, *Tectonics*, **2**, 315–324, 1983.
- Forsyth, D., and S. Uyeda, On the relative importance of the driving forces of plate motion, *Geophys. J. R. Astron. Soc.*, **43**, 163–200, 1975.
- Forte, A. M., and W. R. Peltier, Plate tectonics and aspherical Earth structure: The importance of poloidal-toroidal coupling, *J. Geophys. Res.*, **92**, 3645–3679, 1987.
- Forte, A. M., W. R. Peltier, and A. M. Dziewonski, In-



- ferences of mantle viscosity from tectonic plate velocities, *Geophys. Res. Lett.*, *18*, 1747–1750, 1991.
- Forte, A. M., A. M. Dziewonski, and R. J. O'Connell, Continent–Ocean chemical heterogeneity in the mantle based on seismic tomography, *Science*, *268*, 386–388, 1995.
- Gable, C. W., *Numerical Models of Plate Tectonics and Mantle Convection in Three Dimensions*, Ph.D. thesis, Harvard University, Cambridge MA, 1989.
- Gable, C. W., R. J. O'Connell, and B. J. Travis, Convection in three dimensions with surface plates: Generation of toroidal flow, *J. Geophys. Res.*, *96*, 8391–8405, 1991.
- Gordon, R. G., A. Cox, and C. E. Harter, Absolute motion of an individual plate estimated from its ridge and trench boundaries, *Nature*, *274*, 752–755, 1978.
- Gordon, R. G., and D. M. Jurdy, Cenozoic global plate motions, *J. Geophys. Res.*, *91*, 12,389–12,406, 1986.
- Grand, S. P., Mantle shear structure beneath the Americas and surrounding oceans, *J. Geophys. Res.*, *99*, 11,591–11,621, 1994.
- Grand, S. P., R. D. van der Hilst, and S. Widiyantoro, Global seismic tomography; A snapshot of convection in the Earth, *GSA Today*, *7*, 1–7, 1997.
- Gudmundsson, O., and M. Sambridge, A regionalized upper mantle (RUM) seismic model, *J. Geophys. Res.*, *103*, 7121–7136, 1998.
- Hager, B. H., Oceanic plate motions driven by lithospheric thickening and subducted slabs, *Nature*, *276*, 156–159, 1978.
- Hager, B. H., Subducted slabs and the geoid: Constraints on mantle rheology and flow, *J. Geophys. Res.*, *89*, 6003–6015, 1984.
- Hager, B. H., and R. W. Clayton, Constraints on the structure of mantle convection using seismic observations, flow models, and the geoid, in *Mantle Convection; Plate Tectonics and Global Dynamics*, vol. 4 *The Fluid Mechanics of Astrophysics and Geophysics*, edited by W. R. Peltier, pp. 657–763, Gordon and Breach, Newark, N. J., 1989.
- Hager, B. H., and R. J. O'Connell, Kinematic models of large-scale flow in the Earth's mantle, *J. Geophys. Res.*, *84*, 1031–1048, 1979.
- Hager, B. H., and R. J. O'Connell, A simple global model of plate dynamics and mantle convection, *J. Geophys. Res.*, *86*, 4843–4867, 1981.
- Hager, B. H., R. W. Clayton, M. A. Richards, R. P. Comer, and A. M. Dziewonski, Lower mantle heterogeneity, dynamic topography and the geoid, *Nature*, *313*, 541–545, 1985.
- Hales, A. L., Gravitational sliding and continental drift, *Earth Planet. Sci. Lett.*, *6*, 31–34, 1969.
- Harper, J. F., On the driving forces of plate tectonics, *Geophys. J. R. Astron. Soc.*, *40*, 465–474, 1975.
- Isacks, B. L., J. Oliver, and L. R. Sykes, Seismology and the new global tectonics, *J. Geophys. Res.*, *73*, 5855–5899, 1968.
- Ishii, M., and J. Tromp, Even-degree lateral variations in the earth's mantle constrained by free oscillations and the free-air gravity anomaly, *Geophys. J. Int.*, *145*, 77–96, 2001.
- Jordan, T. H., Composition and development of the continental tectosphere, *Nature*, *274*, 544–548, 1978.
- Kárason, H., and R. D. van der Hilst, Tomographic imaging of the lowermost mantle with differential times of refracted and diffracted core phases (PKP, Pdiff), *J. Geophys. Res.*, *106*, 6569–6588, 2001.
- Karato, S.-I., Importance of anelasticity in the interpretation of seismic tomography, *Geophys. Res. Lett.*, *20*, 1623–1626, 1993.
- Karpychev, M., and L. Fleitout, Simple considerations on forces driving plate motion and on the plate-tectonic contribution to the long-wavelength geoid, *Geophys. J. Int.*, *127*, 268–282, 1996.
- King, S. D., C. W. Gable, and S. A. Weinstein, Models of convection-driven tectonic plates: A comparison of methods and results, *Geophys. J. Int.*, *109*, 481–487, 1992.
- Lister, C. R. B., Gravitational drive on oceanic plates caused by thermal contraction, *Nature*, *257*, 663–665, 1975.
- Lithgow-Bertelloni, C., and M. A. Richards, Cenozoic plate driving forces, *Geophys. Res. Lett.*, *22*, 1317–1320, 1995.
- Lithgow-Bertelloni, C., and M. A. Richards, The dynamics of Cenozoic and Mesozoic plate motions, *Rev. of Geophys.*, *36*, 27–78, 1998.
- Lliboutry, L. A., Sea floor spreading, continental drift and lithosphere sinking with an asthenosphere at melting point, *J. Geophys. Res.*, *74*, 6525–6540, 1969.
- Masters, G., H. Bolton, and G. Laske, Joint seismic tomography for p and s velocities: How pervasive are chemical anomalies in the mantle?, *Eos Trans. AGU*, *80*(17), Spring Meet. Suppl., S14, 1999.
- Masters, G., G. Laske, H. Bolton, and A. M. Dziewonski, The relative behavior of shear velocity, bulk sound speed, and compressional velocity in the mantle: Implications for chemical and thermal structure, in *Earth's Deep Interior: Mineral Physics and Tomography From the Atomic to the Global Scale*, *Geophysical Monograph*, vol. 117, edited by S.-I. Karato, A. M. Forte, R. C. Liebermann, G. Masters, and L. Stixrude, pp. 63–87, AGU, Washington, D.C., 2000.
- McKenzie, D. P., Some remarks on heat flow and gravity anomalies, *J. Geophys. Res.*, *72*, 6261–6273, 1967.
- McKenzie, D. P., Speculations on the consequences and causes of plate motions, *Geophys. J. R. Astron. Soc.*, *18*, 1–32, 1968.



- Mitrovica, J. X., and A. M. Forte, Radial profile of mantle viscosity: Results from the joint inversion of convection and postglacial rebound observables, *J. Geophys. Res.*, *102*, 2751–2769, 1997.
- Mooney, W. D., G. Laske, and G. Masters, CRUST 5.1: A global crustal model at  $5^\circ \times 5^\circ$ , *J. Geophys. Res.*, *103*, 727–747, 1998.
- Moresi, L., and M. Gurnis, Constraints on the lateral strength of slabs from three-dimensional dynamic flow models, *Earth Planet. Sci. Lett.*, *138*, 15–28, 1996.
- Müller, D., W. R. Roest, J. Y. Royer, L. M. Gahagan, and J. G. Sclater, Digital isochrons of the world's ocean floor, *J. Geophys. Res.*, *102*, 3211–3214, 1997.
- Nataf, H.-C., and Y. Ricard, 3SMAC: An a priori tomographic model of the upper mantle based on geophysical modeling, *Phys. Earth Planet. Inter.*, *95*, 101–122, 1996.
- Nelder, J. A., and R. Mead, A simplex method for function minimization, *Comput. J.*, *7*, 308–313, 1965.
- National Oceanic and Atmospheric Administration (NOAA), Data Announcement 88-MGG-02, Digital relief of the Surface of the Earth, Natl. Geophys. Data Cent., Boulder, Colo., 1988.
- O'Connell, R. J., C. W. Gable, and B. H. Hager, Toroidal-poloidal partitioning of lithospheric plate motions, in *Glacial Isostasy, Sea-Level and Mantle Rheology*, edited by R. Sabadini, pp. 535–551, Kluwer Acad., Norwell, Mass., 1991.
- Pari, G., and W. R. Peltier, Subcontinental mantle dynamics: a further analysis based on the joint constraints of dynamic surface topography and free-air gravity, *J. Geophys. Res.*, *105*, 5635, 2000.
- Parsons, B., and J. G. Sclater, An analysis of the variation of ocean floor bathymetry and heat flow with age, *J. Geophys. Res.*, *82*, 803–827, 1977.
- Press, W. H., S. A. Teukolsky, W. T. Vetterling, and B. P. Flannery, *Numerical Recipes in C: The Art of Scientific Computing*, 2nd ed., Cambridge Univ. Press, New York, 1993.
- Puster, P., and T. H. Jordan, How stratified is mantle convection?, *J. Geophys. Res.*, *102*, 7625–7646, 1997.
- Ray, T. R., and D. L. Anderson, Spherical disharmonics in the Earth sciences and the spatial solution: Ridges, hot-spots, slabs, geochemistry and tomography correlations, *J. Geophys. Res.*, *99*, 9605–9614, 1994.
- Ricard, Y., and C. Vigny, Mantle dynamics with induced plate tectonics, *J. Geophys. Res.*, *94*, 17,543–17,559, 1989.
- Ricard, Y., M. A. Richards, C. Lithgow-Bertelloni, and Y. Le Stunff, A geodynamic model of mantle density heterogeneity, *J. Geophys. Res.*, *98*, 21,895–21,909, 1993.
- Richardson, R. M., Ridge forces, absolute plate motions, and the intraplate stress field, *J. Geophys. Res.*, *97*, 11,739–11,748, 1992.
- Richardson, R. M., S. C. Solomon, and N. H. Sleep, Tectonic stresses in plates, *Rev. Geophys.*, *17*, 981–1019, 1979.
- Richter, F. M., Dynamical models for sea floor spreading, *Rev. Geophys.*, *11*, 223–287, 1973.
- Ritsema, J., and H. J. van Heijst, Seismic imaging of structural heterogeneity in Earth's mantle: Evidence for large-scale mantle flow, *Sci. Progr.*, *83*, 243–259, 2000.
- Solomon, S. C., and N. H. Sleep, Some simple physical models for absolute plate motions, *J. Geophys. Res.*, *79*, 2557–2567, 1974.
- Solomon, S. C., N. H. Sleep, and R. M. Richardson, On the forces driving plate tectonics: Inferences from absolute plate velocities and intraplate stress, *Geophys. J. R. Astron. Soc.*, *42*, 769–801, 1975.
- Steinberger, B., Slabs in the lower mantle: Results of dynamic modelling compared with tomographic images and the geoid, *Phys. Earth Planet. Inter.*, *118*, 241–257, 2000.
- Steinberger, B., H. Schmeling, and G. Marquart, Large-scale lithospheric stress field and topography induced by global mantle circulation, *Earth Planet. Sci. Lett.*, *186*, 75–91, 2001.
- Tackley, P. J., Mantle convection and plate tectonics: Toward an integrated physical and chemical theory, *Science*, *288*, 2002–2007, 2000.
- Turcotte, D. L., and E. R. Oxburgh, Finite amplitude convective cells and continental drift, *J. Fluid Mech.*, *28*, 29–42, 1967.
- Turcotte, D. L., and G. Schubert, *Geodynamics: Applications of Continuum Physics to Geological Problems*, John Wiley, New York, 1982.
- van der Hilst, R. D., S. Widiyantoro, and E. R. Engdahl, Evidence of deep mantle circulation from global tomography, *Nature*, *386*, 578–584, 1997.
- Wessel, P., and W. H. F. Smith, New version of the Generic Mapping Tools released, *Eos Trans. AGU*, *76*, 329, 1995.